UNIVERSITY OF CALIFORNIA

Los Angeles

Heat Transfer in the Porous Structure of an Additively Manufactured Evaporator for a Two-Phase Mechanically Pumped Loop for Space Applications

A dissertation submitted in partial satisfaction of the

requirements for the degree of

Doctor of Philosophy

in

Aerospace Engineering

by

Luca Valdarno

2022

.

ABSTRACT OF THE DISSERTATION

Heat Transfer in the Porous Structure of an Additively Manufactured Evaporator for a Two-Phase Mechanically Pumped Loop for Space Applications

by

Luca Valdarno
Doctor of Philosophy in Aerospace Engineering
University of California, Los Angeles, 2022
Professor Vijay K. Dhir, Chair

The two-phase heat transfer technology has been a major thermal control hot-point for cooling or heat rejection during the last decade. Two-phase pumped cooling systems are applied when it is required to maintain a very stable temperature for heat dissipation in a system. A novel additively manufactured evaporator for two-phase thermal control has been developed at NASA Jet Propulsion Laboratory. The Two-Phase Mechanically Pumped Loop (2PMPL) permits latent heat transfer to be implemented with much wider breath of control authority compared to capillary-based systems while alleviating the system sensitivity to pressure drops. The flexibility of the 2PMPL stays in the capability to reclaim waste heat dissipation and to reject heat from discrete locations (multiple evaporators and condensers) and to control loop temperature with minimal control power. Another key aspect of this technology is the ability to integrate multi-phase heat transfer provisions directly with structural elements thanks to the conjunct use of the Additive Manufacturing Technology.

A collaboration between the NASA Jet Propulsion Laboratory, University of California Los Angeles and University of Michigan has been established to develop numerical models for the prediction of the thermal behavior and performance of the 2PMPL. The Boiling and

Phase Change Heat Transfer Laboratory in the Department of Mechanical and Aerospace Engineering at University of California Los Angeles has focused on the understanding and capture of the micro-scale evaporation occurring in the porous structure of the evaporator.

The main goal of the research has been to develop a modelling tool that can be used to design and optimize the evaporator. An all-encompassing numerical simulation can be carried out to predict the operational thermal behaviour of the evaporator taking into account the effect of the liquid-vapor interface at the wick-to-vapor border. The numerical model allows to study the effect of different parameters, such as boundary conditions (inlet temperature, input heat loads, etc.), geometrical parameters and wick (effective thermal conductivity, permeability, pore size, etc.) and fluid properties.

An experimental setup has been built in order to characterize the heat transfer within an additively manufactured porous sample and in particular its evaporative heat load under certain heat inputs. The experimental campaign has served also as validation for the numerical results and for the characterization of the transient phenomena such as dry-out.

The dissertation of Luca Valdarno is approved.

Adrienne Lavine

Chang-Jin Kim

Vasilios Manousiouthakis

Vijay K. Dhir, Committee Chair

University of California, Los Angeles

2022

Alla mia famiglia

Contents

List of Figures

List of Tables

Nomenclature

A	surface area	m^2
K	permeability	m^2
P	Pressure	Pa
Q	heat load	W
T	Temperature	°C
X^*, Y^*	dimensionless coordinates	$-$
$\dot{m}$	mass flow rate	g/s
$\hat{a}$	accommodation coefficient	-
$\hat{t}, \hat{n}$	tangential and normal coordinates	m
$\widetilde{M}$	molar mass	kg/mol
$\widetilde{R}$	universal gas constant	$J/(K \cdot mol)$
c_p	specific heat	J/K
h	heat transfer coefficient	W/m^2K
h_{fg}	latent heat of evaporation	J/kg

k	thermal conductivity	$\mathrm{W/(m \cdot K)}$
q	heat flux	$\mathrm{W/m^2}$
r	radius	m
u, v, w	components of velocity along (x, y, z)	m/s
x, y, z	axis coordinates	m

Acronyms

CPL Capillary Pumped Loop

ISS International Space Station

JPL Jet Propulsion Laboratory

LHP Loop Heat Pipe

MPFL Mechanically Pumped Fluid Loop

NASA National Aeronautics and Space Administration

PFPE Perfluoropolyether

PFL Pumped Fluid Loops

2PMPL Two-Phase Mechanically Pumped Loop

Greek Symbols

α	angle	deg
ϵ	porosity	-
μ	dynamic viscosity	$\mathrm{m^2/s}$

ρ	density	kg/m^3
σ	surface tension	N/m

Subscripts

cap	capillary
conv	convection
e	effective
ev	evaporation
in	input
l	liquid
out	output
part	particle
p	pore
sat	saturation
s	solid
v	vapour

Acknowledgments

I am immensely grateful to Prof. Vijay K. Dhir for his guidance, encouragement and support during these years. His genuine passion and dedication to science are a source of inspiration for my future professional endeavours.

I would like to extend my appreciation to my past and present labmates of the Boiling and Phase Change Laboratory at UCLA for sharing these years of hard work together.

I am infinitely grateful to Eric Sunada and Ben Furst for the opportunity to work on R&D technologies on two-phase heat transfer at JPL. I am in particular thankful for their guidance, kindness and friendship.

I would like to extend my gratitude to the JPLers I have the chance to work with, especially the Thermal Fluid Systems and Hardware group and the Mars Sample Return Thermal Team. I appreciate the flexibility and support I have received in particular during the final phase of my doctorate and I am grateful to be in a place where I feel at home.

Finally, my most profound gratitude is for my parents and my brothers for their constant love and support during all my entire life. I would also like to wish my niece and nephews the strength and perseverance to pursue their dreams in their lives.

Vita

University of California at Los Angeles, United States

M.S. in Aerospace Engineering, 2020

University of California at Berkeley, United States

M.Eng. in Nuclear Engineering, 2017

Politecnico di Milano, Italy

B.S. and M.S. in Space Engineering, 2012

Publications

L. Valdarno, E. Ossola, B. Furst, E. Sunada, and V. K. Dhir. "Thermo-mechanical Analysis and Design of an Additive Manufactured Evaporator for a Two-Phase Mechanically Pumped Loop". In: 50th International Conference on Environmental Systems. 2021.

L. Valdarno, V. K. Dhir, B. Furst, and E. Sunada. "Heat Transfer Modeling in the Wick Structure of an Innovative Evaporator for a Two-Phase Mechanically Pumped Loop". In: International Conference on Environmental Systems. 2020.

L. Valdarno, V. K. Dhir, B. Furst, and E. Sunada. "Heat Transfer Modeling of an Additive Manufactured Porous Structure of a Two Phase Evaporator for Spacecraft Thermal Control.". In: American Society for Gravitational and Space Research Virtual Meeting. 2020.

L. Valdarno, V. K. Dhir, B. Furst, and E. Sunada. "Heat Transfer in a Porous Medium with Local Heating and Evaporation on the Top Boundary". In: International Mechanical Engineering Congress and Exposition (IMECE). 2019.

Chapter 1

Two-Phase Mechanically Pumped Fluid Loop

1.1 Introduction

With the advancements in space missions, the need for highly efficient thermal control systems that can handle high heat fluxes and accurate temperature control is increasing. To meet these demands, a novel Two-Phase Mechanically Pumped fluid Loop (2PMPL) for spacecraft thermal control was developed at the NASA Jet Propulsion Laboratory (JPL). The system incorporates an innovative additively manufactured planar evaporator that uses a porous wick to separate the liquid and vapor phases. In a two-phase pumped system, a pump is used to circulate the fluid to an evaporator, where heat from the payload is absorbed while liquid is evaporated. The vapor then flows to a condenser where the vapor is condensed back into liquid.

The two-phase heat transfer technology has been a major thermal control hot-point for cooling or heat rejection of the last decade. The main applications including heat pipe, capillary pumped loop (CPL) and loop heat pipe (LHP) have now been used in a variety of aviation thermal management. While CPL and LHP have reached a flight maturity grade

by offering major advantages over the traditional thermal control technology, it is clear that this technology alone will not meet the needs of all future scientific spacecrafts [1].

NASA's technology road-map [1] specifically lists two-phase pumped loops systems as an enabling thermal management technology. Two-phase mechanically pumped cooling loop has emerged as a highly effective means for dissipating large amounts of heat from a small heat transfer area and provided a robust solution for significant design with its more flexibility, more precise temperature control, greater heat transport capacity.

1.2 Two-phase technologies for spacecraft thermal control

Spacecraft thermal control consists of managing the heat transfer within the different subsystems by control of the conductive and radiative heat paths through selection of the proper geometrical configurations, insulation blankets, sun shields, radiating fins, surface thermo-optical properties, thermal coating, heat sinks, heat pipes, pumped fluid loops, louvers, heaters and phase-change materials. The spacecraft component temperatures are maintained within the desired range by proper control of the dissipated energy between all spacecrafts elements during the different mission phases. The pros and cons of the two-phase mechanically pumped loops compared to traditional cooling techniques for space applications are here presented.

1.2.1 Capillary pumped loops vs. Two-phase mechanically pumped loops

In a Capillary Pumped Loop (CPL) heat is transported from the evaporator to the condenser through the flow generated by capillary pumping of the curvature of the liquid-vapor interface. The capillary pumping limits the total heat load and transport length since the pressure drop of the system has to be lower than the capillary pressure of the meniscus at

the porous interface. The thermal performance is completely dictated by the wick properties such as permeability, pore size and porosity.

The 2PMPL developed at JPL is very similar to a CPL since it separates the fluid phases in the evaporator but it can count on the addition of a centrifugal pump and a by-pass line that connects the outlet of the pump to the condenser outlet. The mechanical pump and the by-pass line assist the fluid flow in addition to the capillary pumping and allow to control the pressure at condenser outlet. Reducing pressure at the condenser outlet provides a suction head that assists the capillary forces in moving the fluid through the evaporator. These two elements significantly impact the performance of the fluid loop since enable the thermal management of much larger systems subjected to higher heat loads. Moreover, in the event of pump failure, the system could operate as a CPL at lower performance.

1.2.2 Single phase vs. Two-phase mechanically pumped loops

Pumped Fluid Loops (PFLs) are devices that provide efficient transfer of a large amount of thermal energy between two points by means of forced liquid cooling. A simplified PFL consists of a pumping device, a heat exchanger and a space radiator. The cooling can be accomplished by the use of a coolant as the thermal transport agent. The coolant absorbs the dissipated energy from the component and transfers it to a heat sink. The coolant is recirculated within the system once its thermal energy has been radiated to space via a radiator.

Mechanically pumped fluid systems have advantages over capillary-based heat pipes systems in the following aspects:

- less sensitivity to pressure drops which allow for longer transport distances and smaller piping diameters

- more flow rate control authority which increases heat flux limits and robustness during start-up and turn-down.

The most notable disadvantage is the use of mechanical pump that requires electric power and introduces reliability concerns associated with a mechanism. A two-phase mechanically pumped system has the following advantages over a single-phase pumped system: high heat flux accommodation, minimal temperature excursion required to transfer heat, and a high degree of isothermality. This is due to the use of latent versus sensible heat for the single-phase option. This also results in smaller flow rates and pumping power due to the generally higher heat of vaporization compared to the product of specific heat and an acceptable temperature excursion of the fluid for the single-phase liquid. However, the two-phase must deal with a degree of uncertainty related to flows and phase change in microgravity and need to supply sufficient net positive suction head to the pump without creating an excessive sensible heating range prior to evaporation or boiling. In 2010, the Alpha Magnetic Spectrometer instrument on board the International Space Station was successfully commissioned using a two-phase thermal control system designed by the National Aerospace Laboratory of the Netherlands [2]. The system utilized a two-phase accumulator to provide loop temperature control using carbon dioxide as working fluid for its relatively high vapor to liquid density and its compatibility with the instrument radiation environment.

1.2.3 Mixed vs. Separated two-phase mechanically pumped loops

Mixed and separated two-phase flows pumped loops can rely on same basic elements such as a pump, an evaporator, a condenser and an accumulator. However, the main difference is that in a mixed two-phase flow the liquid and vapor phases are not separated in the evaporator characterised by the presence of flow boiling that also continues in the flow line till the condenser. Classical two-phase MPFL relies on the mixed flow in the evaporator. These systems require a pre-heater to bring the fluid to saturation conditions at the inlet of the evaporator and an higher pumping power to supply the pressure drop of a larger two-phase flow region.

In a separated two-phase flow MPFL the wick in the evaporator acts as a liquid and

vapor phases separator. The two-phase region is confined in the evaporator while the rest of the loop is practically a single phase loop. Two-phase flow in microgravity is notoriously unpredictable. For instance, for low flow rates inertia forces might not dominate over surface tension forces leading to possible flow instabilities that can affect pressure drop and flow maldistribution. Moreover, based on current technology the only type of pump recommended for long-life missions ($>$ 15 years) are centrifugal pumps with hydrodynamics bearings. The temperature at the inlet of these pumps must be subcooled to avoid cavitation and provide significant Net Positive Suction Head (NPSH). In the separated two-phase flow MPFL the wick works also as pre-heater while the fluid flows through it before reaching the porous border at the vapor chamber. The simplicity in the design of a separated 2PMPL allows to host multiple evaporators and condensers along the path without affecting the overall system complexity.

1.3 JPL Two-Phase Mechanically Pumped Loop

1.3.1 Design requirements

Sunada et al. [3] describe the need for a novel thermal management technology that could enable new deep space science missions. Planetary science missions to outer planets are expensive. Every Watt of heating requires approximately three kilograms of mass at 10 Astronomic Units (AU). The need to reduce mass and power consumption could be enabled by thermal technologies that can best manage power resources while not impacting on the overall mass. Efforts in integrated thermal management systems are necessary to achieve these new challenging goals. It is clear that relying on temperature deltas to drive heat is not sufficient for spacecrafts with higher heat densities. A thermal management system that is able to offer accurate temperature control for scientific instruments is critical to reduce the instrument noise levels and, consequently, to strongly improve the science data return. Previous studies conducted at the NASA Jet Propulsion Laboratory (JPL) identified Two-

Phase Mechanically Pumped fluid Loops (2PMPL) as being well suited to meet the thermal control needs of many spacecraft missions focused on scientific exploration.

The specific loop architecture developed at JPL are based on a set of underlying thermal and structural requirements presented by Sunada et al. [3]:

- accommodate any arrangement of heat loads up to 500 W
- accommodate any arrangement of heat fluxes up to 5 W/cm^2
- maintain a temperature difference below 2 °C
- provide temporal temperature fluctuations less than 0.05 °C/min
- be a planar 1 m^2 heat acquisition surface
- 15 year life, 500 krad total dose at the pump and control electronics

A Two-Phase Mechanically Pumped Loop permits latent heat transfer to be implemented with much wider breath of control authority compared to capillary-based systems while alleviating the system sensitivity to pressure drops. The flexibility of the 2PMPL stays in the capability to reclaim waste heat dissipation and to reject heat from discrete locations (multiple evaporators and condensers) and to control loop temperature with minimal control power. Another key aspect of this technology is the ability to integrate multi-phase heat transfer provisions directly with structural elements thanks to the conjunct use of the Additive Manufacturing Technology.

This architecture is well suited to produce an isothermal heat acquisition surface since during nominal operation only vapor (close to the saturation temperature) is present in the vapor channel. The wick in the evaporator serves two primary purposes: (1) it ensures that the heated surface remains wet in a microgravity environment (to avoid dry-out), and (2) it helps keep the heated surface isothermal by constraining the vapor flow to be next to the heated surface. Any subcooled liquid is kept away from the heated surface by the wick.

1.3.2 Loop description

In 2PMPL developed at JPL, a mechanical pump is used to circulate the fluid to an evaporator and through a by-pass line. In the evaporator, heat from the payload is absorbed while liquid is evaporated. The evaporator contains two channels separated by a porous wick. The wick serves as a phase separator and ensures that only vapor exits through the vapor line. Then, the vapor flows to a condenser where it condenses back into liquid, and combines with the liquid exiting the by-pass line. A sub-cooler ensures that the liquid is adequately sub-cooled for the mechanical pump, and an accumulator is used to regulate system pressure and thus evaporation temperature. The system architecture is essentially a Capillary Pumped Loop (CPL) with the addition of a mechanical pump and a by-pass line to help maintain stable performance and extend the operational capability. Figure 1.1 illustrates the basic concept of the 2PMPL and Figure 1.2 shows the experimental setup of the ammonia test-bed 2.0.

During the operational nominal conditions, a constant heat load is applied to the evaporator, the pump is operating at constant speed and the accumulator temperature is held constant. The pressure balance is established along the by-pass line ΔP_{14}, the evaporator inlet ΔP_{12} and outlet lines ΔP_{34} and the capillary pressure at the wick ΔP_{cap}, as summarized in equation 1.1:

$$\Delta P_{14} = \Delta P_{12} + \Delta P_{34} - \Delta P_{cap} \tag{1.1}$$

The pressure loss in the by-pass line depends on the flow-rate dictated by the pump and the by-pass fluid resistance. In other terms, it is possible to assist the capillary pumping in the evaporator independently of the heat load applied. During nominal operation, the pressure in the vapor grooves is higher than the pressure in the liquid chamber preventing the liquid to invade the vapor grooves due to the action of the pump. In both the liquid and vapor lines at the inlet and outlet of the evaporator pressure decreases monotonically due to the fluid flow.

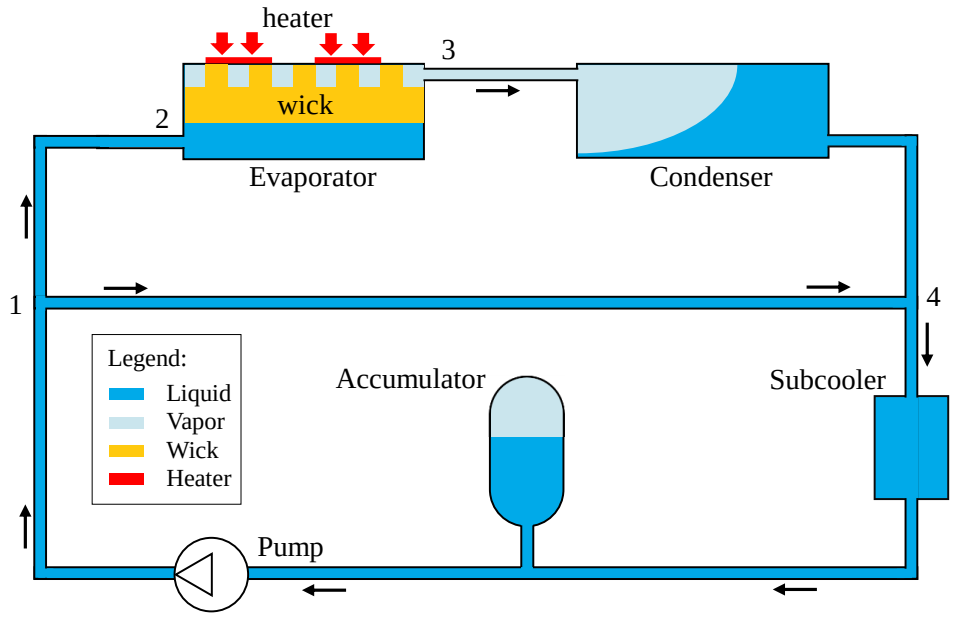

Figure 1.1: JPL Two-Phase Mechanically Pumped Loop layout.

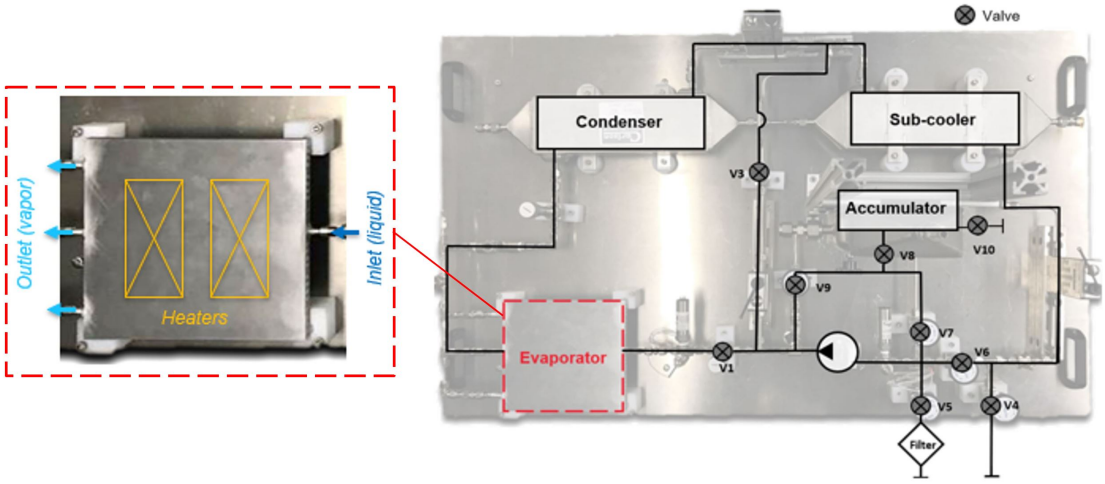

Figure 1.2: Experimental setup of the Two-Phase Mechanically Pumped Fluid Loop.

1.3.3 Working fluid

The fluid selected for the JPL two-phase mechanically pumped loop is ammonia at 10.34 bara. This selection is a result of a trade-off between many criteria such as heat transport performance, mass of the system, power consumption of the pump, accumulator sizing, tubing, etc. At the operating temperature of unmanned spacecraft missions, ammonia has the most favorable thermodynamic properties. The highest performance is obtained by utilizing a working fluid that has a low freezing temperature, a high surface tension, a high latent heat, and a low liquid viscosity. Moreover, ammonia is compatible with the aluminum wick and solid casing if proper care is taken in the manufacturing process. On the other side, handling ammonia needs an extra care in order to avoid severe irritation to eyes and other mucous membranes and severe burns to the skin.

1.4 JPL Two-Phase Evaporator

The evaporator chamber has a rectangular shape further split into two chambers (liquid and vapor) by a porous plate that serves as wick. Vapor occupies the upper chamber thus formed, whereas subcooled liquid flows in the lower chamber. The upper plate of the evaporator is subjected to uniform heat input. Several porous pillars serve to transport heat from the top plate to the upper surface of the wick. Liquid in the lower chamber needs to remain subcooled to reduce any chances of vapor formation in the liquid chamber. Similarly, pressure in the vapor chamber (capillary pressure) needs to remain sufficiently high to eliminate migration of liquid into the vapor chamber. Vapor generated as a result of evaporation at the wick interface occupies the vapor chamber and creates a nearly isothermal condition on the back side of the heat receiving surface. Vapor is also superheated as a result of heat transfer from the upper chamber walls and the pillar transferring heat to the wick. Vapor exiting the chamber is converted into liquid in the condenser.

In the capillary porous structure, the liquid-vapor interface adjusts itself to steady con-

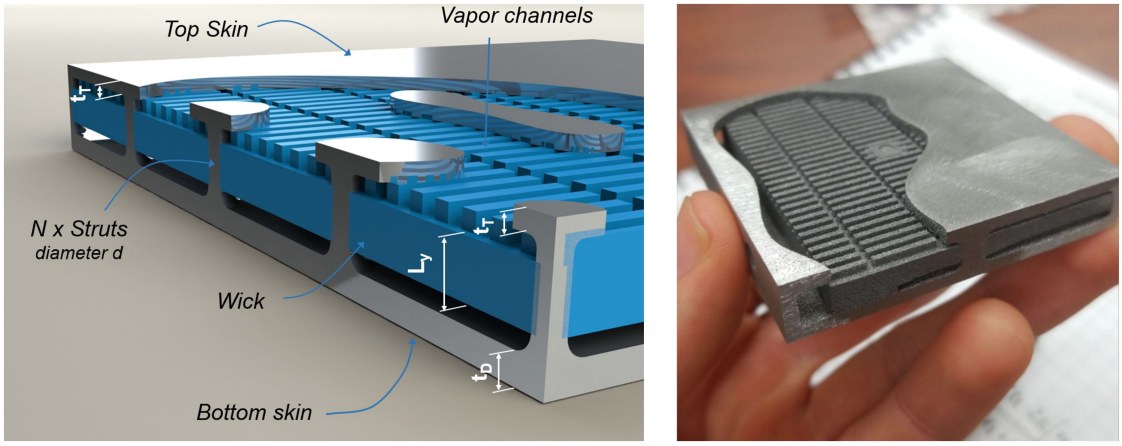

Figure 1.3: Evaporator layout (left). Show-sample of the evaporator (right).

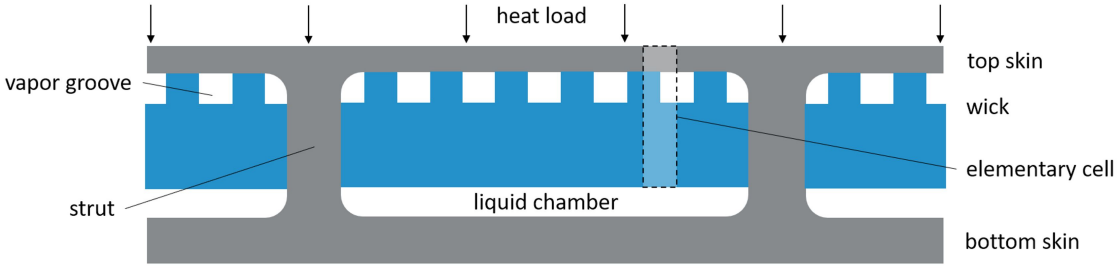

Figure 1.4: Evaporator cross-section.

ditions at various heat fluxes by spontaneously changing the curvature of the menisci and the location in the porous media. In a nominal operational case, where the liquid-vapor interface is located along the boundary between the wick and the vapor grooves, most of the heat goes into the evaporation of the liquid from the menisci. The vapor grooves not only form a well-developed evaporating surface, but also ensure the removal of the vapor that, formed in the evaporator, flows into the vapor line to move towards the condenser.

1.4.1 Design evolution

Since 2016, five generations of evaporators have been developed, demonstrating constant improvements in thermal performances and mass budgets. If the first prototype is composed of multiple components fabricated with conventional techniques and sealed together using

Table 1.1: Main features of the ammonia evaporator [4].

Housing	Area [mm^2]	213 x 197
	Thickness [mm]	16
Porous Structure	Thickness [mm]	4
	Max. pore radius [μm]	18
	Porosity [%]	22.3
	Permeability [m^2]	3.2 x 10^{-13}
Vapor grooves	Size [mm^3]	1 x 1 x 10
	Pitch [mm]	1

an o-ring, the following generations exploit the potential of Additive Manufacturing, which enables the fabrication of monolithic evaporators where solid and porous materials can be printed at the same time by tailoring the process parameters. Since the third prototype, which is designed to operate with ammonia, wick properties have been improved and the structural performance together with mass savings have been considered as well. Thinner form factors are achieved, going from 16 mm-thick evaporators (3rd gen) to 10 mm-thick evaporators (4th gen), also by using internal full-solid struts helping in withstanding the internal pressure loading.

The baseline evaporator unit measures 213 x 198 x 16 mm and has a mass of 1.3 kg. The wick material, separating the liquid channel from the vapor grooves, is additively manufactured along with the rest of the evaporator. The maximum pore radius is 18 μm with an average value of 6 μm. The measured permeability is of 3.2 x 10^{-13} m^2 and porosity is 22.3 %. The baseline design presents a wick thickness of 4 mm and a pillar 1 x 1 x 10 mm. The distance between two consecutive pillars (vapor groove) is 1 mm. Figure 1.3 and Figure 1.4 illustrate the evaporator layout and its cross-section. The unit is designed to withstand 1.7 barg. In the nominal case, two main heaters are placed on top of the evaporator on a surface of 50.8 x 101.6 mm providing a power of 250 W each maximum (4.8 W/cm^2). Test results shows that the evaporator unit can keep spatial isothermality within 0.5 °C for heat loads up to 100 W and within 3 °C for heat loads up to 325 W [4].

1.4.2 Powder Bed Fusion Additive Manufacturing technique

The innovative evaporator developed for the Two-Phase MPFL was fabricated at JPL using Powder Bed Fusion (PBF) Additive Manufacturing (AM). This manufacturing process allows the entire evaporator to be fabricated as a single monolithic piece, and affords great geometric design freedom removing the constraints coming from traditional manufacturing processes. The most common additive manufacturing method is the sintered powder technique. However, the main disadvantage stays in the generation of a random internal structure in the porous media which promotes heterogeneity in the fluid-thermal performances. Furthermore, this method does not allow the fabrication of a monolithic piece consisting of both solid and porous structures such as the evaporator. On the other side the Power Bed Fusion AM technique employed at JPL allows the manufacturing of a lattice-structure with a well defined unit-cell geometry. The main limitation stays in the resolution of the laser to print fine explicitly modelled features and pore size.

Gotoh et al. [5] present a detailed experimental study on the porous properties of samples produced at JPL using the Power Bed Fusion AM technique with samples in AlSi10Mg, Stainless steel 316L, Inconel 625 and Ti-6Al-4V. The authors report measurements of the effective pore radius, permeability and porosity. They show that with this processes by varying the laser parameters they obtained porous materials with pore radii from 1.1 to 28.1 μm, porosity ranging from 10.4 to 42.4 % and permeability ranging from 5.9 x 10^{-16} to 4.4 x 10^{-12} m^2. With appropriate energy density given to the laser, porosity and other parameters can be controlled.

1.5 Ammonia test-bed 3.0

1.5.1 Description

In order to establish a Technology Readiness Level (TRL) 5, the Two-Phase MPFL test-bed has been updated and tested at JPL in 2021 and 2022. A TRL 5 technology has to

demonstrate that each element of the loop replicates the thermal-hydraulics characteristics of the intended flight system under relevant environmental factors. A relevant environment is defined as a specific subset of the operational environment that focuses on stressing the technology advancement in question. For the Two-Phase MPFL, this means that a higher level of fidelity is needed to verify the correct operation of the evaporator, the condenser and the complete system. The system counts on a two freezable radiators, instead of the liquid-liquid plate heat exchanger used for the condenser and sub-cooler in the previous design. The freezable radiators, designed by Creare, are condenser tubes with an internal cylindrical and annular wick that separates the incoming vapor (outer annulus) from the outgoing liquid (inner core) where the condensate exits. When a low heat load is applied at the evaporator, liquid freezes without the formation of liquid slugs.

Figure 1.5 shows the layout of the ammonia test-bed 3.0. As described by Furst et al. [4], the loop includes a miniature centrifugal pump (TCS Micropumps Ltd. - Model M510), diaphragm valves (Swagelok - Model SS-4BK), one needle valve (Swagelok - Model SS-4BMRG) located along the by-pass line, an accumulator designed to be the highest point of the loop. Transfer lines are made of 6.35 mm 316 stainless steel tubing with 0.89 mm wall thickness. RTDs (Omega Engineering - Model PR-20) are installed along the fluid line and E-type thermocouples are located on the bottom side of the evaporator, along the radiator and along the loop. Coriolis flow-meters (Brokhorst USA - Model M14) are calibrated for ammonia, pressure transducers (Transducer Direct - Model TD1200) are calibrated to read absolute pressure and differential pressure transducers are installed along the loop. On top of the evaporator a IR camera (FLIR) is used to record the evaporator thermal behaviour. All the system, with exception of the top face of the evaporator, is insulated. A relief valve (Rego - Model SS9432T) vented to a water reservoir is installed for safety. Heat load is applied on top of the evaporator using polyimide film heaters (Minco Products, Inc. - Model HAP). The vapor exiting the evaporator is conveyed into the freezable radiators located inside a vacuum chamber with internal pressure of 10^{-6} torr. The radiators are located between two aluminum plates cooled by two cold plates with LN_2 with 100 K as inlet temperature, as

shown in Figure 1.6. The by-pass line merges into the outlet of the radiator followed by a sub-cooler tube facing directly the cold plates.

Thermal-hydraulics numerical models have been developed at UCLA under the supervision of Prof. Vijay K. Dhir to capture the micro-scale evaporation and flow occurring in the evaporator during operation and a system level model has been developed by University of Michigan under the supervision of Prof. Massoud Kaviany to understand and predict the loop behavior and dynamics.

1.5.2 Experimental procedure

Figure 1.7 shows the experimental setup of the ammonia 2PMPL and the radiator plates located in the vacuum chamber at JPL. The test-bed operating procedure is the following:

1. Pull vacuum in the vacuum chamber.
2. Activate accumulator: pressurize system, turn on heater control and select a set point temperature.
3. Activate shroud cooling: start LN_2 flow through the cold plates to cool-down the shroud.
4. Turn on pump at a fixed speed: force liquid circulation in the loop.
5. Once steady-state conditions are reached at the shroud, switch on the IR camera and turn on heat load at the evaporator and wait for thermal steady-state.
6. Run specific test: testing of system limits, evaporator stability, max heat flux, etc.
7. Shut down the system: turn off the evaporator, close LN_2 inlet valve and let the shroud warm up, turn off the pump and the accumulator.

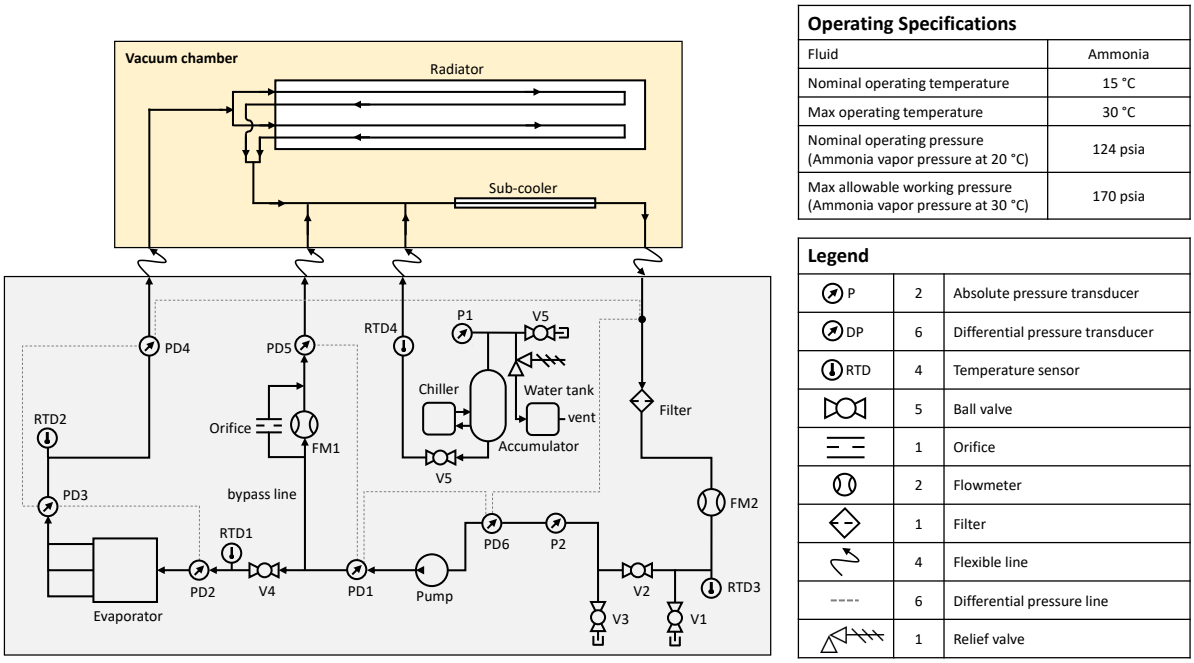

Operating Specifications	
Fluid	Ammonia
Nominal operating temperature	15 °C
Max operating temperature	30 °C
Nominal operating pressure (Ammonia vapor pressure at 20 °C)	124 psia
Max allowable working pressure (Ammonia vapor pressure at 30 °C)	170 psia

Legend		
P	2	Absolute pressure transducer
DP	6	Differential pressure transducer
RTD	4	Temperature sensor
	5	Ball valve
	1	Orifice
	2	Flowmeter
	1	Filter
	4	Flexible line
----	6	Differential pressure line
	1	Relief valve

Figure 1.5: Ammonia test-bed 3.0

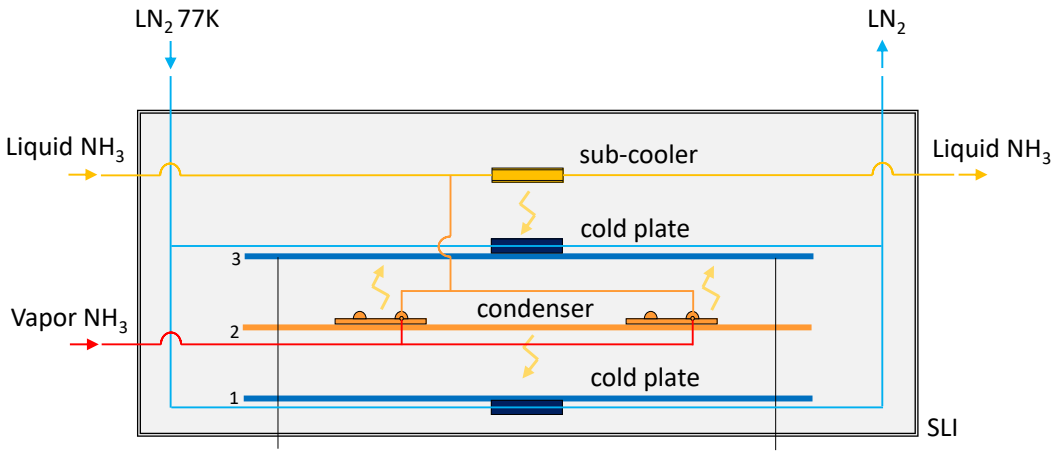

Figure 1.6: Radiator layout inside the vacuum chamber.

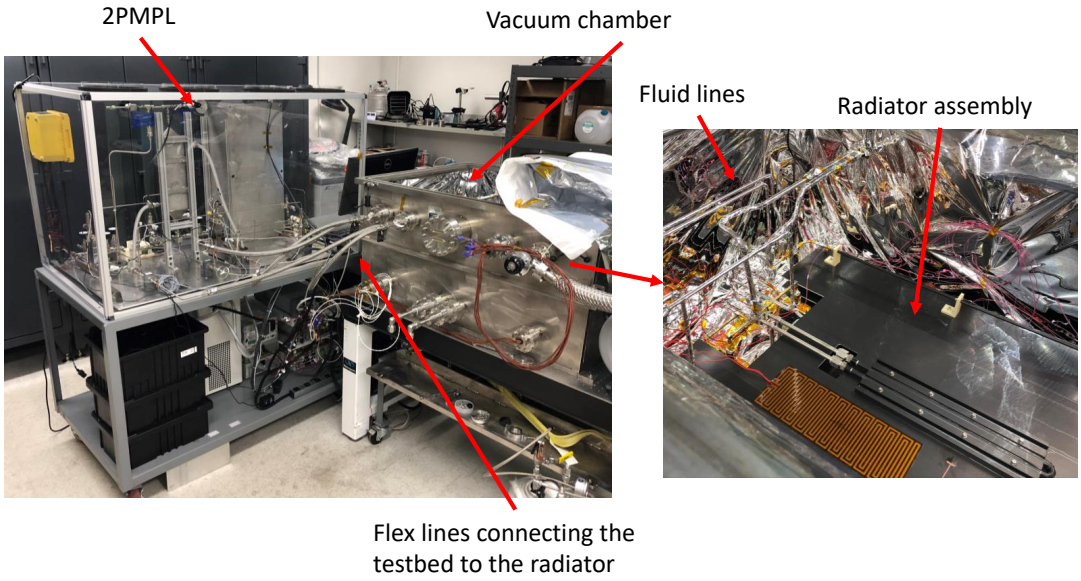

Figure 1.7: Experimental setup of the Ammonia test-bed 3.0 (left). Radiator inside the vacuum chamber (right).

1.5.3 Experimental results

Figure 1.8 illustrates and summarizes the operating regime of the 2PMPL with a freezable radiator. The experimental limits are given by the dry-out limit (on the left) and the flooding limit (on the right), while the upper limit is represented by the capability of the radiator to reject a maximum power of 250 W.

Figure 1.10 presents a test with 150 W input heat load and a total mass flow rate of 80 g/min. After applying the heat input at the evaporator, fully separation is reached in few minutes at saturation temperature of 26 °C. The evaporator has a maximum gradient of temperature of 0.5 °C. The radiator has a gradient of temperatures along its length ranging from 3 to -47 °C and the temperature at the outlet of the sub-cooler (entering the pump) is 20 °C. The cold plate is maintained constant at -158 °C. The vapor mass flow rate is 7.3 g/min. Figure 1.9 shows the temperature mapping of the evaporator recorded by the IR camera. It is possible to notice how the start-up of the evaporator takes places in few

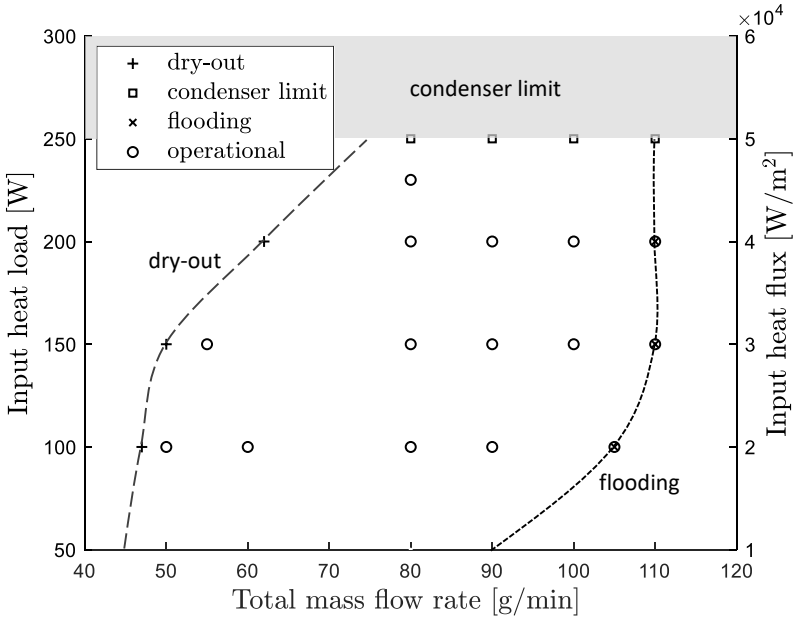

Figure 1.8: Working envelope of the 2PMPL Ammonia test-bed.

seconds. At t = 0, liquid flows inside the evaporator at 10 °C, when the heater at the inlet is switched on with a 150 W power, vapor is generated and expands throughout the full evaporator causing the fully separation of liquid and vapor phases in the rest of the loop.

The dry-out condition is characterized by a rapid increase of the evaporator temperatures due to vapor penetration inside the porous structure. Figure 1.11 presents test 16 with a 200 W heat load and a gradual decreasing of mass flow rate imposed from the pump. Dry-out occurs when the total mass flow rate reaches 62 g/min and the evaporator is affected by a rapid increase of temperatures. Vapor penetration occurs when the heat load is too high and is generating more vapor that can flow out to the condenser. The pressure differential across the meniscus overwhelms the capillary pressure that can be maintained by the meniscus.

Flooding is an event that is consequence of an higher pressure on the liquid side of the meniscus than the pressure on the vapor side, causing liquid penetration in the vapor grooves due to low heat loads and/or high mechanical pump pressure. Two types of flooding are observed: one with a rapid decrease of the temperatures at the evaporator and one where only the vapor mass flow rate is affected without effect on thermal behaviour of the

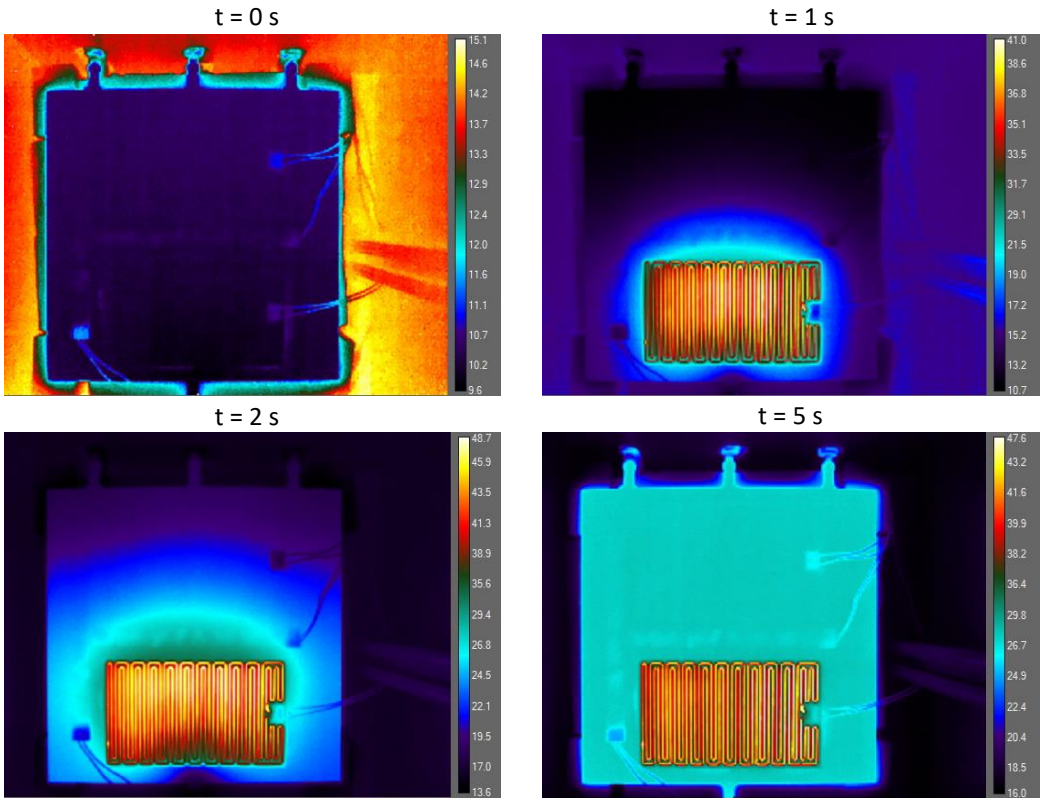

Figure 1.9: IR camera on the evaporator: vapor formation and flow separation at start-up. Heat load at inlet = 150 W, total mass flow rate = 80 g/min (Test 9).

evaporator. Figure 1.12 shows that partial flooding takes place in the evaporator when 150 W is applied at the inlet heater and 110 g/min of total mass flow rate is imposed by the pump. The system does not show thermal anomalies from the operational case, however a higher vapor flow rate compared to the ideal case is measured. This type of flooding can be explained by the fact that, while heat is applied over a certain area of the evaporator, at higher total mass flow rates the areas of wick far from the heater are not able to sustain the liquid meniscus anymore reducing the overall vapor mass flow rate and causing partial flooding. When the input heat is decreased to 100 W at same pump speed, it is possible to observe a total flooding event in the evaporator.

During the test campaign the radiator also demonstrated its capability to work from fully-frozen and partially-frozen conditions after applying heat load at the evaporator.

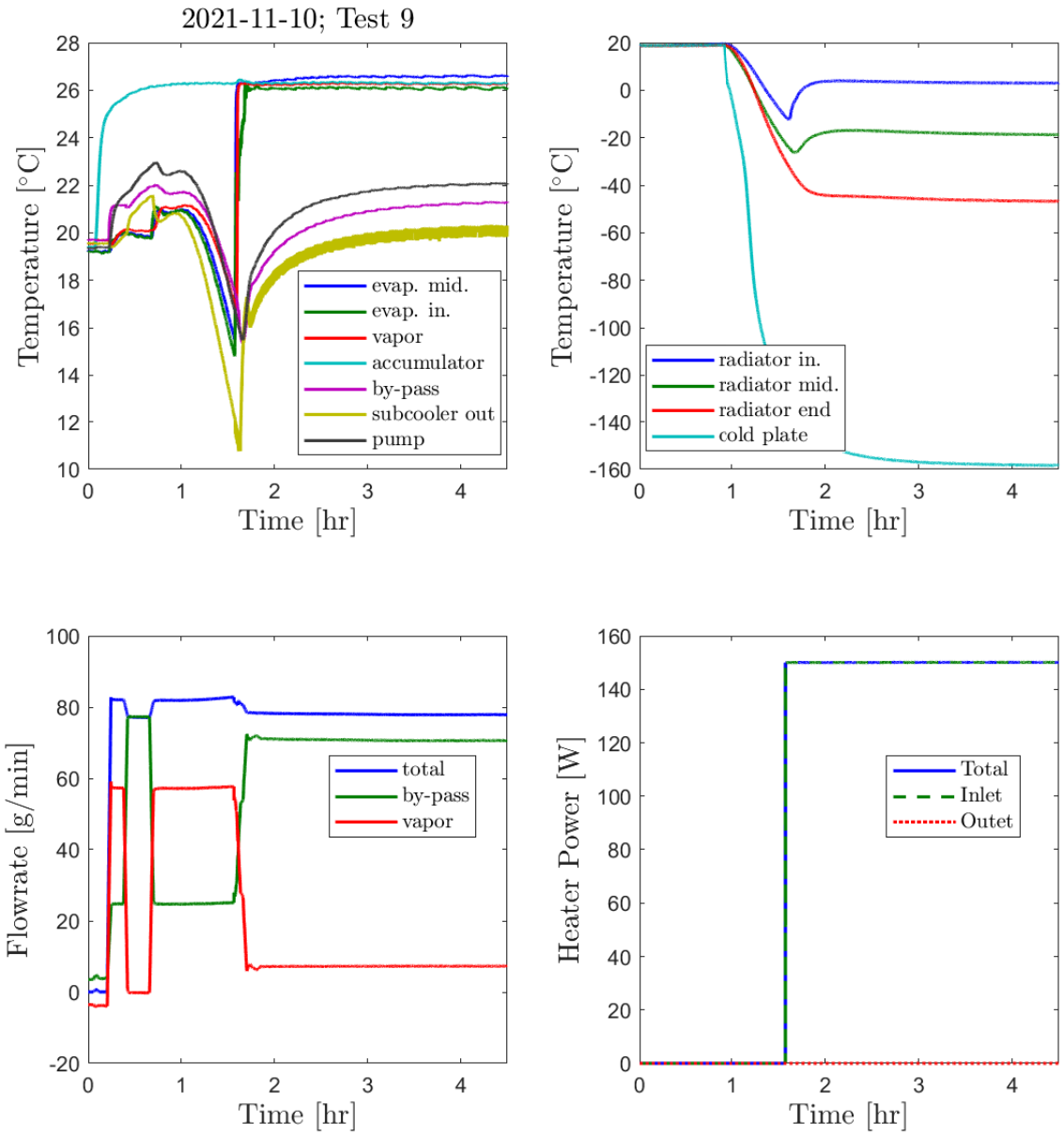

Figure 1.10: Operational case. Test 9: Heat load = 150 W, total mass flow rate = 80 g/min.

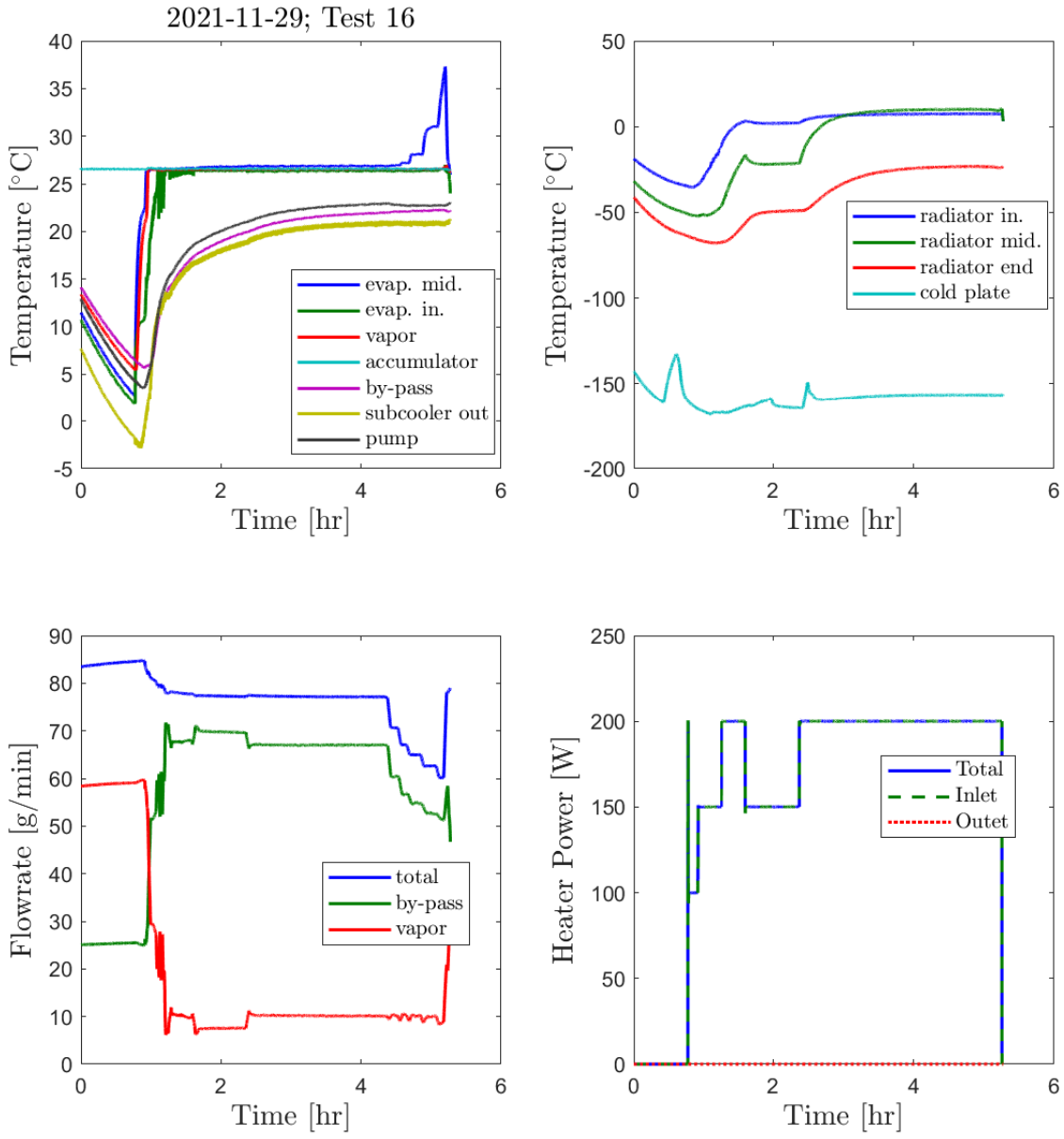

Figure 1.11: Dry-out event. Test 16: Heat load = 200 W, total mass flow rate = 62 g/min.

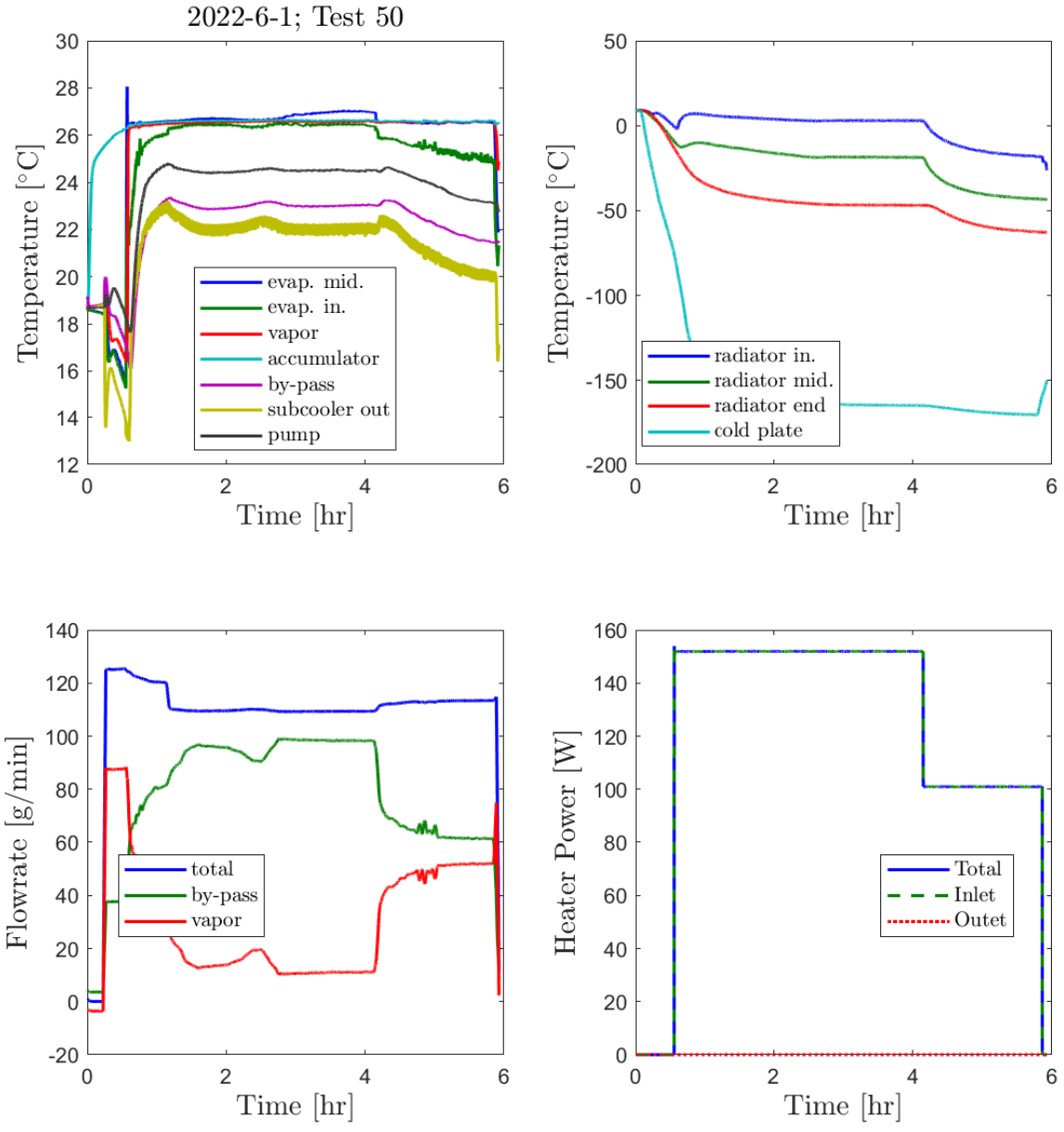

Figure 1.12: Partial flooding. Test 50: Heat load = 150 W, total mass flow rate = 110 g/min.

1.6 Research objectives

The evaporator has a strategical influence on the overall performance of the fluid loop and understanding the fundamental physics aspects under different operational regimes allows the optimization of the evaporator itself and of the entire loop. Thanks to the additive manufacturing techniques, it is possible not only to manipulate the porous properties but also integrate the two-phase heat transfer system directly within the structural elements. This design choice increases the heat transfer efficiency by removing interfaces and to reduce mass by combining different functions.

The need to fully understand and improve the performance of the two-phase evaporator is at the the base of the research conducted at UCLA. Understanding the heat and mass transfer within the porous structure of the evaporator and how it is connected to the dynamics of the liquid-vapor interface at the boundary of the porous structure is fundamental to characterize the current performance of the evaporator but also to design the next generation of 2PMPL.

The main goals of this research can be summarized as follows:

1. develop a numerical tool to predict the heat and mass transfer within the porous structure of the evaporator valid during nominal operational conditions (no vapor penetration).

2. develop a detailed model of the liquid-vapor meniscus at particle level along the evaporative boundary located between the wick structure and the vapor chamber.

3. design and build an experimental setup to observe the steady-state and transient behaviours of a simplified version of the 2PMPL evaporator.

An all-encompassing numerical simulation can predict the operational thermal behaviour of the evaporator in the two-phase pumped loop thermal control system. The numerical model allows to study the effect of different parameters, such as thermal conductivity, permeability, porosity, pore radius of the porous structure and of the fluid properties on the overall performance of the evaporator.

The experimental setup allows validate the numerical calculations and to investigate the transient behaviours of a capillary driven titanium evaporator. Both the numerical model and the experimental setup lead to better understand the fundamental physics aspect behind the thermal performance of the 2PMPL.

1.7 Thesis outline

This PhD thesis follows the below reported structure:

- Chapter 1 introduces the Two-Phase Mechanically Pumped Loop developed at JPL and the research objectives of this PhD thesis.

- Chapter 2 presents a bibliographic review of the state of the art of the two-phase evaporators. Lastly it discusses the main analytical, numerical and experimental studies found in literature.

- Chapter 3 describes the physical and mathematical problem formulation. The numerical models and their assumptions are discussed. Lastly, the main numerical results of the JPL evaporator and a parametric study of the main design features are discussed.

- Chapter 4 presents the experimental study on the titanium evaporator. In particular the experimental setup, procedure and validation are summarized. Lastly, it introduces the validation of the numerical model based on the experimental outcomes and a discussion of the experimental results.

- Chapter 5 lists the main conclusions of the PhD thesis.

Chapter 2

Literature Review

2.1 Introduction

The two-phase MPFL developed at JPL uses a similar evaporator layout of a capillary pumped loop integrated inside a system provided with a mechanical pump and a by-pass line located at the inlet of the evaporator. The JPL 2PMPL is a novelty in its genre since it combines the features of a CPL with those of a pumped loop. It allows to extend the limits of a traditional CPL thanks to the assistance provided by the pump, but also it allows to keep the liquid and vapor phases separated along the loop. This feature makes the JPL 2PMPL competitive for space applications since it removes the uncertainties connected to the physical understanding of two-phase flow in microgravity while keeping a isothermal evaporator. There are no other 2PMPL that use such solution and the only reference for two-phase evaporator is given by the CPL and LHP technologies.

In this chapter a discussion on the operating modes and limits of two-phase evaporator is presented first. Then, a literature review on the evaporator designs, wick materials and properties, working fluids is introduced. Finally, several analytical, numerical and experimental studies performed by different authors on the heat transfer of two-phase evaporators are presented.

2.2 Operating modes and limits

A conventional LHP works thanks to the capillary pressure created at the wick-to-vapor groove interface due to the presence of a liquid-vapor meniscus. Heat applied on the evaporator reduces the radius of the meniscus, creating a consequent suction capability that encourages the liquid from the liquid chamber to flow towards the liquid-vapor interface where it evaporates. Then the vapor flows towards the condenser where it exchange heat and return to the liquid phase.

Figure 2.1 illustrates the working principle of the evaporator for the 2PMPL. During the operational nominal conditions, the pump is operating at constant speed and the accumulator temperature is held constant. If a constant heat load is applied to the evaporator, a liquid-vapor meniscus is formed at the border between wick and vapor groove. This configuration allows the liquid to flow from the bottom of the liquid chamber to the liquid-vapor interface thanks to the capillary pressure created by the meniscus curvature. If the heat load is increased, bubble nucleation first and vapor penetration after might take place in the wick bringing the system to dry-out and failure, as shown in Figure 2.2.

2.2.1 Capillary limit

Capillary limit is consequence of the capillary pressure drop along the liquid-vapor interfaces in the evaporator section. When the capillary pressure is not sufficient to bring enough liquid flow from the condenser to the evaporator, dry-out of the evaporator wick occurs. The equation describing the capillary limit is:

$$\Delta P_{cap} = p_v - p_l = \frac{2\sigma}{r_e} \tag{2.1}$$

where σ is the surface tension and r_e is the effective radius of curvature of the meniscus.

The effective capillary radius is dependent upon particle size, packing mode and sintering process. Decreasing the radius of the particle size R_{part}, increases the capillary pumping.

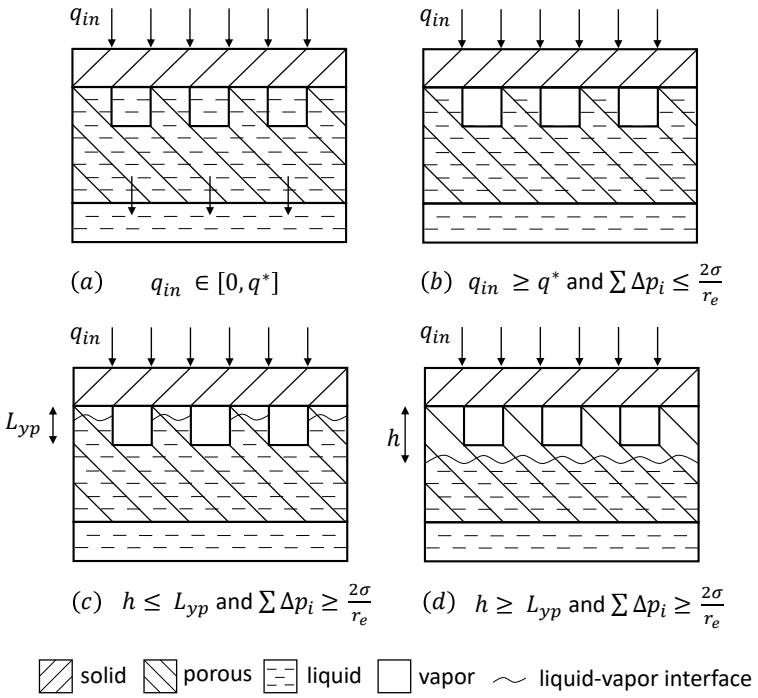

Figure 2.1: Working principle of the wick inside the evaporator.

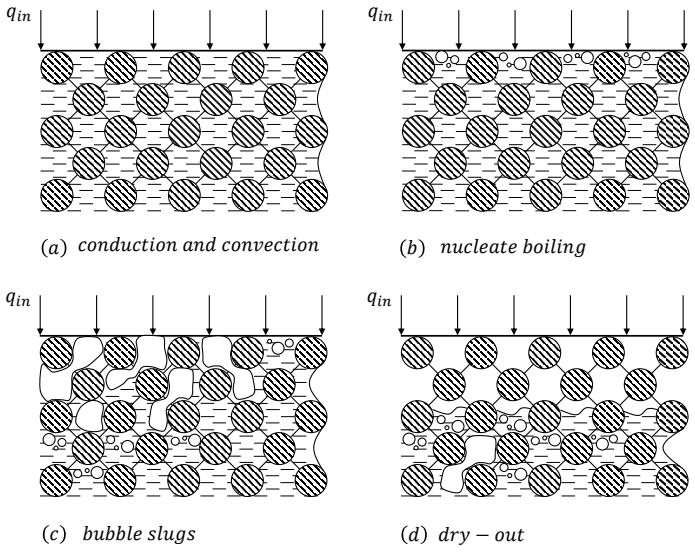

Figure 2.2: Different phases of the two-phase inside the porous structure of the evaporator.

However, as the particle size is reduced, the permeability also decreases. Equation 2.2 [6] shows the dependence of permeability on particle radius R_{part} and porosity ϵ:

$$K = \frac{R_{part}^2 \epsilon^3}{37.5(1-\epsilon)^2} \tag{2.2}$$

By increasing the heat load, liquid mass flow rate and pressure drop along the porous media increase. In a conventional LHP, if the pressure drop along the system is higher than the capillary pressure, the liquid-vapor interface recedes into the wick leading to an eventual failure of the loop. Nagano and Ku [7] and other authors in literature have studied and observed this limit both theoretically and experimentally.

2.2.2 Nucleation limit

The nucleation limit arises when the heat flux at the evaporator is sufficient to originate nucleate boiling in the evaporator section. The generated vapor bubbles block in part the liquid return and may bring to dry-out at the wick. The nucleation limit can be considered a heat flux limit.

Knowing the pressure distribution, then the Clausius-Clapeyron equation describes the minimum superheat for the onset of bubble formation as shown in equation 2.3:

$$T_l - T_{sat}\left(P_l\right) = \frac{2\ \sigma\ T_{sat}\left(P_l\right)}{h_{fg} r_p} \left(\frac{1}{\rho_v} - \frac{1}{\rho_l}\right) \tag{2.3}$$

To avoid bubble formation, the difference between the maximum temperature in the wick and the saturation temperature must be lower than the superheat indicated in equation 2.3.

In practice, the nucleation limit is difficult to predict. Hanlon and Ma [8] observed that when boiling occurs within the wick where the heat is applied, thin film evaporation at the liquid-vapor interface dramatically decreases as the boiling mode dominates the phase change behavior. A vapor bubble is generated near the heat load application area within the porous structure, increasing the thermal resistance and preventing the liquid to flow.

2.2.3 Other limits

In traditional heat pipes, other typical limits are the entrainment, sonic and viscous limits. The entrainment limit is due to high shear forces originated when the vapor goes in the counter-flow direction over the liquid saturated wick, where the liquid may be entrained by the vapor and returned to the condenser. This brings to an inadequate liquid flow of the wick structure. The sonic limit relates to low vapor densities, and the consequent mass flow rate results in high vapor velocities, increasing the possibility of choked flow in the vapor passage. The viscous limit arises at low operating temperatures, in which the saturation vapor pressure is usually of the same order of magnitude as the pressure drop needed to drive the vapor flow in the HP. This results in an inadequate pressure available to drive the vapor. These limits are all related to the vapor velocity, and are more significant at low temperatures. The reason is that the vapor pressure and vapor density lower as the temperature is decreased and, consequently, the vapor velocity needs to increase to carry the same amount of power. However, the entrainment, sonic and viscous limits are not of interest since vapour and liquid flow in separate channels in a conventional LHP.

2.3 Evaporator design

2.3.1 Evaporator layouts

The literature survey shows that it is possible to divide the evaporator shapes into two categories: cylindrical and flat with longitudinal or opposite liquid replenishment. Figure 2.3 presents these layouts. A cylindrical evaporator is massive for a space mission due to the need to cover a wide area without incurring in significant temperature gradients, but on the other side it has the advantage of a higher mechanical strength that makes it desirable for high pressure fluids such as ammonia. Maydanik, Chernysheva, and Pastukhov [9] present a review of flat evaporators: rectangular, disk- shaped, and flat-oval. The authors do not indicate a particular advantage given by a certain shape on the thermal performance.

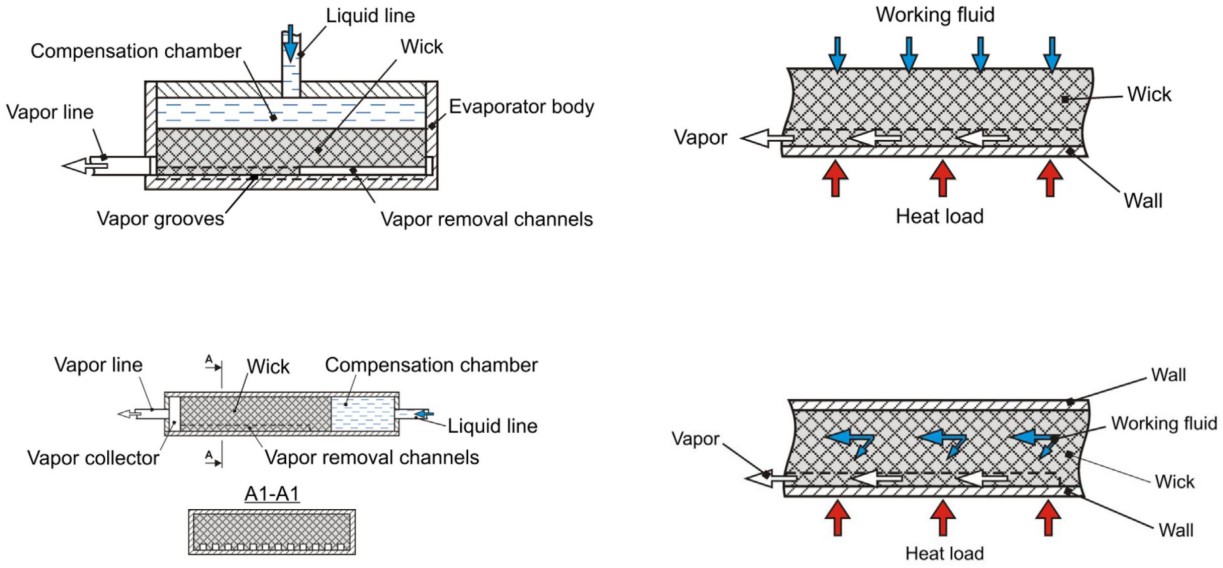

Figure 2.3: Schematics of flat evaporators with opposite (top) and longitudinal (bottom) replenishment [9].

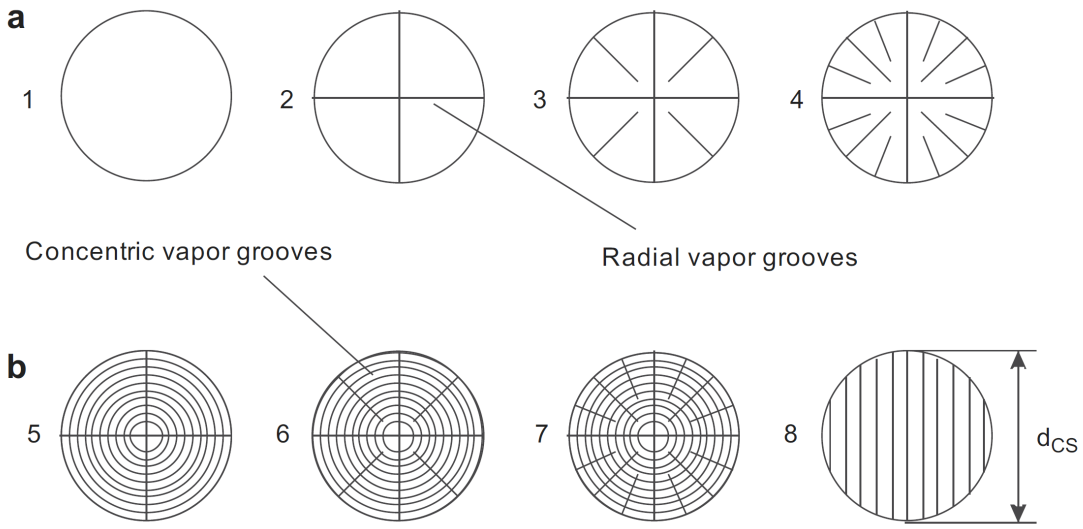

Figure 2.4: Vapor grooves layouts: only radial (a1 - a4); radial and concentric (b5 - b7); (b8) parallel [10].

An important part of any evaporator is the vapor groove. Vapor generated as a result of evaporation at the wick interface occupies the vapor chamber and creates a nearly isothermal condition. Kiseev, Vlassov, and Muraoka [10] presented an experimental study of vapor grooves with different cross-section shapes such as triangular, rectangular and trapezoidal. The authors observed that the optimum ratio for the heat transfer between the vapor groove cross-section and the heat input cross-section is 0.5. Moreover, they concluded that decreasing the size and distance between concentric vapor grooves intensified the heat transfer coefficient. Figure 2.4 illustrates the typical vapor grooves configurations as studied by Kiseev, Vlassov, and Muraoka [10].

A solid case typically surrounds the porous structure, the liquid chamber and the vapor grooves. The contact resistance between the solid and porous structures greatly affects the performance of the evaporator. Minimizing the contact resistance at the interface can improve the heat transfer withing the porous media. Metallic powders have the advantage to accommodate plastic deformations during the machining process, improving the contact between the solid and the porous structures. However, this does not eliminate the possibility to get local empty regions within the wick. Choi et al. [11] explored a sintering method for fabricating evaporators. The sintering method employed an organic material for the definition of the vapor grooves, which was then sublimated at the end of the sintering process. Interpenetrating the vapor chamber and the wick parts of the evaporator resulted in an increased contact area and thermal conductance.

2.3.2 Porous structures

The wick structure of the evaporator is the main element of any two-phase evaporator. The literature review shows a great variety of experimental studies on different materials such as plastics, metals and ceramics. Plastic porous structures such as polyethylene, polypropylene and PTFE have low effective thermal conductivity and limited maximum operating temperatures. Metal wicks such as stainless steel, aluminum alloy, titanium are very common. The

main distinction stays in the manufacturing process. The most common one is the sintered powder that typically provides low pore radius and high porosity. Ceramic wicks have the advantage of good chemical stability and compatibility with many fluids and low thermal conductivity minimizing the heat leaks to the liquid chamber.

The porosity is defined as the ratio between the volume occupied by the wick and the total volume. Increasing the porosity leads to an increase of liquid mass flow rate through the porous structure available for the evaporation process at the liquid-vapor interface along the wick-to-vapor groove boundary. On the other side, thermal and mechanical properties of the wick degrade with the increase of porosity.

The permeability is defined as the capability of the wick to transport liquid in presence of a pressure gradient. Higher is the permeability, lower is the pressure drop across the porous structure under same boundary conditions.

The pore size affects the maximum capillary pressure that the wick can sustain. Lower is the pore size, higher is the the capillary pressure. Typically a porous structure presents a distribution of pore radius within a certain range. The capillary limit is calculated from the maximum pore size measured by the bubble point test. Other methods are also available such as the risen meniscus test [12], and the fallen meniscus test [13].

The effective thermal conductivity of a wick structure fully saturated with liquid affects the ability of the wick to transport heat from the heat source to the evaporative boundary, but also influences the heat leaks towards the liquid chamber. Correlations are typically available to estimate the effective thermal conductivity [6]. Equation 2.4 illustrates the effective thermal conductivity as function of the thermal conductivities of the solid k_s and liquid k_l phases and the porosity ϵ for sintered particles:

$$k_e = \frac{k_s(2k_s + k_l - 2\epsilon\,(k_s - k_l))}{2k_s + k_l + \epsilon(k_s - k_l)} \tag{2.4}$$

Porosity, pore distribution and mean pore radius affect the thermo-physical properties of the wick. For this reason, a great disagreement is found in literature between different

authors. Experimental tests are typically the best way to get an accurate evaluation of these properties.

2.3.3 Working fluids

The selection of a suitable fluid is one of the first and most important steps for the design of a thermal control system. Van Gerner, Van Benthem, and Es [14] developed a Figure of Merit (FoM) for two-phase loops as shown in equation 2.5. CO_2 has the highest figure of merit over a large part of the operating range. However, there are a number of fluids with a similar figure of merit, such as ammonia, N_2O, fluoromethane and ethane.

$$FoM = \left(\frac{\mu_l^{\frac{1}{4}}}{\rho_l h_{fg}^{\frac{7}{4}}} + \frac{\mu_v^{\frac{1}{4}}}{\rho_v h_{fg}^{\frac{7}{4}}} \right)^{-1} \tag{2.5}$$

Criteria that lead to the correct selection of the best fluid for a two-phase loop for space applications are several, such as thermal performance, mass of the system, power consumption of the pump, total occupied volume, availability, etc. Table 2.1 indicates the desired thermal properties of a two-phase fluid loop for the thermal management of space mission. Freezing temperature, vapor pressure and liquid specific heat are driving properties for an isothermal evaporator.

Chemical compatibility needs to be taken into account when selection a working fluid. Non-condensable gases might be generated and modify the working conditions of the evaporator if the wrong selection fluid/material is made. The generation of non-condensable gases depends on working fluid, surface area of the material, time of exposure and operating conditions [15]. Anderson [16] conducted life tests on 30 intermediate working fluids and over 60 fluid/material combinations. In general, there is a certain disagreement among several authors on the chemical compatibility of certain fluids with certain materials. In Table 2.2 an overview of the main material/fluid combinations studied and tested in literature is presented.

Table 2.1: Desired working fluid properties for a two-phase loop for space applications [3].

Property	**Small**	**Large**	**Reason**
Liquid density	x	-	lower mass
Vapor density	-	x	lower pressure drop
Thermal conductivity	-	x	higher h
Latent heat	-	x	lower mass and pressure drop
Liquid dynamic viscosity	x	x	higher h / lower pressure drop
Vapor dynamic viscosity	x	-	lower pressure drop
Liquid specific heat	x	-	easy sub-cooling
Vapor specific heat	-	x	lower temperature gradient in dry vapor
Boiling point	-	x	lower operating pressure
Freezing point	x	-	to reduce freeze concerns
Surface tension	-	x	to improve evaporator isothermality

Table 2.2: Material and fluid compatibility: c = compatible, i = incompatible.

	Water	Ammonia	Methanol	Acetone	Sodium	Potassium
Aluminum	i	c	i	c	-	-
Stainless steel	c	c	c	c	c	-
Copper	c	-	c	c	-	-
Nickel	c	c	c	-	c	c
Titanium	-	-	-	-	i	i

2.4 Heat transfer modeling of the evaporator

2.4.1 Analytical studies

Cao and Faghri [17] presented an analytical solution for a capillary pumped loop with a single phase fluid. In this study, a two dimensional porous enclosure was heated on part of its upper surface and had a fluid of constant velocity coming in the bottom permeable and isothermal surface. The vertical walls were impermeable and insulated. The portion of the top surface over which the heat flux occurred was impermeable, while the rest of the top surface was permeable. They found that the fluid flowed vertically into the porous structure, remained approximately one dimensional until the middle section, and then turned toward the permeable part of the upper surface. Since the upper surface was not permeable across the entire width, the fluid sped up as it turned. The authors also presented a relationship between the heat flux at the top surface and the mass flux of fluid coming out of the top.

Siedel, Sartre, and Lefèvre [15] developed a steady-state analytical model of a flat evaporator as part of a loop heat pipe. The originality of the investigation was in the combination of 2D analytic solutions, based on the expansion of Fourier series, of the temperature field in the evaporator with the energy balance equations for the other components of the loop. The results showed that convection inside the wick did not play a major role and the temperature field is uniform far from the vapor grooves. The presence of non-condensables gases leaded to an increase of the evaporator temperature in particular at lower heat loads.

2.4.2 Numerical studies

Tung and Dhir [18] obtained a finite element solution for phase change problems with two-dimensional fluid flow in porous media. The authors used a blocked porous channel in which the permeability was not constant. The partition in the channel did not cover the entire width, and it was observed that the fluid sped up as it went through the opening and slowed again on the other side. The drag models in conjunction with force balances on the two

phases were employed to obtain the void fraction and pressure gradients as functions of liquid and gas velocities.

Hanlon and Ma [8] built a 2D model for a sintered wick structure including heat conduction and capillary limitation to predict the overall heat transfer coefficient. Numerical results showed that the evaporative heat transfer can be enhanced by decreasing the average particle radius.

Ren, Wu, and Hu [19] developed a axis-symmetric two-dimensional model of a cylindrical evaporator. A finite volume method was built to discretize the enthalpy and pressure equations in the liquid and vapor regions. The authors observed that evaporation occurred along the porous interface with different intensity. Higher heat flux leaded to stronger convection and intense evaporation. The vapor receded into the wick when the effect of evaporation and conduction was predominant compared to the effect of convection within the wick.

Zhang, Li, and Wang [20] also investigated the heat transfer in a flat evaporator of a LHP. They built a numerical model assuming fully saturation of the porous structure and applying heat at the evaporator wall. The authors employed continuity, energy and Darcy's equations in the porous section of the evaporator. Contact between the solid and porous media was assumed perfect and heat losses were neglected. Numerical results showed that liquid flowing along the wick was superheated, the lowest temperature gradient were reached for a width ratio porous pillar-vapor groove equal to 1. The heat transfer coefficient of the a vapor groove included inside the wick is higher than that with a vapor groove inside the solid walls.

Figus et al. [21] built a pore network model to predict the liquid-vapor behaviour within the porous structure. When the wick was characterized by a uniform pore size, the network model results were consistent with a continuum model. However when there was a pore size distribution, pore network results showed fractal fronts of vapor within the wick.

Kaya and Goldak [22] numerically studied the heat and mass transfer in a capillary LHP and investigated the boiling limit. They solved mass, momentum, and energy equations with FE method investigating both all-liquid and vapor-liquid cases inside the wick by using the

cluster nucleation theory to determine the boiling limit.

Boubaker et al. [23] developed a two-dimensional mathematical model of a flat evaporator to simulate the heat transfer within the porous structure with phase change based on Langmuir's law. The authors presented the results for a sintered nickel wick with methanol working fluid. They observed that for low heat loads, the vaporization does not take place and the wick remains fully saturated with liquid, while above a certain critical value of heat load the upper part of the wick becomes fully saturated with vapor.

Nishikawara et al. [24] built a 3D numerical simulation with a pore network model for the case of wick fully saturated with liquid. The authors obtained that the evaporative heat transfer coefficient of the stainless steel wick was 10 times larger than the PTFE wick. On both cases the heat fluxes concentrated at the casing-wick-groove boundary. The authors also noticed a heat pipe effect along the wick fin for low heat fluxes allowing evaporation and condensation to take place.

2.5 Experimental studies of the heat transfer within the evaporator

Udell [25] studied a porous enclosure heated from above and cooled from below. Udell found that such an enclosure had three distinct regions at steady state. Near the top was a conduction dominated region with stationary superheated vapor. The middle region was two-phase, approximately isothermal, and convection dominated. Capillary forces pushed liquid components upward, while a pressure gradient forced vapor components downward. The bottom region was also conduction dominated and filled with compressed liquid. Udell also observed that the length of the two-phase region increased as the prescribed boundary heat flux was decreased.

Ramesh and Torrance [26] studied a porous enclosure heated from below and cooled from above to determine the interaction of boiling and convection. Torrance found that

vapor formed near the heated surface and observed the critical Rayleigh numbers for the onset of convection, mode switching, and oscillatory convection. He also observed that in low permeability media, a non-convecting liquid layer overlay the two-phase region, while in higher permeability media, convection initiated in the liquid region and penetrated into the two-phase zone.

Liao and Zhao [27] studied the temperature distribution of a porous block under different heat load conditions. He found that increasing the imposed heat flux leads to an increase of the heat transfer coefficient to a maximum value to decrease afterwards. The liquid-vapor interface moves towards the heated surface and when the critical heat flux is reached the vapor film expands covering the full heated surface. For a large hydrostatic heads, there is an optimal particle size for the maximum heat transfer coefficient. The critical heat flux increases with the decrease of the particle size. The height of the porous structure affects the critical heat flux but does not have influence on the maximum heat transfer coefficient. Increasing the inlet fluid temperature leads to an increase of both the heat transfer coefficient and the critical heat flux.

Odagiri and Nagano [28] presented an experimental study on the liquid-vapor interface in a capillary evaporator. Four samples of 5 mm height and 15 mm width were observed with a micro-scale IR camera. At low heat flux, the authors observed the presence of a liquid bridge in the vapor chamber between the heated plate and the porous pillar where evaporation occurred. At moderate heat flux small bubbles were generated at the contact between the solid and porous media while a smaller liquid bridge remained at the contact surface. At higher heat flux, nucleate boiling stopped and the liquid bridge disappeared. They sustained that the heat transfer coefficient reached a maximum when evaporation occurred at the surface of small liquid bridges and when nucleate boiling took place.

Li and Peterson [29] investigated the evaporation and boiling of porous media with wire structures at atmospheric pressure. The experimental results showed that the critical heat flux was strongly dependent on mesh size and volumetric porosity, while the evaporative heat transfer coefficient was only affected by the mesh size.

Boubaker, Harmand, and Platel [30] experimentally studied the heat and mass transfer with phase change in a copper foam cylindrical porous structure. The authors affirmed that porosity and pore diameter considerably impact the phase change phenomenon. They indicated that liquid sub-cooling negatively impacts the thermal performance of the capillary device, while an increase of the adverse hydrostatic pressure reduces the amount of liquid available to supply the liquid-vapor interface decreasing the performance of the evaporator.

Mottet, Coquard, and Prat [31] made a three-dimensional pore network model and compared it with an ad-hoc experimental setup. The experiments indicated that nucleation occurred under the casing at a certain distance from the vapor grooves as well as near the triple contact line casing-wick-groove.

Kumar et al. [32] designed an experimental setup and analyzed the thermal behaviour of a bi-porous wick using Infrared Thermography. The authors found out that the evaporative heat transfer coefficient at the fin-wick interface decreased with increase in heat inputs due to an increase of the thermal contact resistance under the heated surface with applied heat loads.

Giraudon et al. [33] investigated the effect of the characteristics of porous structures in a flat disk-shaped evaporator. Copper wicks were fabricated using the sintered powder technique, and water and pentane were used as working fluids. They found out that a high permeable wick is likely to reach the boiling limit before the capillary limit because the fluid easily percolates it. The fluid properties have a significant influence on the optimum heat transfer coefficient, for instance higher for pentane than water due to the higher wettability of pentane allowing it to easily wet the wick.

Table 2.3: Literature review of the heat and mass transfer studies on two-phase evaporators.

	Analytical	Numerical	Experimental	Steady state	Transient	2D	3D	AM wick	Contact resistance	Vapor penetration	HT vapor chamber	Gravity	Capillary based
Hanlon and Ma [8]	-	x	-	x	-	x	-	-	-	-	x	-	x
Siedel, Sartre, and Lefèvre [15]	x	-	-	x	-	x	-	-	x	-	-	x	x
Cao and Faghri [17]	x	-	-	x	-	x	-	-	-	-	-	-	x
Tung and Dhir [18]	-	x	-	x	-	x	-	-	-	-	-	x	x
Ren, Wu, and Hu [19]	-	x	-	x	-	x	-	-	-	-	x	x	x
Zhang, Li, and Wang [20]	-	x	-	x	-	x	-	-	-	-	-	-	x
Figus et al. [21]	-	x	-	x	x	x	-	-	-	x	-	x	x
Kaya and Goldak [22]	-	x	-	x	x	x	-	-	-	x	-	x	x
Boubaker et al. [23]	-	x	-	x	x	x	-	-	-	x	-	x	x
Nishikawara et al. [24]	-	x	-	x	-	-	x	-	-	-	-	x	x
Udell [25]	-	-	x	x	x	-	-	-	-	-	-	x	x
Ramesh and Torrance [26]	-	-	x	x	x	-	-	-	-	-	-	x	x
Liao and Zhao [27]	-	-	x	x	x	-	-	-	-	x	-	x	x
Odagiri and Nagano [28]	-	-	x	x	x	-	-	x	x	x	-	x	x
Li and Peterson [29]	-	-	x	x	x	-	-	-	x	x	-	x	x
Boubaker, Harmand, and Platel [30]	-	-	x	x	x	-	-	x	x	x	-	x	x
Mottet, Coquard, and Prat [31]	-	-	x	x	x	-	-	-	x	x	-	x	x
Kumar et al. [32]	-	-	x	x	x	-	-	-	x	x	-	x	x
Giraudon et al. [33]	-	-	x	x	x	-	-	x	x	x	-	x	x

2.6 Conclusions

The literature survey presents the complexity of the heat transfer within the porous structure of evaporators as part of a LHP system. Several analytical and numerical studies were undertaken to investigate the steady-state and sometimes transient behaviours of the evaporative and boiling heat transfer in porous structures. Several experimental setups were built in order to validate the numerical models under simplified boundary conditions. However a common denominator is the difficulty to get a good understanding of the heat and mass transfer in porous media due to the underlying uncertainties related to the evaporative heat transfer, the wick properties such as effective thermal conductivity, pore distribution, and contact resistance between the solid and porous walls. One additional source of uncertainty is related to the heat losses to the ambient that take a relevant role in the heat transfer within the evaporator in particular at low heat loads. Many experimental studies, tempted by the need to observe the behaviour of the liquid-vapor interface, introduced relevant heat leaks to the observed systems. Heat transfer within the porous structure not only depends on the wick properties (such as permeability, pore size, porosity), on the geometric features of the porous, liquid and vapor chambers and on the fluid properties but also on the contact resistance between the solid and porous structures, heat losses through the case, etc. An accurate evaluation of the heat and mass transfer between the several components of the evaporator is necessary.

Chapter 3

Heat Transfer Modeling in the Wick

3.1 Introduction

The evaporator design influences the thermal characteristics of the overall Two-Phase Mechanically Pumped Loop. Heat conduction within the wick transfers heat from the pillar to the wick-groove interface, as shown in Figure 3.1, while convection of the cooling liquid transports liquid from the inlet to the interface. The behaviour of the interface is a result of the combining effect of evaporation, heat conduction and convection. Evaporation occurs everywhere on the interface with different intensity of evaporation. It vaporizes more strongly in the region closer to the center of the heat source. Unlike a Loop Heat Pipe (LHP), the pressure across the meniscus is not simply equal to the pressure drop across the system, but it is a more complex function of flow resistances, pumped flow rate and heat load.

The location and the shape of the liquid-vapor interface in the evaporator can have significant influence on the heat transfer inside the wick and is mostly of interest when investigating the deprive of the loop following the drying out of the porous structure. Input heat loads lead to evaporation of the working fluid, and capillary force at the menisci drives the working fluid to flow. The growth of vapor zones inside the wick leads to a different thermal profile in the wick, to a change of the evaporation interface shape and, in case of a

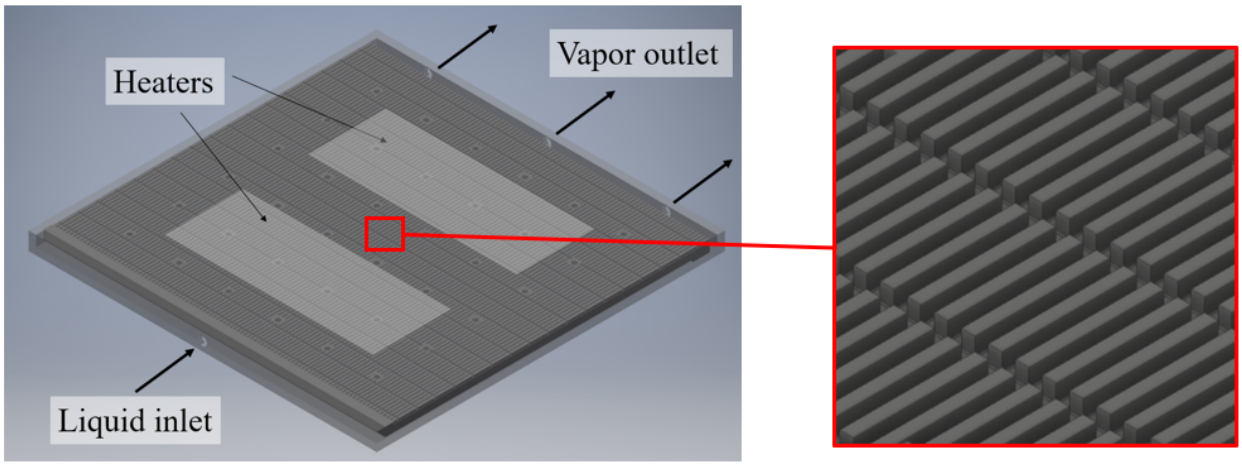

Figure 3.1: Evaporator layout: global view and zoom of the wick pillars.

penetration across the entire porous structure, to a failure of the entire loop operation. In the capillary porous media, the interface adapts itself to steady states at different heat fluxes automatically by two means: it changes the curvature menisci or its position in the porous media to adjust the flux of the working fluids. The change of the curvature of the menisci appears when the curvature of menisci is between the minimum and maximum curvature, and the interface will not move when the curvature is greater than the maximum curvature or smaller than the minimum curvature. When effect of evaporation and heat conduction is stronger than effect of convection, a vapor blanket invades deeply into the wick.

The goal of this chapter is to present and discuss the mathematical formulation of the heat transfer within the porous structure when the liquid-vapor interface is located at the border between the wick and vapor groove interface (operational scenario). A particle level model along the evaporative boundary allows to understand the fundamental aspects of the heat and mass transfer of the evaporation process. The results are discussed for the case of the JPL evaporator and a parametric study has been performed to understand the effect of boundary conditions, geometry, wick and fluid properties on the heat transfer.

3.2 Wick model

3.2.1 Assumptions

A capillary porous structure with partial heating and evaporation on the upper surface is shown in Figure 3.2. The entire porous structure is saturated with liquid from the bottom, which is connected to a pool for the liquid supply. Heat is applied on the external surface of the evaporator (as shown in Figure 3.1) and is transferred to the wick pillar and then towards the liquid-vapor interface located at the wick-to-vapor groove boundary. The liquid is drawn from the bottom of the porous structure and flows to the liquid-vapor interface due to evaporation.

The following assumptions are made:

1. the process is steady-state
2. the capillary structure is homogeneous and isotropic
3. the radiative and gravitational effects are negligible
4. the fluid is Newtonian and has constant properties at each phase.

In addition, there are other assumptions in the present model involving the boundary conditions, the properties of the porous structure and the liquid-vapor interface, which are listed below:

1. the wick structure is perfectly saturated
2. the liquid-vapor interface has zero thickness
3. the sharp discontinuities of the properties are maintained across the interface
4. the temperature at the liquid-vapor interface (here the wick interface) is the saturation temperature corresponding to the local static pressure

5. with the exception of the bottom of the evaporator substrate and the top surface of the liquid in the compensation chamber, all other thermal boundary conditions are chosen as adiabatic condition.

3.2.2 Mathematical formulation

In the evaporator the temperature increases along the direction from the liquid inlet to the porous pillar. There are two-dimensional patterns of isotherms in the proximity of the pillar and the vapor groove. At low heat fluxes, the effect of heat conduction of the porous media is stronger than the effect of convection of the working liquid in the wick. At moderate heat fluxes, the effect of heat conduction of the porous media is stronger than the effect of convection of the working liquid in the proximity of the pillar, where temperature increases with increasing heat flux.

The wick structure in the evaporator can be represented by a two-dimensional elementary cell (Figure 3.2) due to geometrical and physical symmetry. During nominal operation, the wick domain is fully saturated with liquid and the liquid-vapor interface is located at the boundary between the vapor groove and the wick. The fluid flow in the wick is determined based on continuity, Darcy and advection-diffusion equations. Evaporation occurs along the top interface with variable intensity, increasing in proximity of the heat source. The heat transfer is a result of the combination of evaporation, heat conduction within the porous media and convection of the cooling working liquid.

Figure 3.2 illustrates the wick structure domain Ω composed of a porous base with L_x width and L_y thickness and a porous pillar with L_{xp} width and L_{yp} height. The origin of the global coordinate system (x, y) is located at the bottom left corner of the domain. A local coordinate system (t, n) is also adopted to represent the tangential and normal directions at the wick interface along the evaporative boundary. Heat is applied uniformly on the top edge of the pillar, while evaporation is taking place along the interface between the wick and the vapor groove. The side walls are adiabatic and impermeable (symmetry condition).

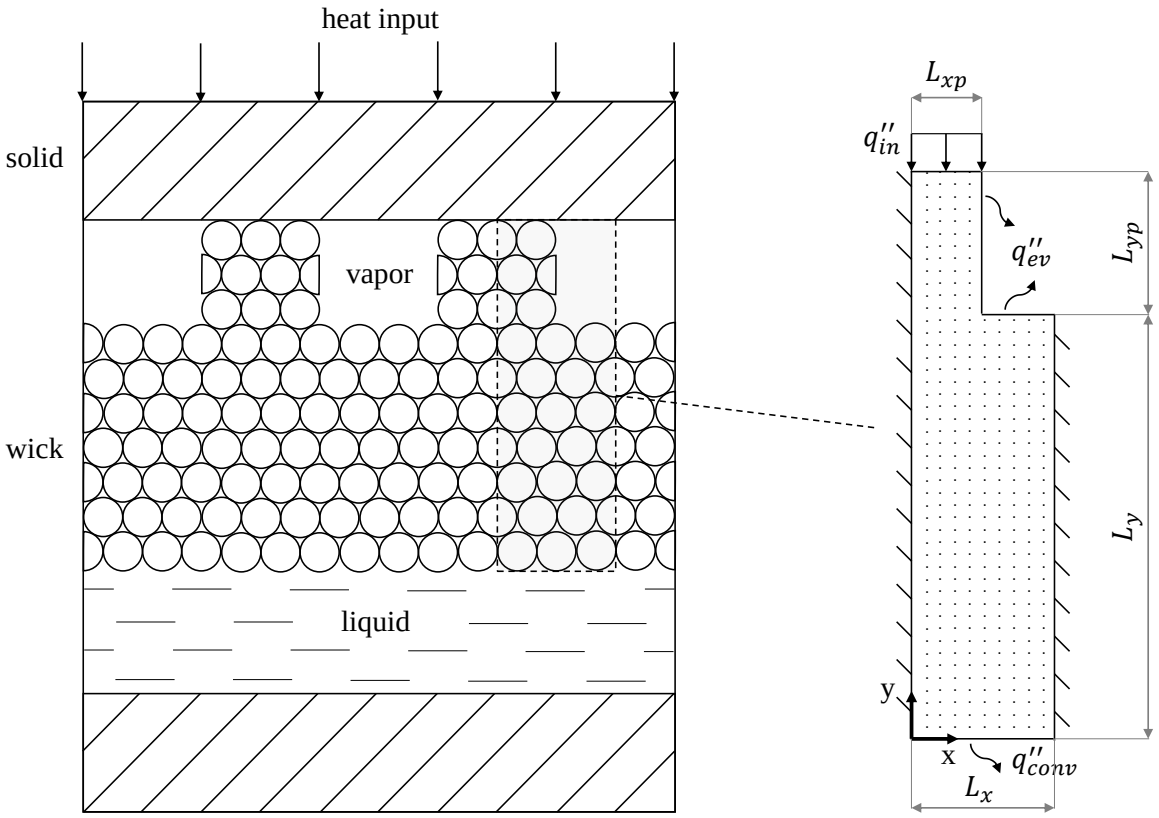

Figure 3.2: Schematic of the elementary cell of the wick domain.

The liquid flows throughout the wick domain from the bottom boundary, where the liquid chamber is located, up to the liquid-vapor interface due to evaporation. In order to sustain the liquid flow, the capillary pressure must be equal or greater than the sum of all other pressure drops. On the bottom side of the domain, convection is taking place where liquid pressure and temperature are known. This configuration represents the nominal operational case in which the wick structure is working far from the incipience of boiling. Bubble formation will not occur in the wick if the difference between the maximum temperature and the saturation temperature is less than the superheat for nucleation. In the event this condition is not respected, vapor would be generated within the domain resulting in an increase of the thermal resistance and decrease of the efficiency of evaporation at the liquid-vapor-solid interface.

The liquid flow in the porous structure can be described by the continuity equation

$$\frac{\partial u}{\partial x} + \frac{\partial v}{\partial y} = 0 \tag{3.1}$$

coupled with the Darcy's law with gravity neglected

$$u = \frac{K}{\mu}\left(-\frac{\partial P}{\partial x}\right) \tag{3.2}$$

$$v = \frac{K}{\mu}\left(-\frac{\partial P}{\partial y}\right) \tag{3.3}$$

where K is the wick permeability, determined by particle packing, sorting and particle size:

$$K = R_{part}^2 \frac{\varepsilon^3}{37.5(1-\varepsilon)^2} \tag{3.4}$$

where R_{part} is the particle radius and ϵ the porosity. The above relationship is valid for unconsolidated packed, spherical particles, plain or sintered, with a diameter spanning between 50 μm and 300 μm and porosity between 27 and 66 % [6]. The particle radius is assumed to be four times the pore radius due to geometrical considerations valid for spherical particles. The energy equation is

$$u\frac{\partial T}{\partial x} + v\frac{\partial T}{\partial y} = \alpha_e\left(\frac{\partial^2 T}{\partial x^2} + \frac{\partial^2 T}{\partial y^2}\right) \tag{3.5}$$

where the effective thermal diffusivity α_e is defined as,

$$\alpha_e = \frac{k_e}{\rho_l c_p} \tag{3.6}$$

where the effective thermal conductivity k_e is calculated as,

$$k_e = \frac{k_s(2k_s + k_l - 2\epsilon\,(k_s - k_l))}{2k_s + k_l + \epsilon(k_s - k_l)} \tag{3.7}$$

where k_s and k_l are respectively the thermal conductivities of the solid and liquid phases. It is valid for sintered metal powder wicks and it has been confirmed experimentally by Gorring and Churchill (1961) [6].

In the above formulation, it is assumed that the porous structure is homogeneous and isotropic. It is also assumed that the solid matrix is in local thermal equilibrium with the

fluid filling the pores, and the order of the local Reynolds number based on the average velocity does not exceed unity.

The boundary conditions can be expressed at the heat input, convective and adiabatic borders respectively as,

$$\begin{cases} -k_e \frac{\partial T}{\partial y} = q''_{in} & \text{for } y = L_y + L_{yp} \text{ and } x \in [0, L_{xp}] \\ -k_e \frac{\partial T}{\partial y} = h_{conv}(T - T_l) & \text{for } y = 0 \\ \frac{\partial T}{\partial x} = 0 & \text{for } x = 0 \text{ and } x = L_x \end{cases} \tag{3.8}$$

while the pressure boundary conditions are

$$\begin{cases} \frac{\partial P}{\partial y} = 0 & \text{for } y = L_y + L_{yp} \text{ and } x \in [0, L_{xp}] \\ P_l & \text{for } y = 0 \\ \frac{\partial P}{\partial x} = 0 & \text{for } x = 0 \text{ and } x = L_x \end{cases} \tag{3.9}$$

where T_l and P_l are respectively the temperature and pressure of the liquid chamber, q''_{in} is the imposed heat flux and h_{conv} is the convective heat transfer at the bottom boundary calculated from

$$Nu = 7.54 + \frac{0.03\left(\frac{D_h}{L} RePr\right)}{1 + 0.016\left[\left(\frac{D_h}{L}\right) RePr\right]^{\frac{2}{3}}} \tag{3.10}$$

valid for laminar flow ($Re < 2800$) between isothermal parallel plates [6].

The evaporative pressure boundary conditions are calculated considering the mass balance and the Darcy flow equation,

$$q''_{ev} = -k_e \left.\frac{\partial T}{\partial n}\right|_{\partial\Omega_{ev}} = \dot{m}_l h_{fg} = \rho_l u_l h_{fg} = \rho_l \left(-\frac{K}{\mu} \left.\frac{\partial P}{\partial n}\right|_{\partial\Omega_{ev}}\right) h_{fg} \tag{3.11}$$

that becomes a boundary condition for the pressure field

$$\left.\frac{\partial P}{\partial n}\right|_{\partial\Omega_{ev}} = \frac{k_e}{K}\frac{\mu}{\rho_l h_{fg}} \left.\frac{\partial T}{\partial n}\right|_{\partial\Omega_{ev}} \tag{3.12}$$

and the boundary condition for the temperature field is

$$-k_e \left.\frac{\partial T}{\partial n}\right|_{\partial\Omega_{ev}} = h_{ev}(T - T_{sat}) \tag{3.13}$$

where q''_{ev} is the evaporative heat flux, n is the normal direction to the evaporative boundary $\partial\Omega_{ev}$, $\dot{m}_l$ is the liquid mass flow rate, T_{sat} is the saturation temperature and h_{ev} is the evaporative heat transfer coefficient, calculated directly from the kinetic gas theory. It is a function of the fluid properties at a given pressure:

$$h_{ev} = \left(\frac{2\hat{a}}{2-\hat{a}}\right)\left(\frac{\widetilde{M}}{2\pi\widetilde{R}T_{sat}}\right)^{\frac{1}{2}}\rho_v\frac{h_{fg}^2}{T_{sat}} \tag{3.14}$$

where $\widetilde{M}$ and $\widetilde{R}$ are respectively the molecular weight and the universal gas constant, and $\hat{a}$ is the accommodation coefficient, defined as the ratio between the actual evaporation rate and the theoretical maximum phase change rate [6]. Its value depends on the surface nature and state, but it is also affected by the composition and pressure of the gas mixture in the environment and other parameters. For these reasons, the values of $\hat{a}$ differ widely in literature and a precise evaluation of the accommodation coefficient is not trivial. Paul [34] reported a collection of $\hat{a}$ values valid for many working fluids and Mills and Seban [35] concluded that the accommodation coefficient should be smaller than unity when the fluid or the interface is contaminated. In this model the accommodation coefficient $\hat{a}$ is assumed equal to 0.1.

3.2.3 Dimensionless analysis

The above reported mathematical formulation can be reported into dimensionless form. The advantage of this formulation is the identification of the main dimensionless numbers that affect the heat and mass transfer within the elementary cell of the evaporator. Firstly, the coordinate system can be expressed as,

$$X^* = \frac{x}{L_x} \tag{3.15}$$

$$Y^* = \frac{y}{L_y} \tag{3.16}$$

The following geometrical ratios can be introduced,

$$\Pi_1 = \frac{L_x}{L_y} \tag{3.17}$$

$$\Pi_2 = \frac{L_{xp}}{L_x} \tag{3.18}$$

$$\Pi_3 = \frac{L_{yp}}{L_y} \tag{3.19}$$

A set of reference values can be defined based on permeability, porosity, effective thermal conductivity and liquid properties. Following Udell [25] definition, the characteristic pore diameter can be written as,

$$d_0 = \left(\frac{K}{\varepsilon}\right)^{1/2} \tag{3.20}$$

the characteristic capillary pressure is

$$P_0 = \frac{\sigma}{d_0} = \frac{\sigma}{\left(\frac{K}{\varepsilon}\right)^{1/2}} \tag{3.21}$$

the characteristic liquid velocity is

$$v_0 = \frac{K\ P_0}{\mu_l L_y} = \frac{(K\varepsilon)^{1/2}\,\sigma}{\mu_l L_y} \tag{3.22}$$

and the characteristic temperature is

$$\Delta T_0 = T_{max} - T_v \tag{3.23}$$

where $T_{max} = T(0, L_y + L_{yp})$ is the maximum temperature located at the left-top corner of the domain, $T_v = T_{sat}(P_v)$ is the vapor temperature equivalent to the saturation temperature at pressure P_v and ΔT_0 is the maximum allowable temperature difference defined by the boiling limit. The main dimensionless variables are:

$$T^* = \frac{T - T_v}{\Delta T_0} \tag{3.24}$$

$$P^* = \frac{P}{P_0} = \frac{P\ \left(\frac{K}{\varepsilon}\right)^{1/2}}{\sigma} \tag{3.25}$$

$$u^* = \frac{u}{v_0} = \frac{u\ \mu_l\ L_y}{\sigma\ (K\varepsilon)^{1/2}} \tag{3.26}$$

$$v^* = \frac{v}{v_0} = \frac{v\ \mu_l\ L_y}{\sigma\ (K\varepsilon)^{1/2}} \tag{3.27}$$

The governing equations can be rewritten in a non-dimensional formulation. The dimensionless continuity equation is

$$\frac{\partial u^*}{\partial X^*} + \Pi_1 \frac{\partial v^*}{\partial Y^*} = 0 \tag{3.28}$$

and the dimensionless momentum equations, neglecting inertia, are

$$u^* = -\left(\frac{1}{\Pi_1}\right)\frac{\partial P^*}{\partial X^*} \tag{3.29}$$

$$v^* = -\frac{\partial P^*}{\partial Y^*} \tag{3.30}$$

The dimensionless energy equation is

$$\left(\frac{1}{\Pi_1}\right)u^*\frac{\partial T^*}{\partial X^*} + v^*\frac{\partial T^*}{\partial Y^*} = \frac{1}{Pe}\left(\left(\frac{1}{\Pi_1}\right)^2\frac{\partial^2 T^*}{\partial X^{*2}} + \frac{\partial^2 T^*}{\partial Y^{*2}}\right) \tag{3.31}$$

where the Peclet number Pe is defined as,

$$\Pi_4 = Pe = RePr = \frac{\rho_l c_p \sigma}{\mu_l}\frac{(K\varepsilon)^{1/2}}{k_e} \tag{3.32}$$

The convective boundary conditions become

$$-\frac{\partial T^*}{\partial Y^*} + h_{conv}\frac{L_y}{k_e}\left(T^* + \frac{T_v - T_l}{T_{max} - T_v}\right) = 0 \tag{3.33}$$

and

$$P^*(X^*, 0) = P_l^* \tag{3.34}$$

where the convective dimensionless number is defined as

$$\Pi_5 = h_{conv}\frac{L_y}{k_e} \tag{3.35}$$

The dimensionless evaporative boundary conditions are

$$\begin{cases} \frac{\partial P^*}{\partial X^*} = \frac{1}{Ev}\frac{\partial T^*}{\partial X^*} & \text{for } X^* = \Pi_2 \text{ and } Y^* \in [1, 1+\Pi_3] \\ \frac{\partial P^*}{\partial Y^*} = \frac{1}{Ev}\frac{\partial T^*}{\partial Y^*} & \text{for } X^* \in [\Pi_2, 1] \text{ and } Y^* = 1 \end{cases} \tag{3.36}$$

where the evaporation number Ev is defined as,

$$\Pi_6 = Ev = \frac{1}{(T_{max} - T_v)}\frac{\rho_l h_{fg}\sigma}{\mu_l}\frac{(K\varepsilon)^{1/2}}{k_e} \tag{3.37}$$

and

$$\begin{cases} \frac{\partial T^*}{\partial X^*} = \left(h_{ev}\frac{L_x}{k_e}\right) T^* & \text{for } X^* = \Pi_2 \text{ and } Y^* \in [1, 1+\Pi_3] \\ \frac{\partial T^*}{\partial Y^*} = \left(h_{ev}\frac{L_y}{k_e}\right) T^* & \text{for } X^* \in [\Pi_2, 1] \text{ and } Y^* = 1 \end{cases} \tag{3.38}$$

where

$$\begin{cases} \Pi_7 = h_{ev}\frac{L_x}{k_e} \\ \Pi_8 = h_{ev}\frac{L_y}{k_e} \end{cases} \tag{3.39}$$

At the heat input boundary, the dimensionless boundary conditions are:

$$\frac{\partial T^*}{\partial Y^*} = \frac{q_{in}}{-k_e\frac{\Delta T_0}{L_y}} \tag{3.40}$$

and

$$\frac{\partial P^*}{\partial Y^*} = 0 \tag{3.41}$$

The adiabatic dimensionless boundary conditions are

$$\frac{\partial T^*}{\partial X^*} = \frac{\partial P^*}{\partial X^*} = 0 \tag{3.42}$$

The dimensionless analysis shows the problem dependence on eight dimensionless numbers. Boundary conditions, geometrical configuration, porous and fluid properties affect the performance and the thermal behaviour of the evaporator. These parameters will be presented and discussed in the rest of the chapter.

3.3 Particle-level model

Once the temperature and pressure fields have been solved with the global wick model, it is necessary to include the effect of the meniscus shape along the evaporative boundary. The particle-level model, valid at the evaporative boundary, adds the boundary effect of the liquid-vapor interface on momentum and energy equations solved in the wick model. The following assumptions are made:

1. the process is steady-state

2. convection in the liquid domain is negligible (only conduction)

3. convection between the solid walls of the particle and the vapor is negligible

4. the liquid-vapor interface has zero thickness

5. the sharp discontinuities of the properties are maintained across the interface

6. the temperature at the liquid-vapor interface is the saturation temperature corresponding to the local static pressure

7. thermal properties of the solid and liquid components are constant.

The temperature T_b is equivalent to the average temperature at one particle diameter away from the evaporative boundary. It is assumed to be equal along the three sizes of the domain for simplicity of the calculations. The effect of the temperature variation along the evaporative boundary is accounted when solving the wick model together with the particle model.

3.3.1 Mathematical formulation

Figure 3.3 illustrates the computational domain of the heat transfer of a particle with radius R_{part} and a meniscus at an angular position α. Assuming no convection in the liquid phase, the mathematical formulation of the problem is the following:

$$\frac{\partial^2 T}{\partial x^2} + \frac{\partial^2 T}{\partial y^2} = 0 \tag{3.43}$$

with the following boundary conditions,

$$\begin{cases} T(0, y) = T_b & \text{for } x = 0 \\ T(2R_{part}, y) = T_b & \text{for } x = 2R_{part} \\ T(x, -R_{part}) = T_b & \text{for } y = -R_{part} \\ -k_l \frac{\partial T}{\partial n} = h_{ev}(T - T_{sat}) & \text{at } \partial\Omega_{ev} \\ \frac{\partial T}{\partial n} = 0 & \text{at } \partial\Omega_{ad} \end{cases} \tag{3.44}$$

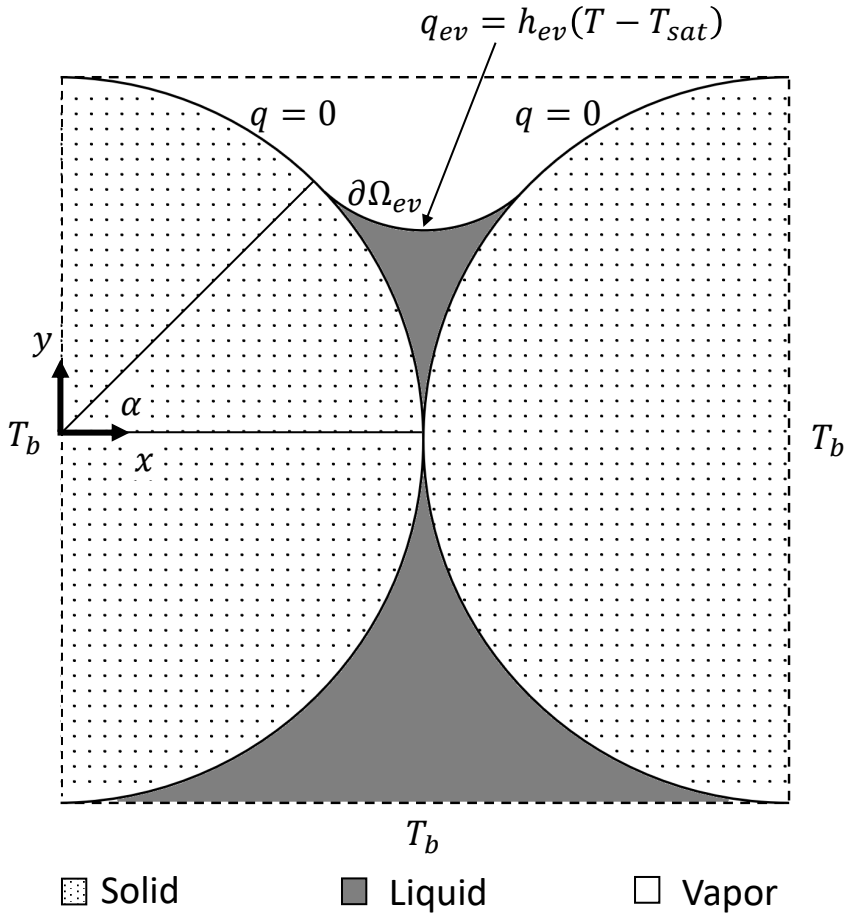

Figure 3.3: Particle model and boundary conditions.

where R_{part} is the particle radius, n is the normal vector to the liquid-vapor interface, T_b is the known temperature at the base of the particle and at the liquid inlet, T_{sat} is the saturation temperature and h_{ev} is the evaporative heat transfer coefficient.

Figure 3.5 illustrates the temperature mapping of a particle of radius R_{part} = 50 μm, meniscus angular position $\alpha = 60°$, temperature T_b = 26.2 °C, liquid thermal conductivity k_l = 0.48 W/m-K and solid thermal conductivity k_s = 80 W/m-K. Thanks to the high thermal conductivity of the solid particle, it is possible to notice the main temperature gradient is in the region below the evaporative boundary on the liquid side (Figure 3.6).

Figure 3.7 and Figure 3.8 show respectively the evaporative heat flux along the evapo-

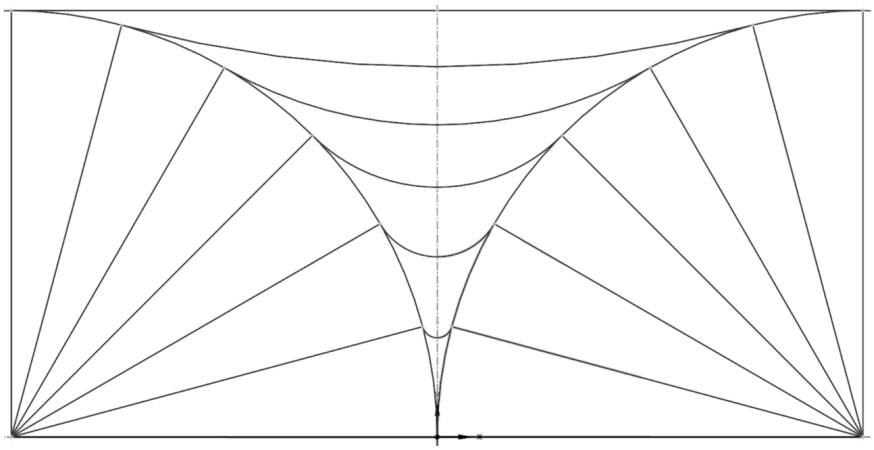

Figure 3.4: Meniscus shapes at different α.

rative boundary $\partial\Omega_{ev}$ and the top boundary $\partial\Omega_{top}$ (adiabatic regions included) for different T_b and α. It is possible to notice that α does not affect the maximum and minimum heat fluxes and temperature values, however it affects the overall evaporative heat load due to the extension of the evaporative domain.

The relationship between α and meniscus radius is calculated as follows:

$$r_m = \frac{R_m}{R_{part}} = \frac{(1 - \cos\alpha)}{\cos\alpha} \tag{3.45}$$

where R_m is the mean radius of the meniscus in the capillary pressure equation

$$P_c = P_{nw} - P_w = \frac{2\sigma}{R_m} \tag{3.46}$$

where P_{nw} and P_w are the non-wetting and wetting phases of two immiscible fluids.

Based on the Darcy's law it is possible to calculate the velocity of the liquid and consequently the liquid mass flow rate along the wick domain. During nominal conditions the liquid mass flow rate $\dot{m}_l$ has to be equal to the vapor mass flow rate $\dot{m}_v$ calculated by the particle model. In other words, the heat load $Q_{ev} = \dot{m}_l h_{fg}$ equals the Q_{ev}^{part}. This relationship can only be satisfied by a univocal meniscus radius or α angle at a given position along the evaporative boundary.

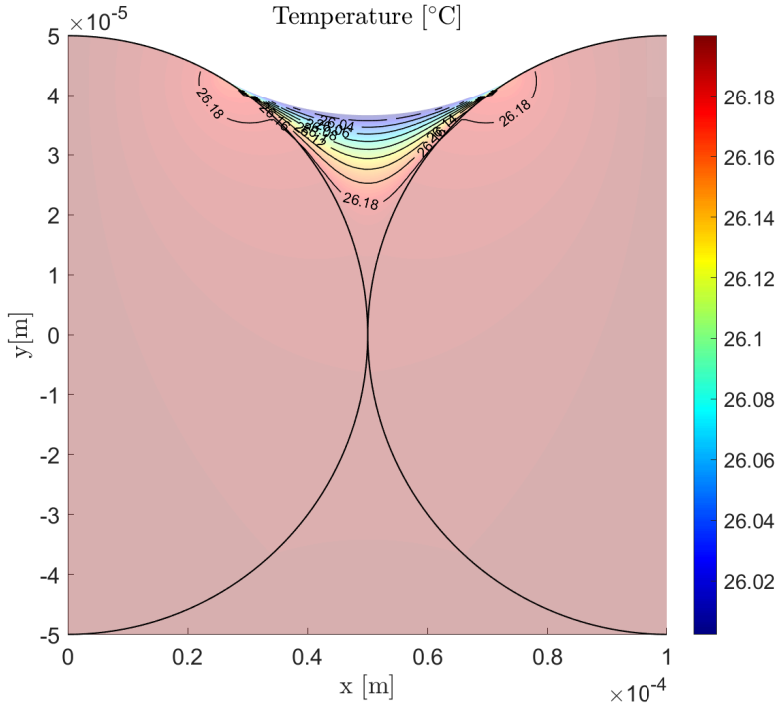

Figure 3.5: Temperature mapping within the particle model

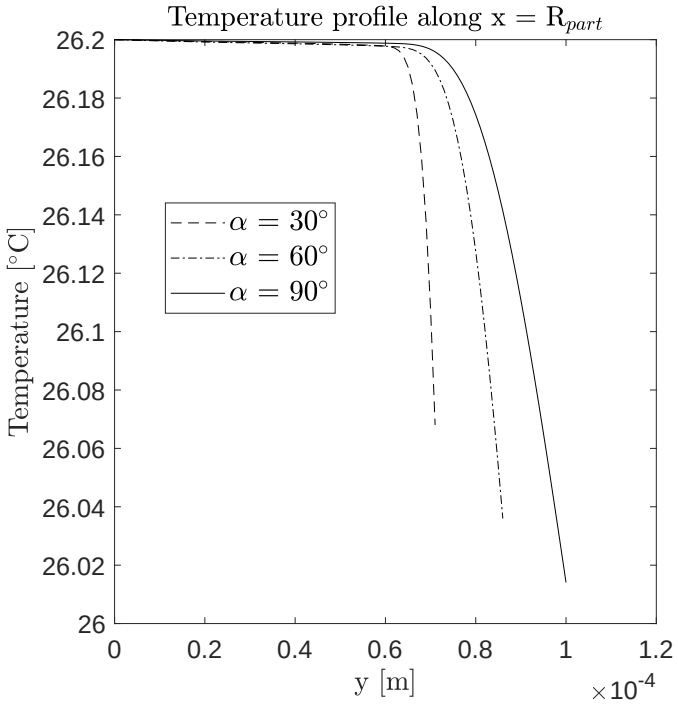

Figure 3.6: Temperature profiles along the y-axis for different α.

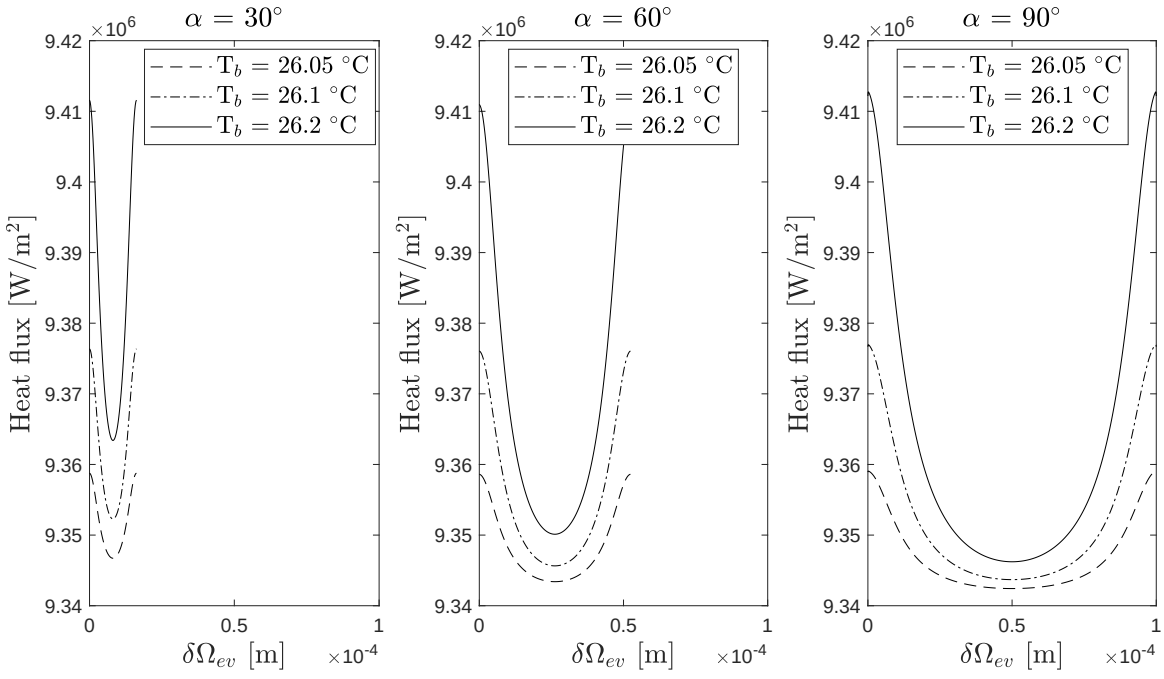

Figure 3.7: Evaporative heat flux along the interface $\delta\Omega_{ev}$ for different T_b and α.

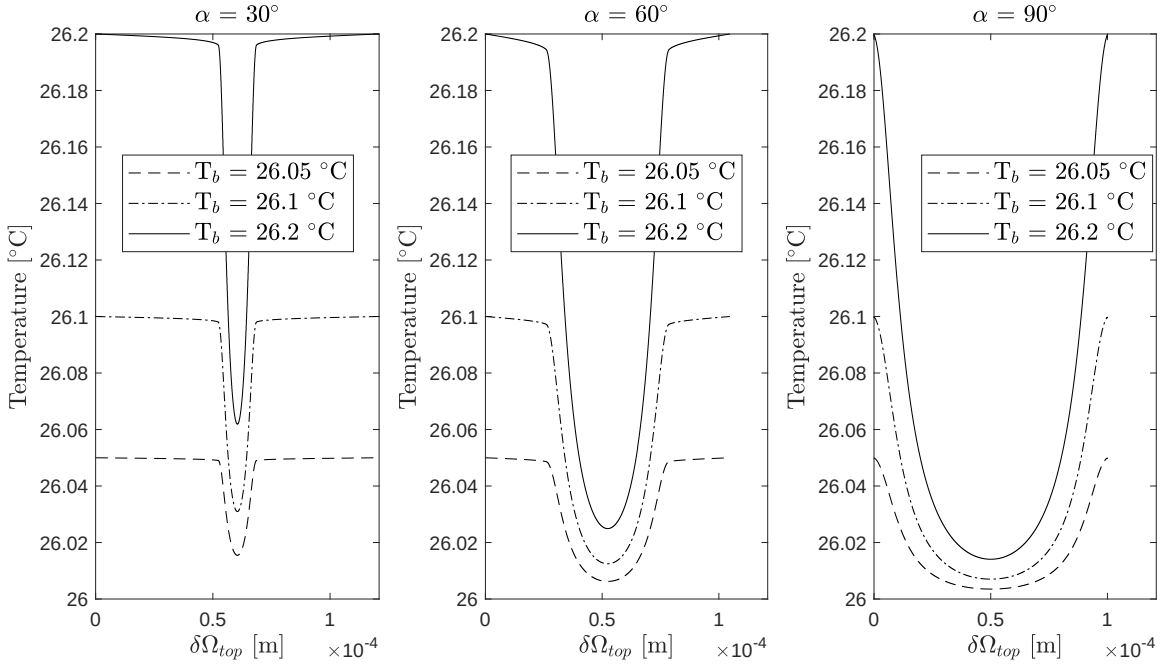

Figure 3.8: Temperature along the top boundary $\delta\Omega_{top}$ for different T_b and α.

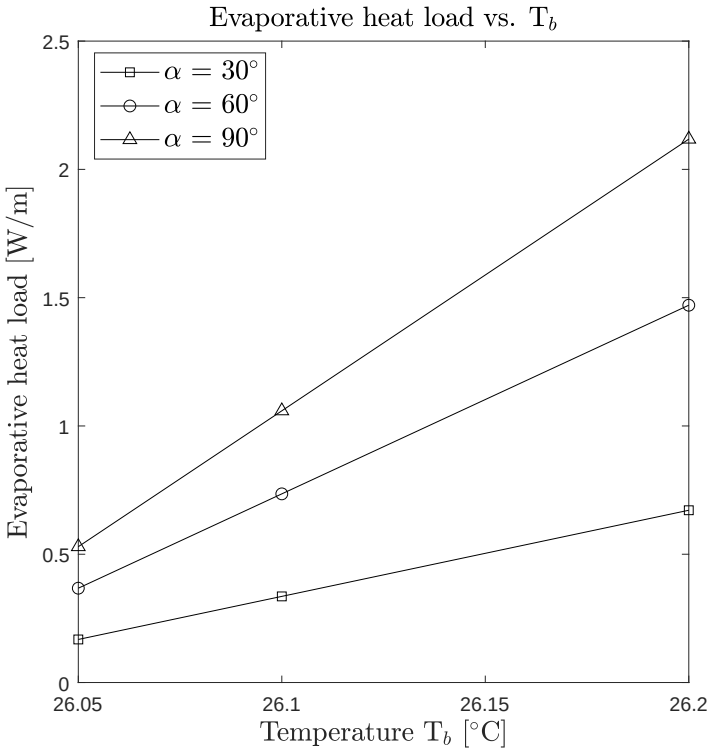

Figure 3.9: Evaporative heat load as function of temperature for different α.

Figure 3.9 summarizes the relationship between the evaporative heat load and the base temperature T_b for different α. Higher α angles lead (theoretically) to higher evaporative heat loads, but the actual limit depends on capillary pressure considerations. For instance, even if $\alpha = 90°$ would allow a higher evaporative heat load, the capillary pressure equal to zero (no curvature) would not create a condition of liquid flow from the bottom inlet to the liquid-vapor interface.

Figure 3.9 also provides the unique input relationships between Q_{ev}^{part} and T_b for several α angles that will be used in the global wick model as part of the iterative method, as described in more details in the coming paragraphs.

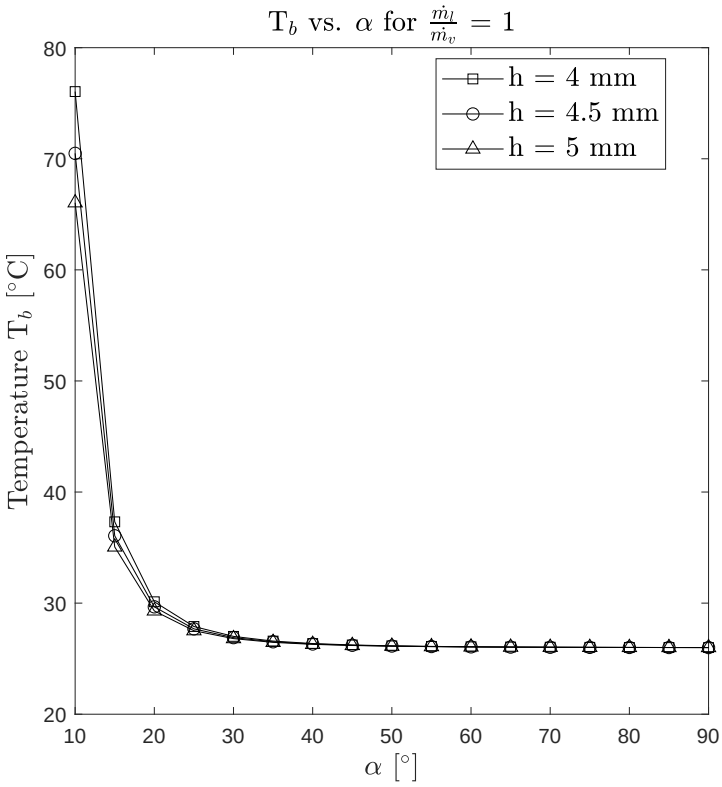

Figure 3.10: Temperature T_b as function of α along the evaporative heat boundary of the wick model.

Figure 3.10 summarizes the relationship between the base particle temperature T_b and the α angle for different locations along the evaporative boundary of the wick domain. In an operational condition, liquid mass flow rate $\dot{m}_l$ has to be equal to the vapor mass flow rate $\dot{m}_v$. In other words, the liquid mass flow rate calculated through the Darcy's law and the capillary pressure has to be equal to the amount of vapor produced by the interface at particle level.

It is possible to notice that the base temperature T_b, able to sustain a ratio $\frac{\dot{m}_l}{\dot{m}_v} = 1$, decreases with α up to the saturation temperature $T_{sat} = 26$ °C at $\alpha = 90°$. While T_b increases exponentially below $\alpha = 30°$ reaching 76 °C at $\alpha = 10°$. This means that dry-out is likely to occur before in the wick at the boundary where the heat input is applied than the evaporative boundary.

3.4 Numerical algorithm

The heat and mass transfer in the porous structure is solved through a 2D Finite Difference scheme built in MATLAB/QuickerSim Toolbox [36] and counts 10^5 elements throughout the domain with a spatial resolution of 0.01 mm per cell.

The algorithm takes as input parameters pressure and temperature on the liquid side, pressure in the vapor groove, imposed heat flux at the top boundary of the pillar and material properties (from REFPROP Thermal Fluid Properties Database [37]).

After an initial guess on the temperature field, the pressure field within the porous domain Ω is solved with the Dirichlet condition at the convective boundary and the evaporative boundary condition (equation 3.12). Knowing the pressure field, velocity is calculated thanks to the Darcy's law. Based on the computed velocity field, the advection-diffusion equation for the temperature field is determined by the convective heat transfer at the liquid chamber, the heat load input and the evaporative heat transfer boundary condition.

Once the wick model has achieved its convergence, the temperature profile located at one particle diameter under the evaporative boundary is extracted. This temperature profile becomes the input to relationship between the evaporative heat load and the base temperature T_b calculated through the particle model (see Figure 3.9 and Figure 3.10) with the condition that the liquid mass flow rate $\dot{m}_l$ has to be equal to the vapor mass flow rate $\dot{m}_v$. The new evaporative heat load along the evaporative heat boundary is calculated and becomes the new boundary condition to the wick model for the energy field. The process is re-iterated till convergence.

The convergence criteria are achieved when the maximum relative change of temperature is less than 10^{-8} and the energy balance is satisfied.

3.4.1 Solving procedure

The heat and mass transfer within the porous structure and, in particular, the evaporative heat load can be calculated with the following procedure:

Step 1: Initialize the input parameters such as boundary conditions, fluid and wick properties, geometrical domain.

Step 2: Solve the momentum equation with the relative BCs.

Step 3: Calculate the velocity field through Darcy's law.

Step 4: Solve the energy equation with the relative BCs.

Step 5: Reiterate till convergence criteria are satisfied (maximum relative change of temperature is less than 10^{-8} and the energy balance is satisfied).

Step 6: Extract the temperature profile parallel to the evaporative boundary at a distance equivalent to one diameter of the particle D_{part}.

Step 7: Split the temperature profile extracted at Step 6 into N elements equal to (length of evaporative boundary) / particle diameter.

Step 8: Based on the relationships between T_b and α calculated through the particle-level model with the condition $\frac{\dot{m}_l}{\dot{m}_v} = 1$, calculate the new evaporative heat load along the evaporative boundary.

Step 9: Re-iterate the calculation of the momentum and energy fields in the wick model using the new evaporative heat load profile.

Step 10: Re-iterate till convergence criteria are satisfied (maximum relative change of temperature is less than 10^{-8} and the energy balance is satisfied).

3.5 Baseline case study

The numerical domain here presented is 1 x 4 mm for the porous base and 0.5 x 1 mm for the porous pillar. The aluminum wick is fully saturated with liquid ammonia. Pressure in the liquid chamber and in the vapor groove is at 10.345 bar, while temperature at the liquid inlet is 24 °C. The liquid properties are reported in Table 3.1 and the saturation temperature T_{sat} is equal to 26 °C. This configuration (that corresponds to the configuration described in Table 3.2) represents the baseline evaporator and 2PMPL conditions tested at JPL, and previously reported [4].

The numerical simulations indicate that the maximum temperature occurs at the upper-left corner, as shown in Figure 3.12. Fluid flow is nearly one-dimensional throughout the wick, except in proximity of the boundary where the heat load is applied, and the x-component of velocity becomes important.

Figure 3.13 shows the temperature profile along x = 0 for different heat flux inputs applied at the top edge of the wick pillar. It is possible to notice that the temperature gradient is significant in the region of the wick pillar. For imposed heat fluxes of 4 and 6 W/cm^2, the maximum temperatures in the domain are respectively 26.2 and 26.4 °C. Note that in this system configuration (assuming an uniform 3.8 μm effective pore radius), nucleation in the wick begins when the superheat (T – T_{sat}) in the wick exceeds 0.35 °C, equivalent to an input heat flux of 5 W/cm^2.

Figure 3.14 illustrates that the temperature along the evaporative boundary is slightly above the saturation temperature of 26 °C as expressed by equation 3.13. The majority of heat transfer is occurring in the first top half of the pillar border (within 0.5 mm).

When evaporation takes place, the heat transfer limit at the evaporating boundary depends on the mechanism of liquid supply to and vapor escape from the liquid-vapor interface. The nucleation limit mainly depends on the maximum temperature at the upper left-hand corner of the wick structure and the pressure drop over the structure for the capillary limit consideration. Figure 3.11 shows the relationship between the pore radius and the minimum

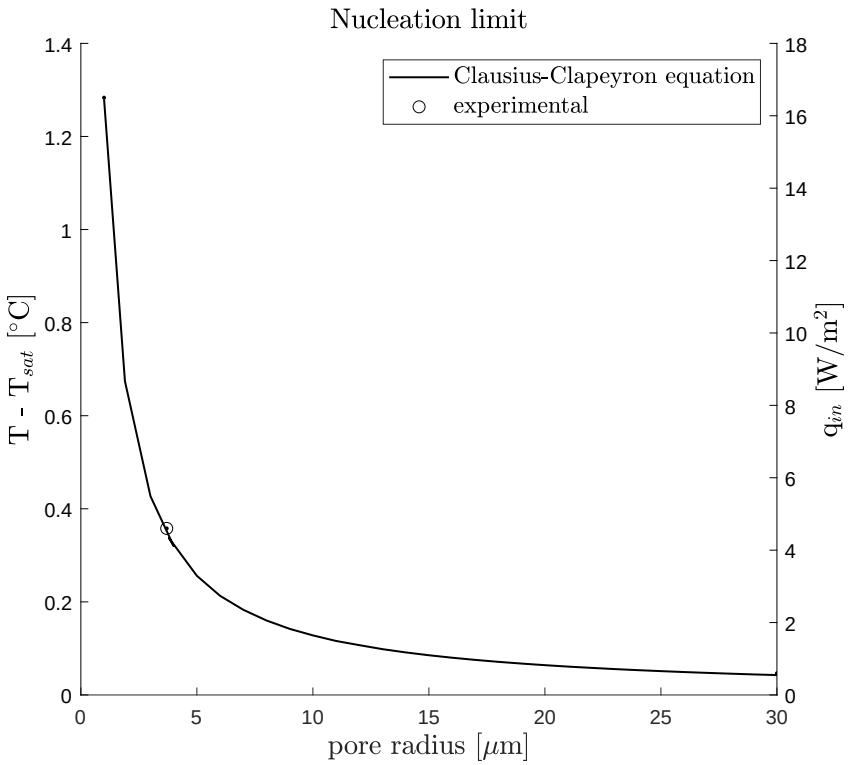

Figure 3.11: Nucleation limit as function of the pore radius.

superheat for the onset of bubble formation. The superheat required for nucleation is inversely proportional to the pore radius. Decreasing the pore size from 3.8 μm to 1 μm leads to an increase of the maximum heat flux from 5 to 16.5 W/cm^2. On the other hand, reducing the pore size affects the permeability of the porous structure increasing the capillary pressure as 1/r$_p$. A compromise is generally required between pore size distribution and permeability. Experimental tests on the evaporator show that the measured dry-out occurs at around 5 W/cm^2. This suggests that a pore radius distribution of around 3.8 μm is located in the region nearby the upper-left hand corner of the domain.

The performance of the evaporator is affected also by other parameters such as boundary conditions (liquid inlet temperature, convective heat transfer), geometric configurations (wick base and wick pillar size, vapor groove shape), wick and fluid properties.

Table 3.1: Thermal properties of ammonia NH_3 at 10.34 bar [37].

Properties	**Units**	**Ammonia NH_3**
Boiling point	°C	26
Density	kg/m^3	601.45
Viscosity	$Pa-s$	0.00012604
Specific heat	$J/kg-K$	4788.8
Heat of vaporization at boiling point	J/kg	1161.6
Surface tension	N/m	0.02028
Thermal conductivity	$W/m-K$	0.468
Molar mass	g/mol	17.03

Table 3.2: Boundary conditions, wick properties and geometrical inputs to the numerical model.

Parameter	**Units**	**Value**
Liquid temperature	°C	24
Liquid pressure	bara	10.34
Convective heat transfer coefficient	W/m^2-K	1900
Vapor pressure	bara	10.34
Saturation temperature	°C	26
Evaporative heat transfer coefficient	W/m^2-K	3.98 x 10^6
Effective thermal conductivity	$W/m-K$	56
Porosity	%	22.3
Permeability	m^2	3.2 x 10^{-13}
Effective pore radius	μm	3.8
L_x	mm	1
L_y	mm	4
L_{xp}	mm	0.5
L_{yp}	mm	1

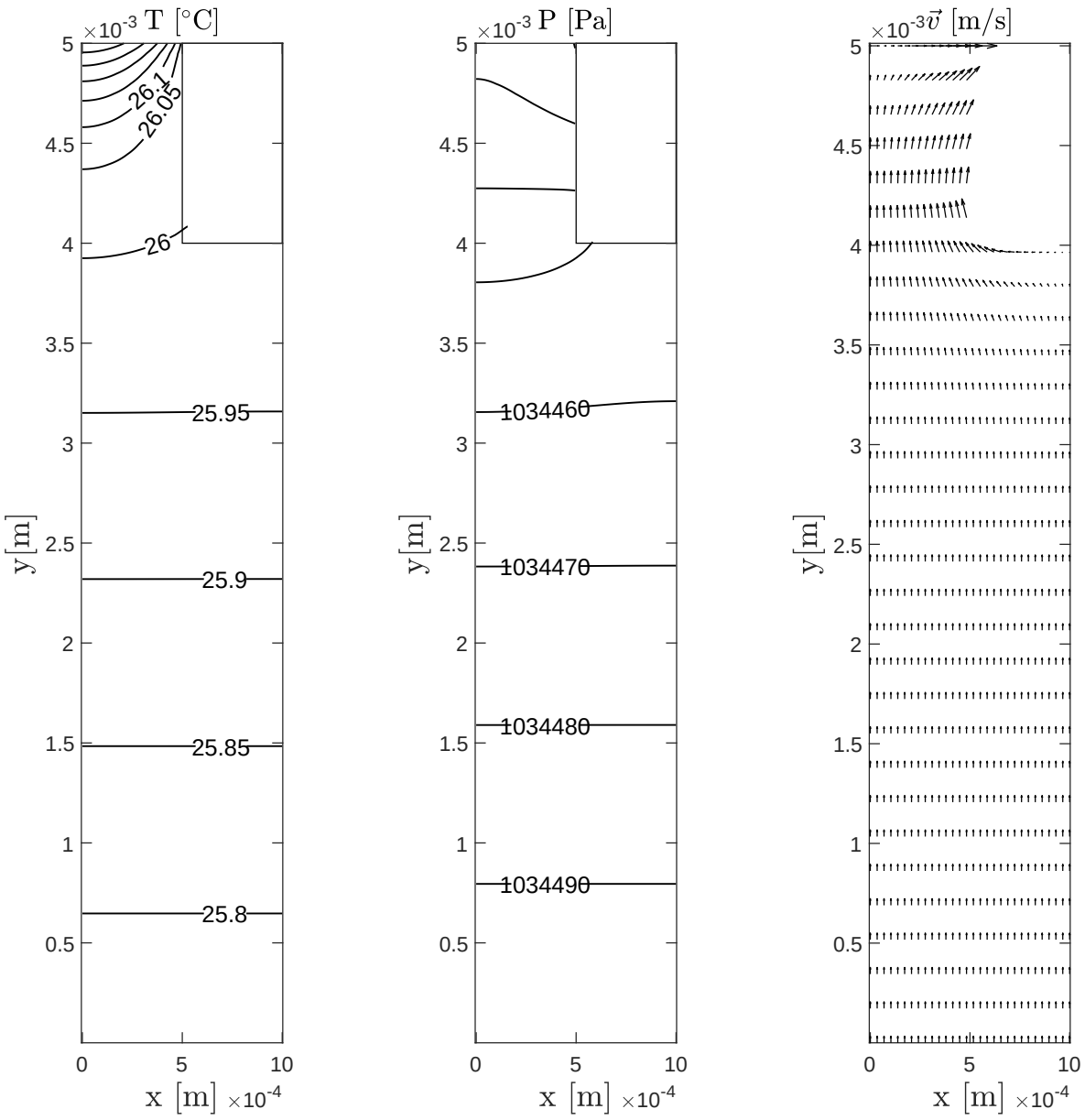

Figure 3.12: Temperature, pressure and velocity mapping along the porous domain with input heat flux $q_{in} = 5$ W/cm^2.

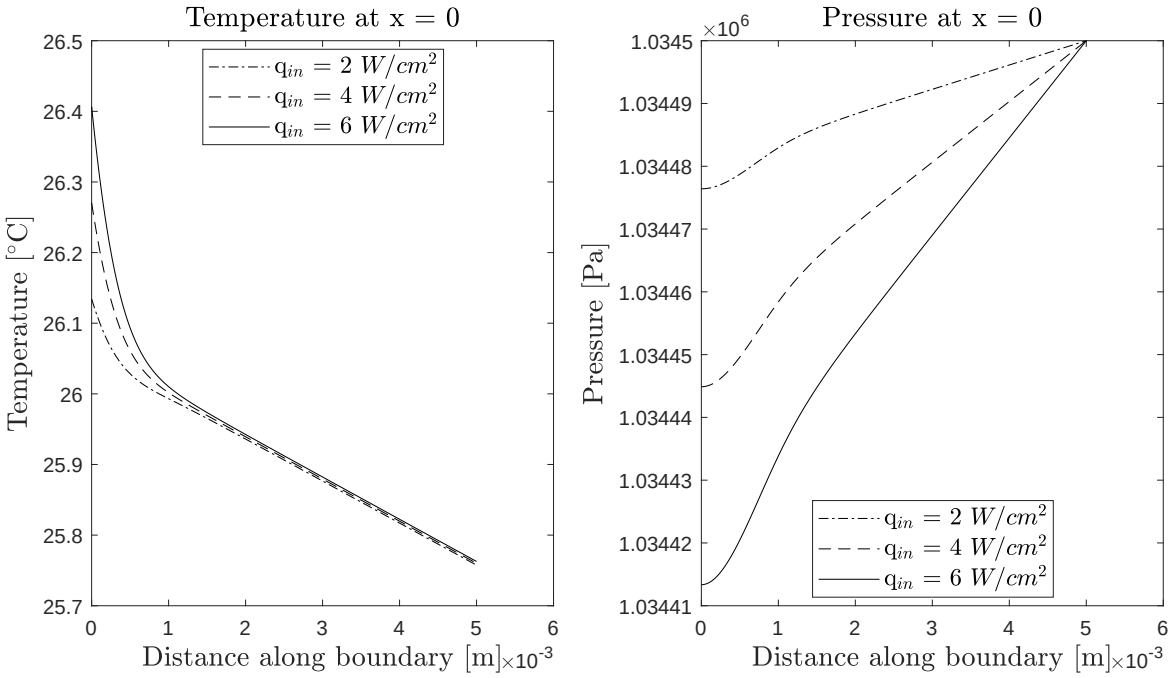

Figure 3.13: Temperature and pressure profiles along the y-axis for different q_{in}.

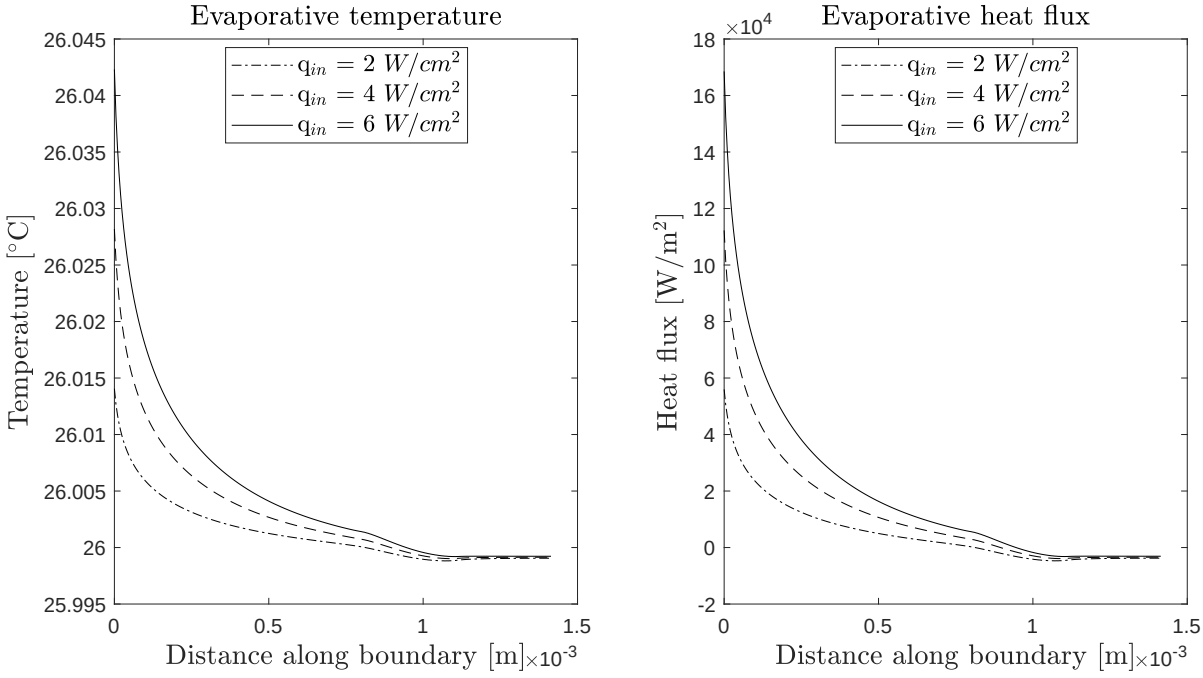

Figure 3.14: Temperature and heat flux profiles along $\partial\Omega_{ev}$ for different q_{in}.

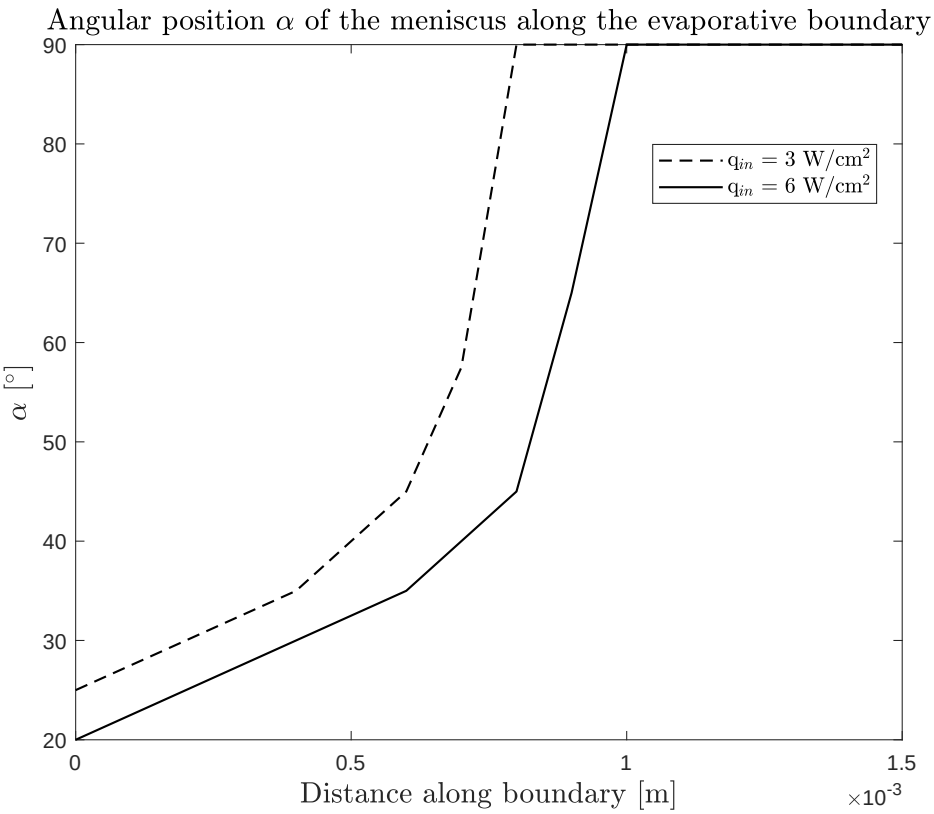

Figure 3.15: Angular position α of the meniscus along the evaporative boundary for different q_{in}.

3.6 Parametric study

In this section a detailed discussion on the effects of boundary conditions, porous and liquid properties and geometrical parameters is presented. The main benefit of the numerical model is not only to understand the heat and mass transfer of the evaporator used at JPL but also to provide a numerical tool for the correct design of future evaporators.

Each parameter has been varied while keeping all the others constant at the reference condition, as summarized in Table 3.2.

3.6.1 Boundary conditions

3.6.1.1 Effect of inlet temperature

Figure 3.16 and Figure 3.17 illustrate the effect of the inlet temperature on the performance of the elementary cell of the porous structure. In particular Figure 3.16 shows the temperature and pressure profiles along the axis of symmetry (y-axis). It is possible to notice that lower values of inlet temperature lead to lower values of the temperature at the bottom of the wick but do not affect the maximum temperature at the left-hand side of the wick.

Table 3.3 shows that at same input heat flux (5 W/cm^2), having a higher inlet temperature allows to reduce the heat losses to the liquid chamber. Moreover, if the temperature at the inlet is highly subcooled (5 °C for instance) the applied heat load might not be able to create a favorable pressure gradient that encourages the liquid to flow from the bottom to the top section of the wick.

Figure 3.17 shows that a highly subcooled liquid temperature affects the evaporative temperature and heat flux profiles in particular at the horizontal section of the porous structure where condensation might take place, instead of evaporation, reducing the overall evaporative heat load.

Table 3.3: Effect of the boundary conditions on the performance of the elementary cell of the evaporator.

Parameter	**Units**	**Value**	$\mathbf{T}_{max}$ [°C]	Δ**P** [Pa]	$\mathbf{Q}_{in}$ [W/m]	$\mathbf{Q}_{ev}$ [W/m]	$\mathbf{Q}_{conv}$ [W/m]
q_{in}	W/cm^2	2	26.13	27.50	9.99	-6.65	-3.34
		4	26.27	63.00	19.98	-16.64	-3.34
		6	26.41	98.50	29.97	-26.62	-3.35
T_l	[°C]	5	26.32	34.89	24.98	9.93	-35.03
		15	26.33	44.71	24.98	-6.61	-18.35
		25	26.34	84.78	24.98	-23.30	-1.68
h_{conv}	W/m^2K	500	26.34	86.50	24.98	-24.02	-0.97
		1500	26.34	82.28	24.98	-22.26	-2.71
		3000	26.34	76.93	24.98	-20.03	-4.93
$\hat{a}$	-	0.1	26.34	80.75	24.98	-21.63	-3.35
		0.5	26.33	81.56	24.98	-21.63	-3.35
		1	26.33	81.66	24.98	-21.62	-3.36

3.6.1.2 Effect of convective heat transfer

The convective heat transfer for the JPL evaporator under the nominal working condition has been estimated as 1900 W/m^2-K as indicated by equation 3.10. Figure 3.18 and Figure 3.19 both show the effect of different convective heat transfer coefficients. Higher is h_{conv}, lower is the temperature at the wick base without affecting the overall maximum temperature, and higher is the heat loss to the liquid chamber (see Table 3.3) at same heat input.

3.6.1.3 Effect of the accommodation coefficient

The accommodation coefficient has been defined in equation 3.14 and affects the evaporative heat transfer coefficient. As shown in Figure 3.20, Figure 3.21 and Table 3.3 it does not affect the temperature and pressure drop along the porous structure, but influences the evaporative temperature along the evaporative boundary. However the overall evaporative heat load does not change since lower $\hat{a}$ leads to higher evaporative temperature, but also lower h_{ev}.

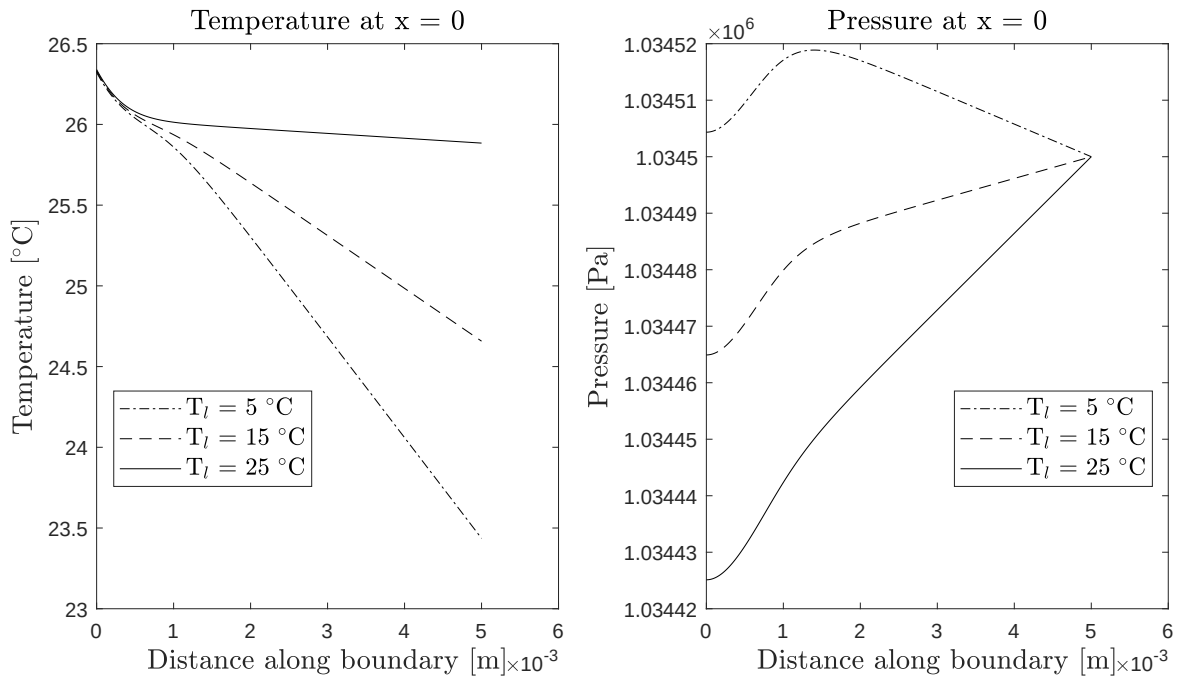

Figure 3.16: Temperature and pressure profiles along the y-axis for different T_l.

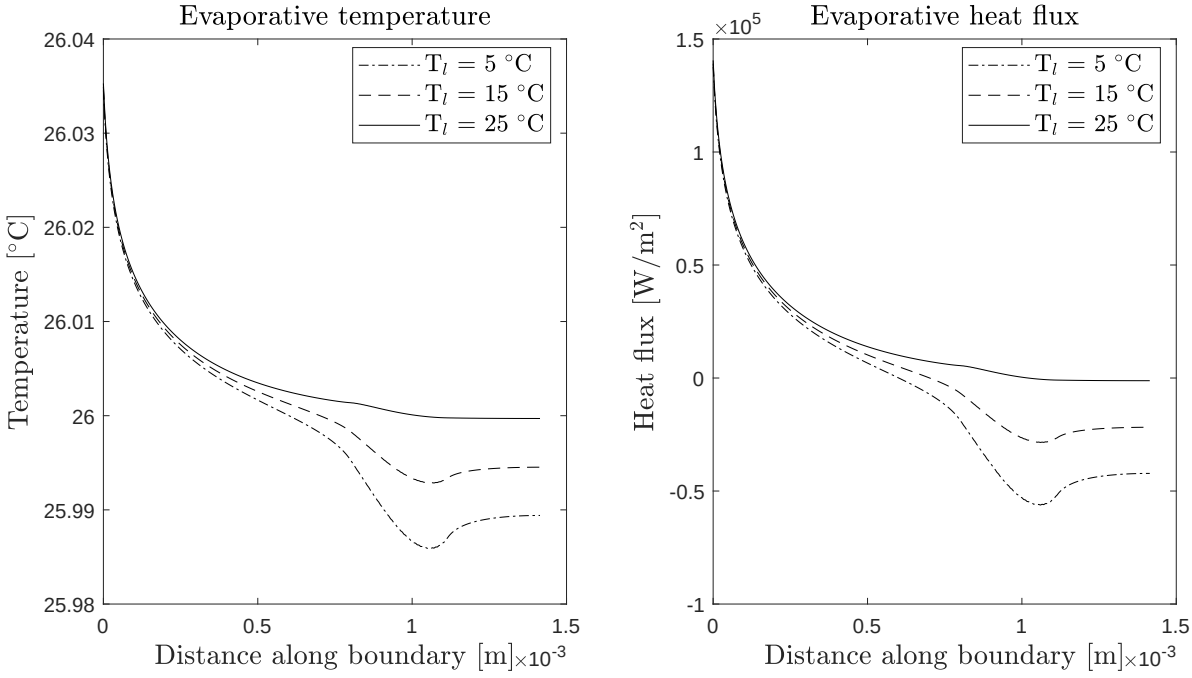

Figure 3.17: Temperature and heat flux profiles along $\partial\Omega_{ev}$ for different T_l.

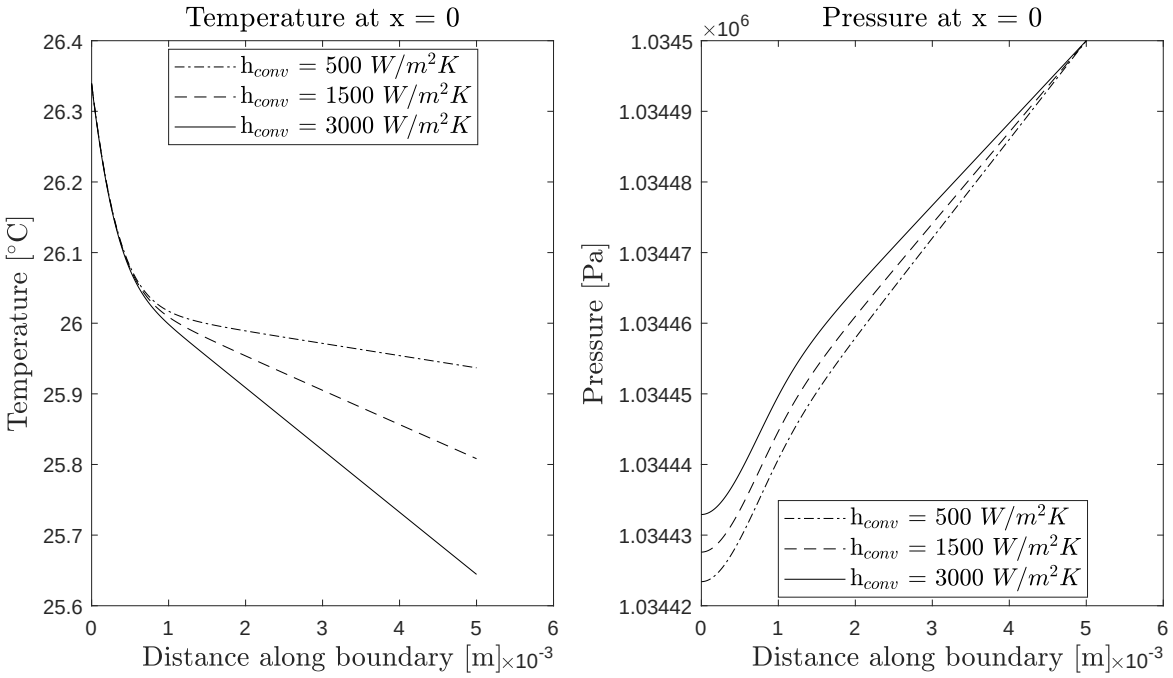

Figure 3.18: Temperature and pressure profiles along the y-axis for different h_{conv}.

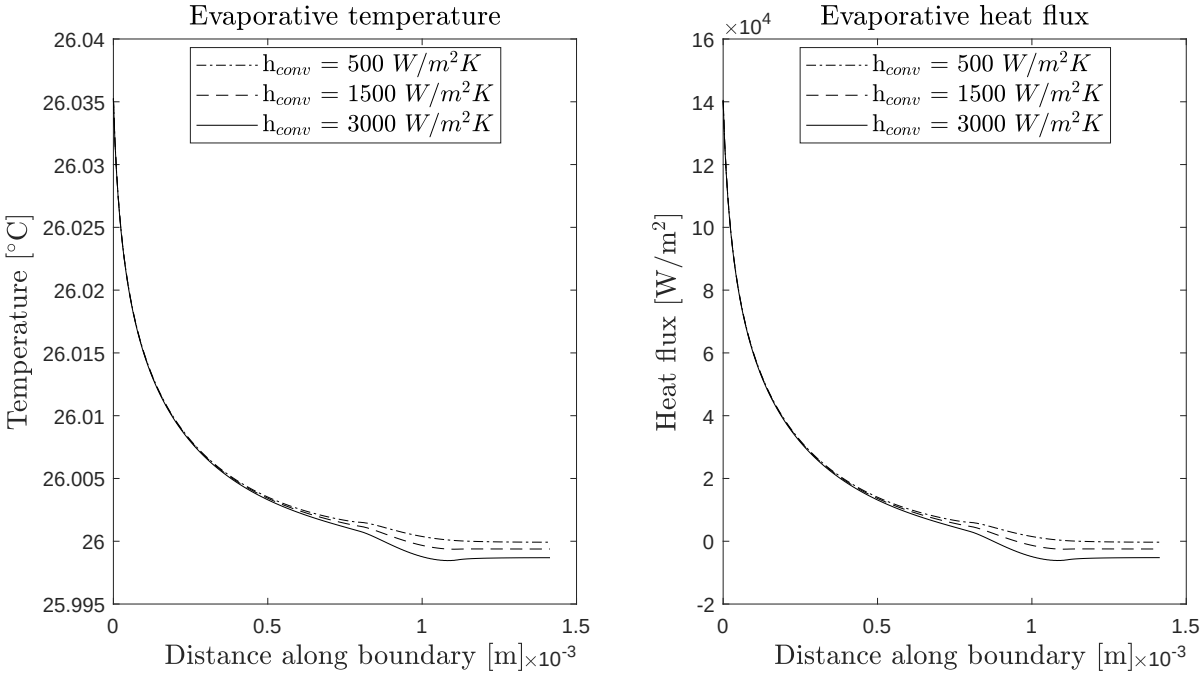

Figure 3.19: Temperature and heat flux profiles along $\partial\Omega_{ev}$ for different h_{conv}.

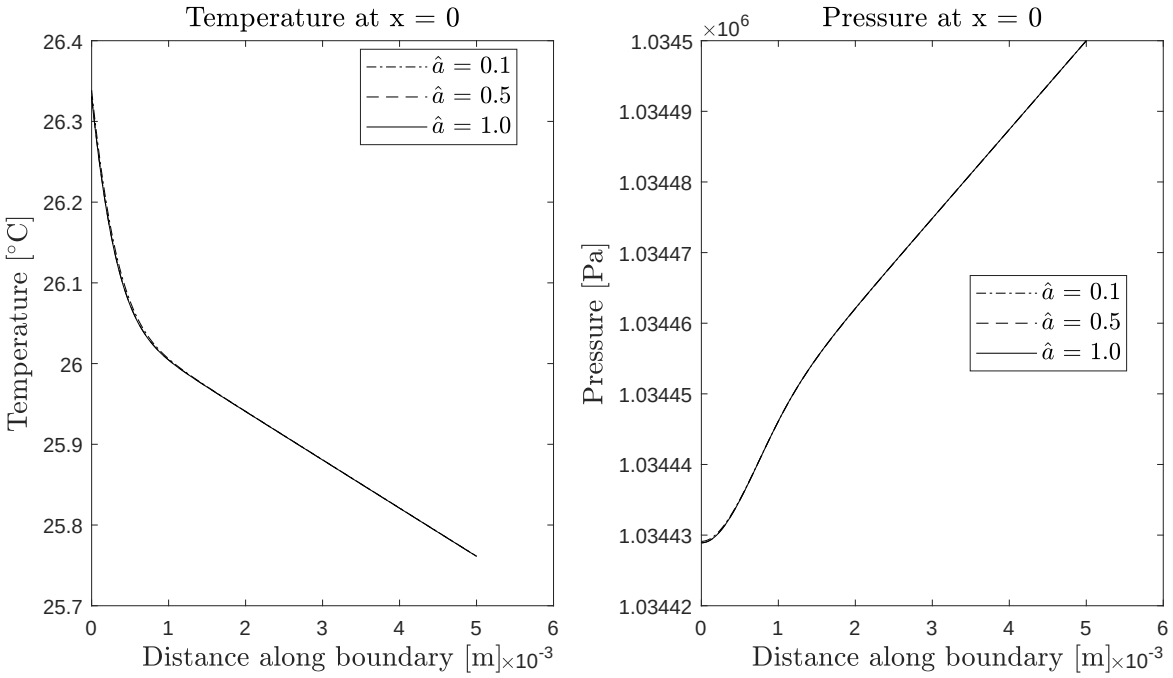

Figure 3.20: Temperature and pressure profiles along the y-axis for different $\hat{a}$.

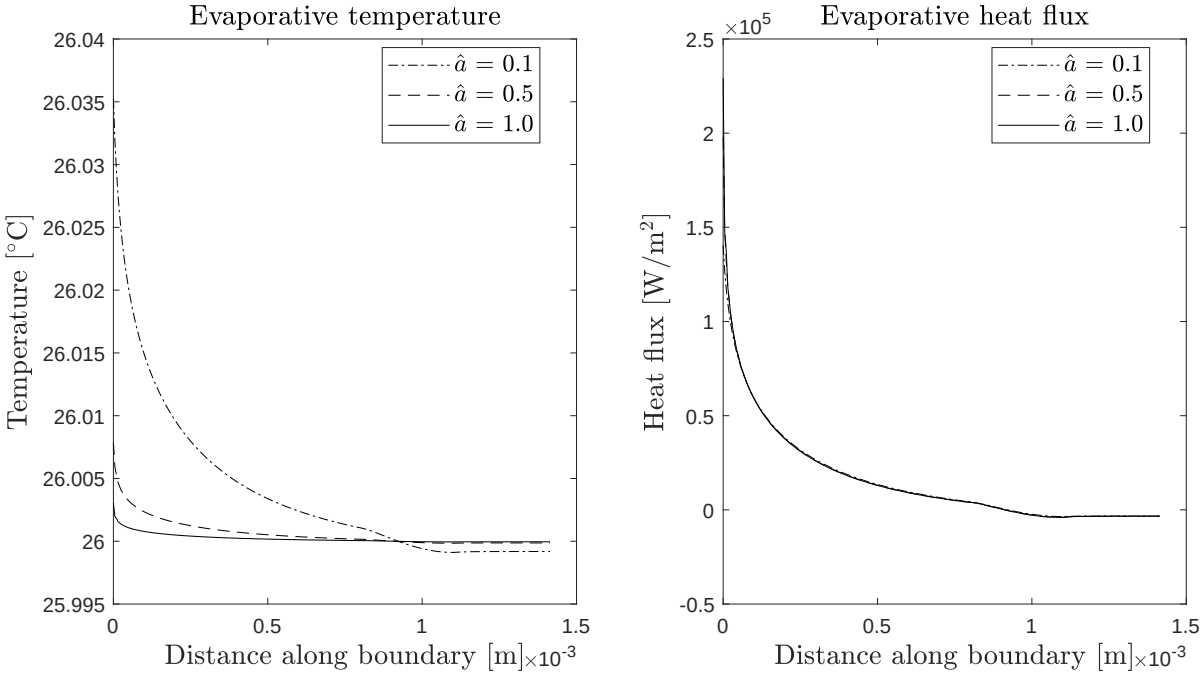

Figure 3.21: Temperature and heat flux profiles along $\partial\Omega_{ev}$ for different $\hat{a}$.

3.6.2 Material and liquid properties

3.6.2.1 Effect of wick effective thermal conductivity

The wick properties have a great influence on the heat transfer performance. An increase in the effective thermal conductivity reduces the temperature gradient across the medium. In Figure 3.22 and Figure 3.23 a comparison between aluminum and stainless steel (both compatible with ammonia) is presented. At $q_{in} = 5$ W/cm^2, the maximum temperature is 26.3 and 28.6 °C respectively for aluminum and stainless steel.

Higher k_e leads to a higher heat loss towards the liquid chamber as summarized in Table 3.4, but on the other side aluminum can accommodate higher input heat fluxes for the same nucleation limit. A designer could consider the possibility to use porous structures with a low thermal conductivity layer located at the interface with the liquid chamber to reduce the heat losses.

3.6.2.2 Effect of permeability

Figure 3.24 and Figure 3.25 present the effect of permeability on the temperature and pressure fields for K varying from 10^{-12} to 10^{-14} m^2. The permeability considerably affects the pressure drop along the domain. As expected, higher the permeability, lower is the pressure drop in the wick structure. The wick capillary pressure decreases with increase of permeability that is not desirable when the driving force is the capillary pressure. On the other hand, the temperature profile along the evaporative boundary is not considerably different, as presented in Figure 3.25, indicating that the evaporative heat load is not affected by this parameter as also summarized in Table 3.4.

3.6.2.3 Effect of porosity

Figure 3.26 and Figure 3.27 show the effect of the porosity ϵ on the temperature and pressure profiles along the wick domain. While it is possible to notice that the evaporative and convective heat loads are not significantly affected by this parameter (see Table 3.4), the

Table 3.4: Effect of the wick and fluid properties on the performance of the elementary cell of the evaporator.

Parameter	**Units**	**Value**	$\mathbf{T}_{max}$ [°C]	$\mathbf{\Delta P}$ [Pa]	$\mathbf{Q}_{in}$ [W/m]	$\mathbf{Q}_{ev}$ [W/m]	$\mathbf{Q}_{conv}$ [W/m]
k_e	W/m-K	6	28.59	85.03	24.92	-23.05	-1.84
		56	26.34	80.75	24.98	-21.63	-3.35
K	m^2	3.2 E-12	26.34	7.87	24.98	-21.63	-3.35
		3.2 E-13	26.34	80.75	24.98	-21.63	-3.35
		3.2 E-14	26.34	787.06	24.98	-21.63	-3.35
ϵ	%	10	26.28	1196.14	24.98	-21.56	-3.42
		20	26.33	118.56	24.98	-21.61	-3.36
		30	26.39	27.00	24.97	-21.68	-3.29
fluid	-	ammonia	26.34	80.75	24.98	-21.63	-3.35
		acetone	26.42	103.76	24.99	-21.69	-3.29

pressure profile along the domain is highly influenced by the relationship between porosity and permeability as indicated in equation 2.2.

3.6.2.4 Effect of working fluid

The choice of the working fluid is crucial on the performance of the evaporator. It depends on many criteria as already indicated in Chapter 1 and Chapter 2. Assuming an aluminum porous structure, ammonia and acetone have been compared since both are compatible with the wick material. Figure 3.28 and Figure 3.29 illustrate the comparison between these two fluids. It is possible to observe that the use of ammonia is more advantageous in terms of better performance of the evaporator. Ammonia allows a lower maximum temperature (consequently higher input heat fluxes for same nucleation limit), a lower pressure drop and a negligible difference on the evaporative and convective heat loads (see Table 3.4) even if acetone shows an higher temperature profile along the evaporative boundary.

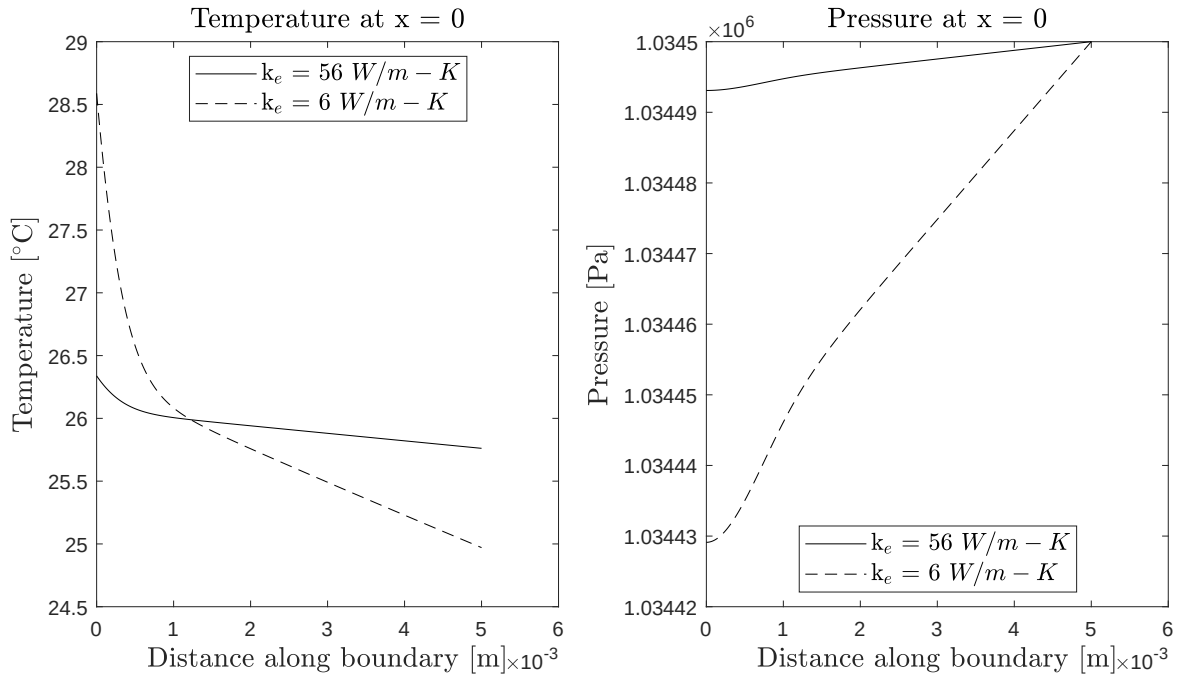

Figure 3.22: Temperature and pressure profiles along the y-axis for different k_e.

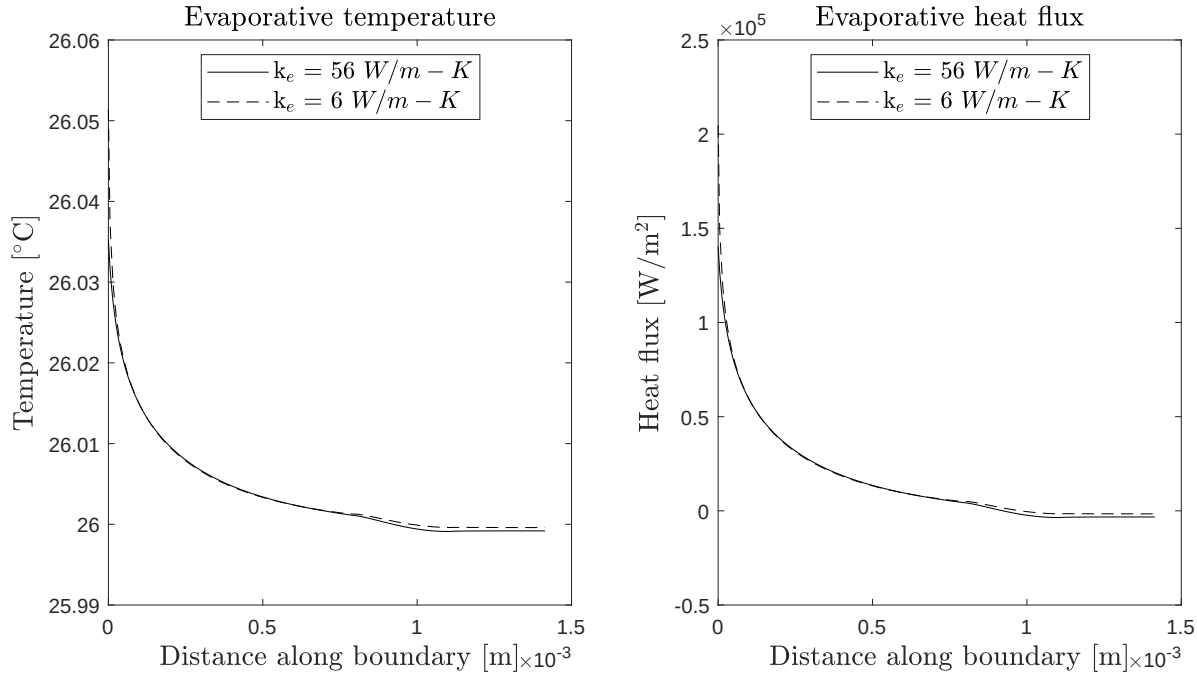

Figure 3.23: Temperature and heat flux profiles along $\partial\Omega_{ev}$ for different k_e.

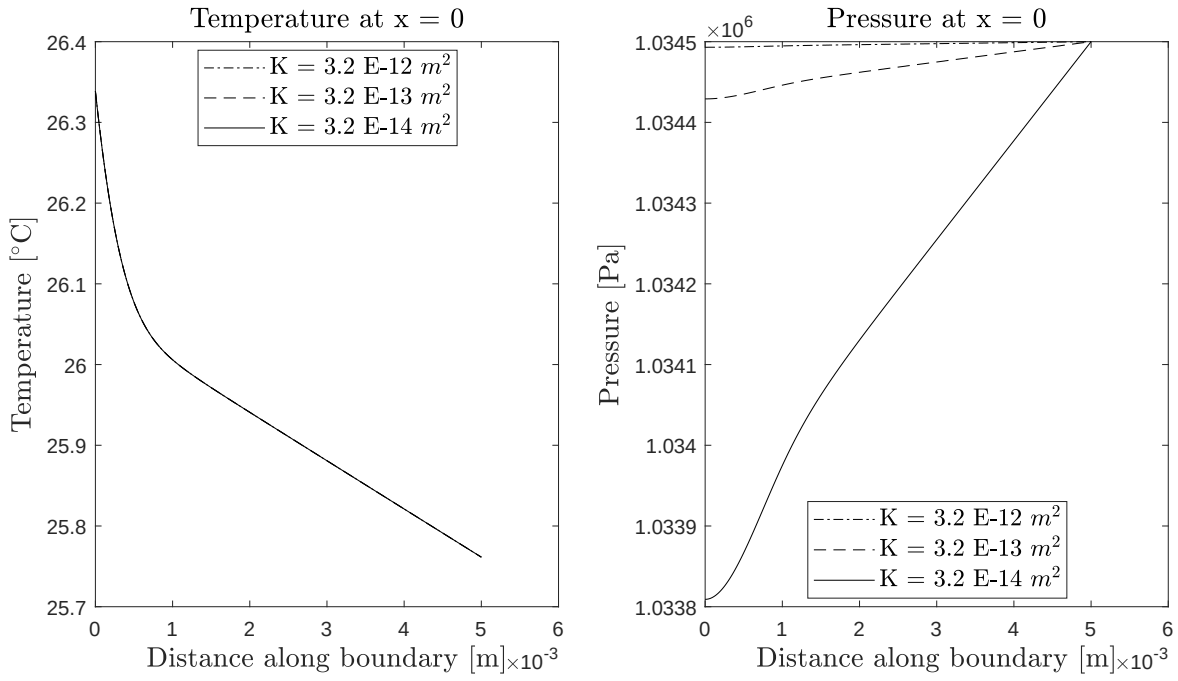

Figure 3.24: Temperature and pressure profiles along the y-axis for different K.

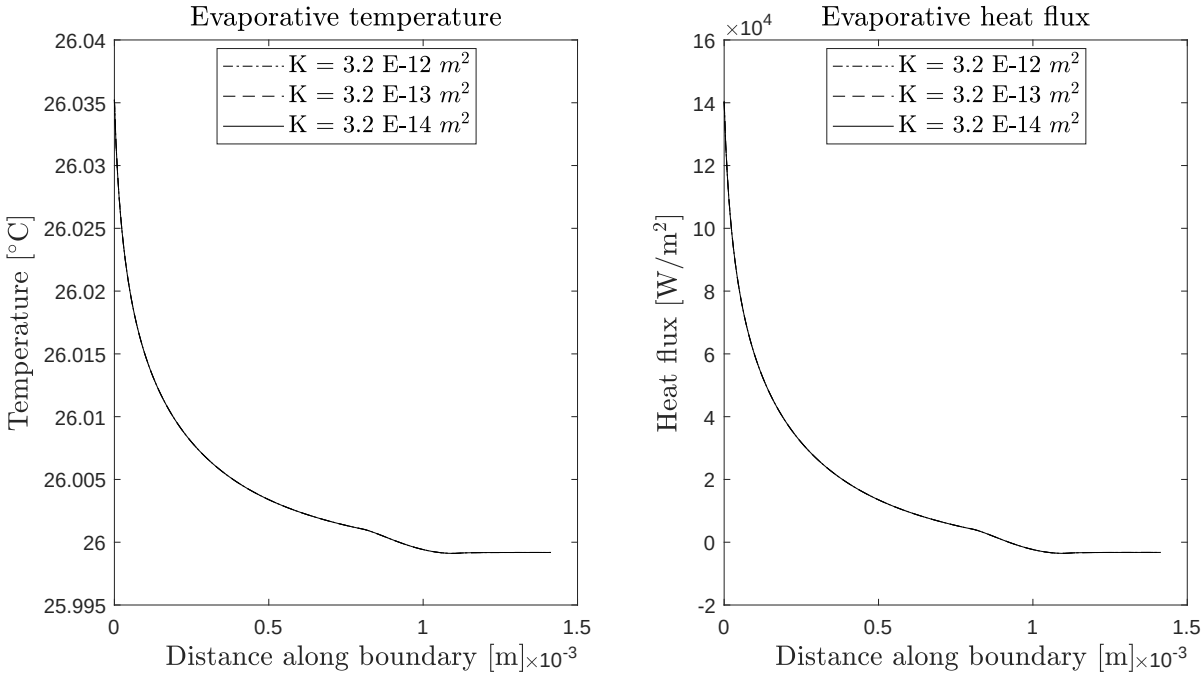

Figure 3.25: Temperature and heat flux profiles along $\partial\Omega_{ev}$ for different K.

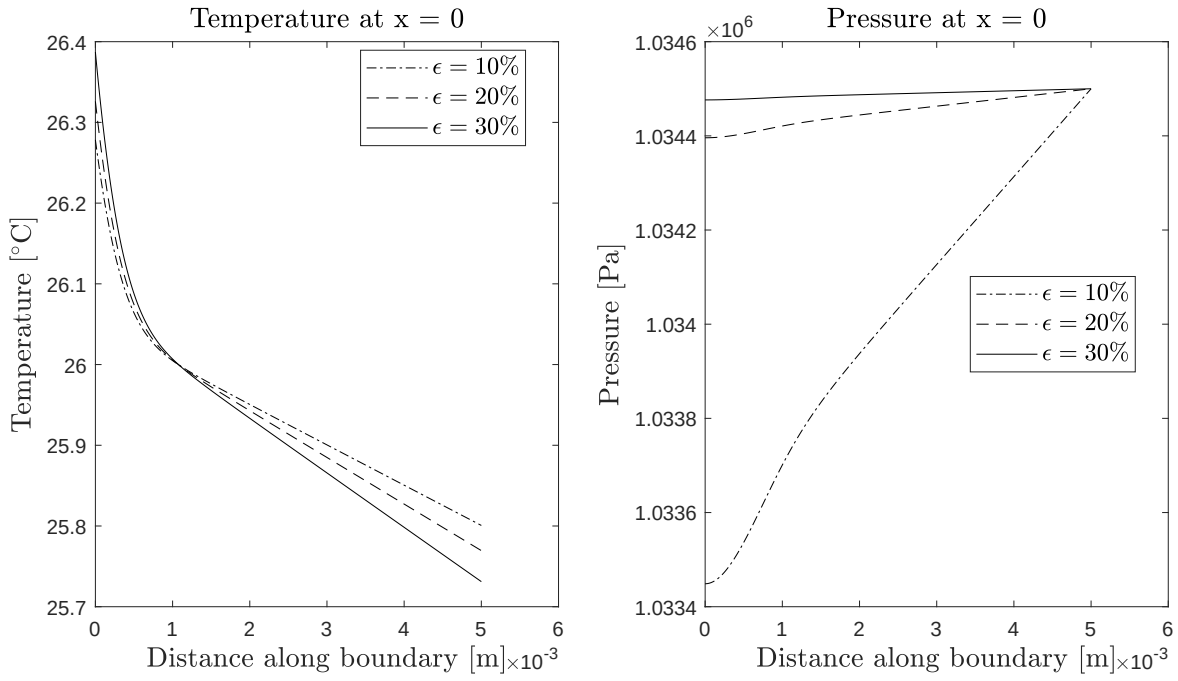

Figure 3.26: Temperature and pressure profiles along the y-axis for different ϵ.

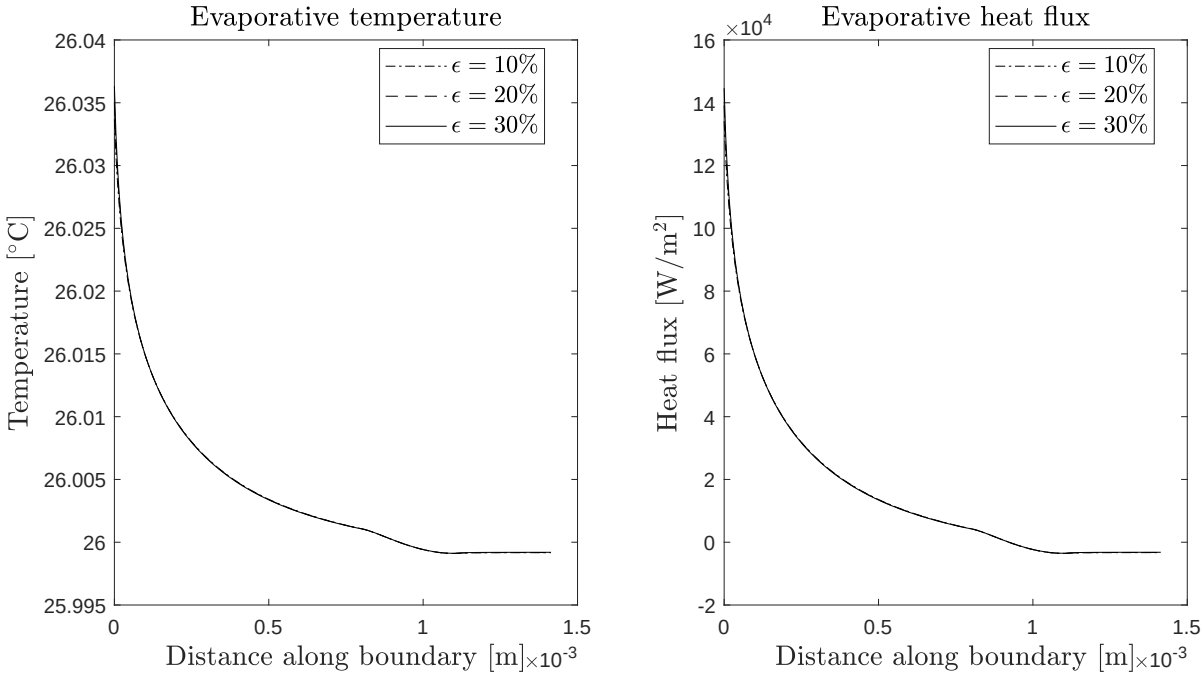

Figure 3.27: Temperature and heat flux profiles along $\partial\Omega_{ev}$ for different ϵ.

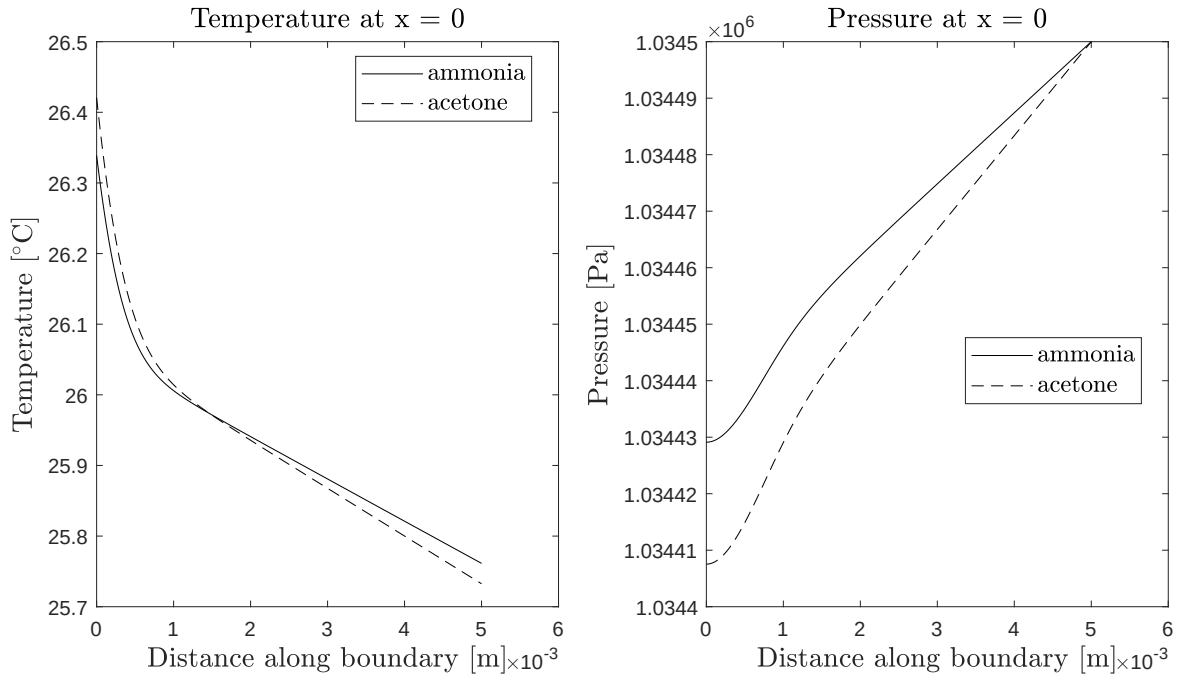

Figure 3.28: Temperature and pressure profiles along the y-axis for different fluids.

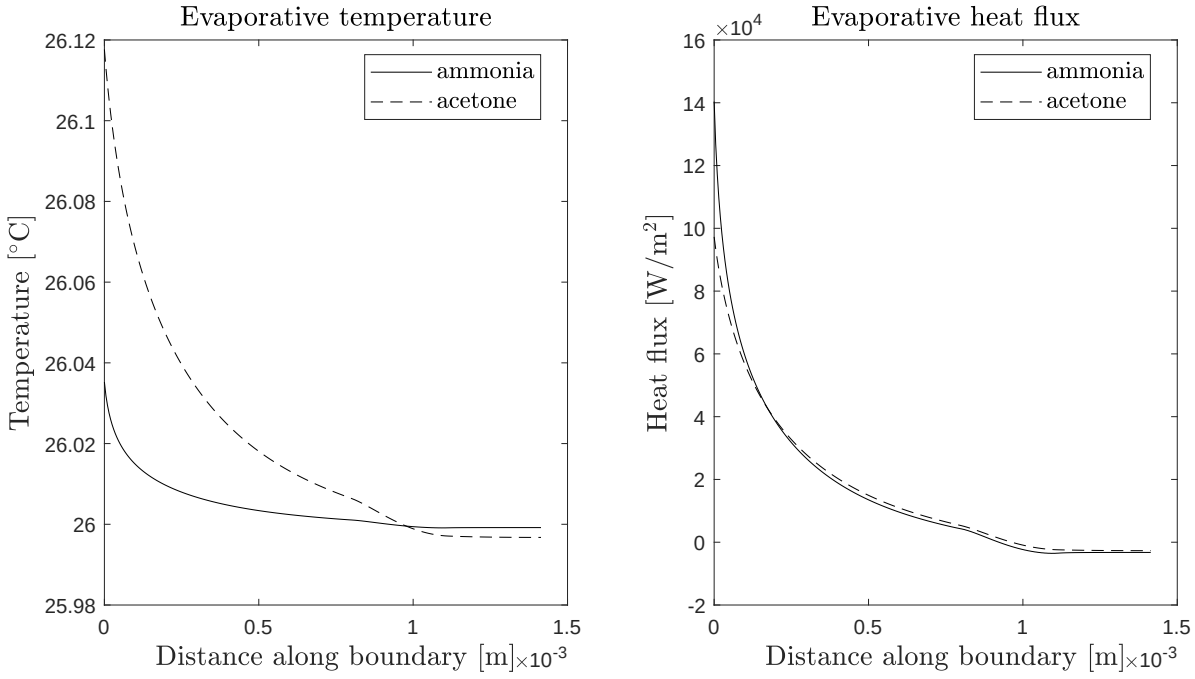

Figure 3.29: Temperature and heat flux profiles along $\partial\Omega_{ev}$ for different fluids.

3.6.3 Geometry

3.6.3.1 Effect of porous base thickness

The wick height affects the performance of the elementary cells of the evaporator. Figure 3.30, Figure 3.31 and Table 3.5 indicate this influence. It is possible to notice that longer is the path for the liquid flow and the separation from the liquid chamber, higher is the temperature gradient between the wick domain and lower is the convective heat loss to the liquid chamber. The maximum temperature in the wick is not affected by this parameter, and the temperature profiles along the evaporative boundary are very similar. However, important is the effect on the pressure drop along the domain: higher L_y leads to higher pressure drop.

3.6.3.2 Effect of porous pillar height

A study on the efficacy of the wick pillar has been performed and it both affects the temperature and pressure fields. Figure 3.32, Figure 3.33 and Table 3.5 prove this influence. Higher is the wick pillar height L_{yp}, larger is the temperature gradient along the wick, and consequently lower is the convective heat loss to the liquid chamber. However, longer wick pillars bring large pressure drops along the domain. The configuration with wick pillar is preferable compared to a configuration with just a solid pillar since it has a lower risk of incipience boiling for higher heat fluxes and similar evaporative heat flux along the liquid-vapor interface at the wick boundary.

3.6.3.3 Effect of porous pillar width

The wick pillar width L_{xp} has a significant influence on the thermal performance of the evaporator. As shown in Table 3.5, smaller is L_{xp} lower is the maximum temperature within the wick. This allows higher heat fluxes for same nucleation limit. Figure 3.34 and Table 3.5 illustrate that a smaller wick pillar width allows a lower pressure drop in the porous medium. However, at same input heat flux, the evaporative temperature and heat flux profiles seem

to be in favor of larger L_{xp}. This effect is due to the fact the same heat flux is applied over a larger length increasing the temperature and the evaporative heat loads in the wick as shown in Figure 3.35. On the other side when applying the same input heat load over the same length, the most performing solution is the one where more wick pillars with smaller L_{xp} and L_x are occupying the same area (higher elementary cell density). This configuration allows a better heat transfer from the heat input boundary to the evaporative boundary.

3.6.3.4 Effect of vapor chamber shape

Three shapes of the vapor grooves have been studied: the wick pillar, the rectangular and the round grooves. Figure 3.36 shows a comparison of the temperature mapping between these three configurations under same input heat flux. It is possible to observe that the wick pillar configuration present a lower maximum temperature compared to the other two options, as shown in Figure 3.37 and in Table 3.5. Moreover the pillar configuration has also better performances in terms of pressure drop along the wick. Both the rectangular and the round shapes have more than two times the pressure drop of the wick pillar. The overall evaporative heat loads are very similar between the configurations in terms of percentage of the total heat input.

3.6.3.5 Effect of casing thickness

Figure 3.39 shows the configuration of the porous wick and a solid layer on top of it that represent the casing of the evaporator. The highest gradient is present in the solid domain and Figure 3.40 plots the temperature profiles along the y-axis for different skin thicknesses. Thicker is the skin, higher is the maximum temperature on the solid domain. However, this does not affect the maximum temperature within the wick, as summarized in Table 3.5. The evaporative heat transfer, as shown in Figure 3.41, is not affected by the change in the skin thickness.

Table 3.5: Effect of the geometric parameters on the performance of the elementary cell of the evaporator.

Parameter	**Units**	**Value**	$\mathbf{T}_{max}$ [°C]	$\mathbf{\Delta P}$ [Pa]	$\mathbf{Q}_{in}$ [W/m]	$\mathbf{Q}_{ev}$ [W/m]	$\mathbf{Q}_{conv}$ [W/m]
L_y	mm	1	26.34	42.80	24.98	-21.31	-3.68
		3	26.34	67.99	24.98	-21.53	-3.45
		6	26.34	106.55	24.98	-21.81	-3.16
L_{yp}	mm	0	26.49	52.6	24.98	-21.32	-3.68
		0.5	26.34	66.91	24.98	-21.58	-3.40
		1.5	26.34	95.11	24.98	-21.64	-3.34
L_{xp}	mm	0.2	26.14	46.30	9.98	-6.65	-3.34
		0.5	26.34	80.75	24.98	-21.63	-3.35
		0.7	26.47	103.13	34.98	-31.58	-3.39
shape	-	pillar	26.34	80.75	24.98	-21.63	-3.35
		rect.	26.61	186.90	50.00	-46.61	-3.34
		round	26.68	173.62	50.00	-46.60	-3.35
t_s	mm	0.5	26.34	80.90	50.00	-46.65	-3.35
		1	26.34	80.75	50.00	-46.55	-3.45
		2	26.34	80.40	50.00	-46.50	-3.50

3.6.3.6 Effect of structural struts

A 3D heat transfer model has been built in order to study the effect of the struts (see Figure 1.4) on the thermal performance of the evaporator. This model is based on the same equations and boundary conditions presented in Chapter 3 with the additional presence of a solid rod crossing the wick domain. Larger is the diameter of the strut, higher is the peak temperature reached at its center as shown in Figure 3.42 and Figure 3.43. For a 2 mm diameter strut, the peak temperature corresponds to 26.4 °C and the evaporative heat load is around 81% of the total heat input. The presence of the strut increases the heat loss towards the liquid chamber and consequently decreases the evaporative heat load that corresponds to around 86% for the case without any strut and with an applied heat flux of 5 W/cm^2. Large struts may occlude the vapor channels, downgrading the thermal performance. In the design of the evaporator the vapor grooves should not be occluded by any struts and vapor should smoothly flow to the outlet.

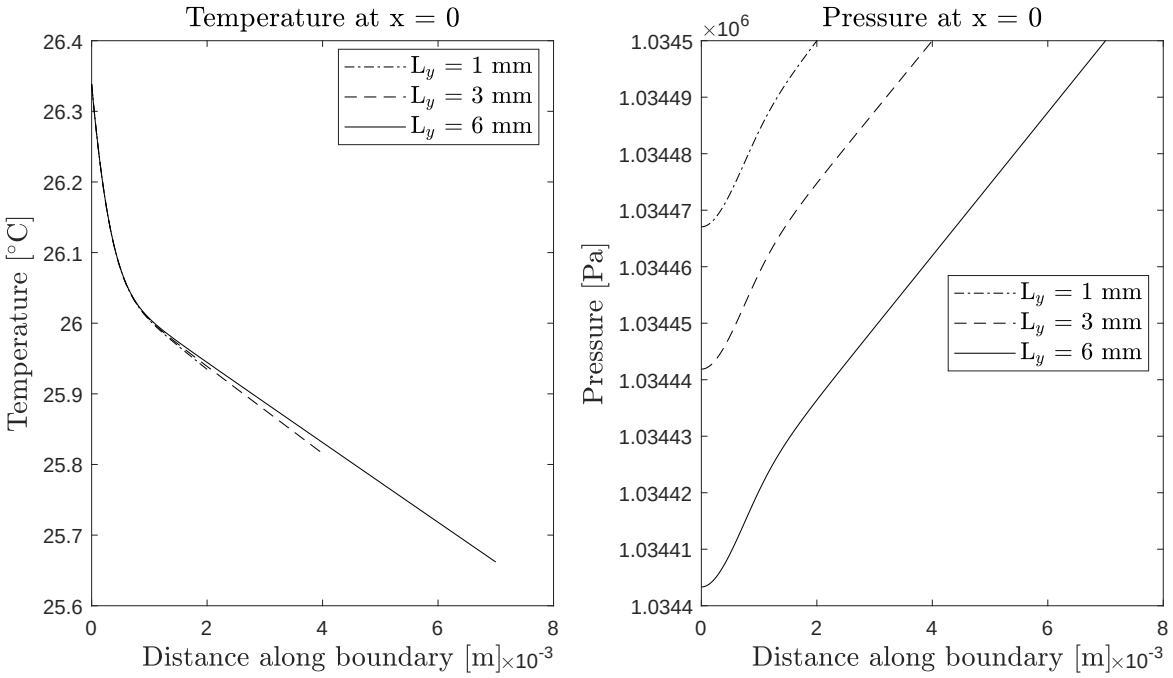

Figure 3.30: Temperature and pressure profiles along the y-axis for different L_y.

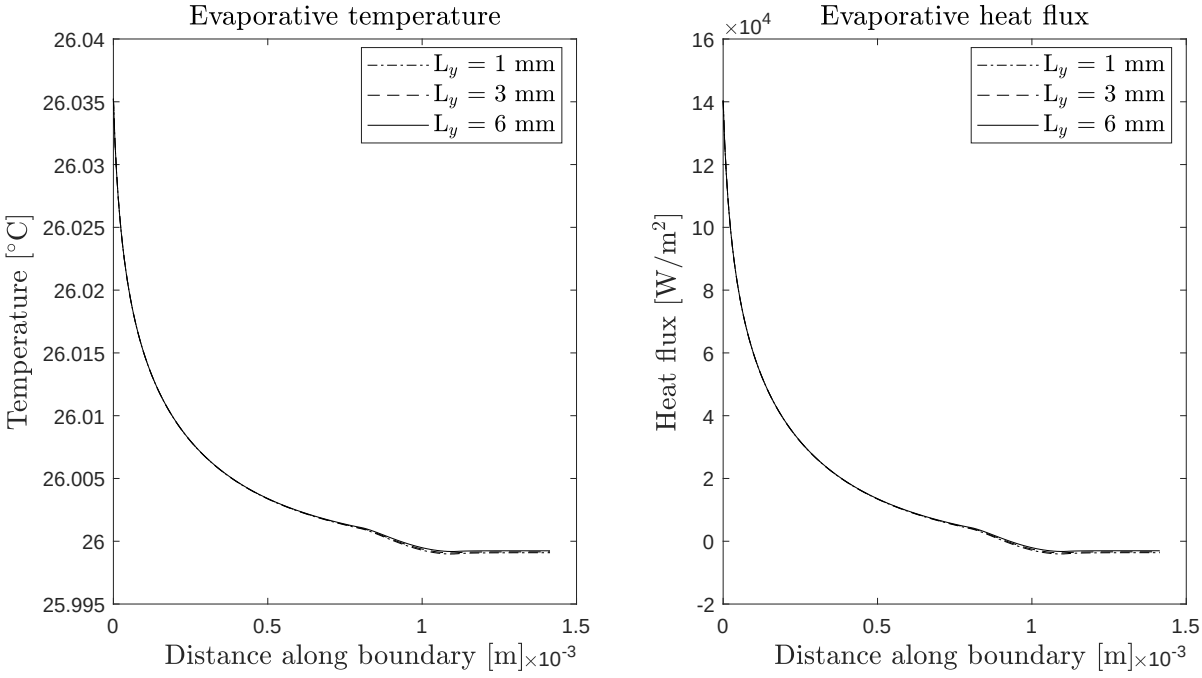

Figure 3.31: Temperature and heat flux profiles along $\partial\Omega_{ev}$ for different L_y.

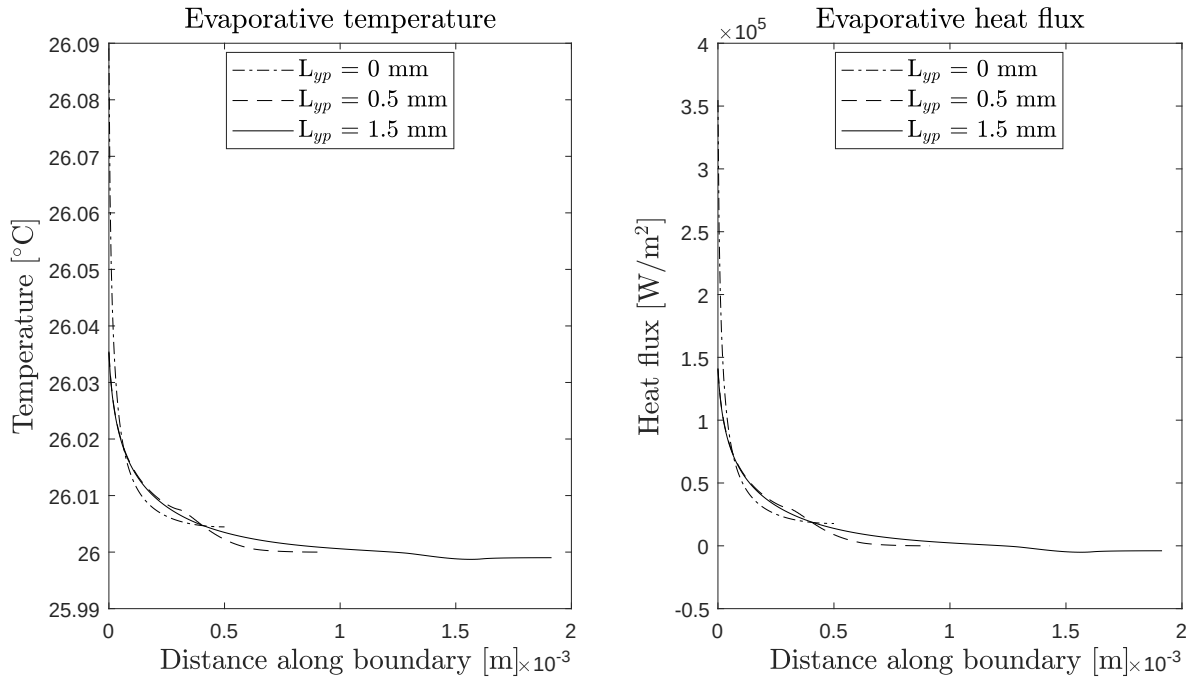

Figure 3.32: Temperature and pressure profiles along the y-axis for different L_{yp}.

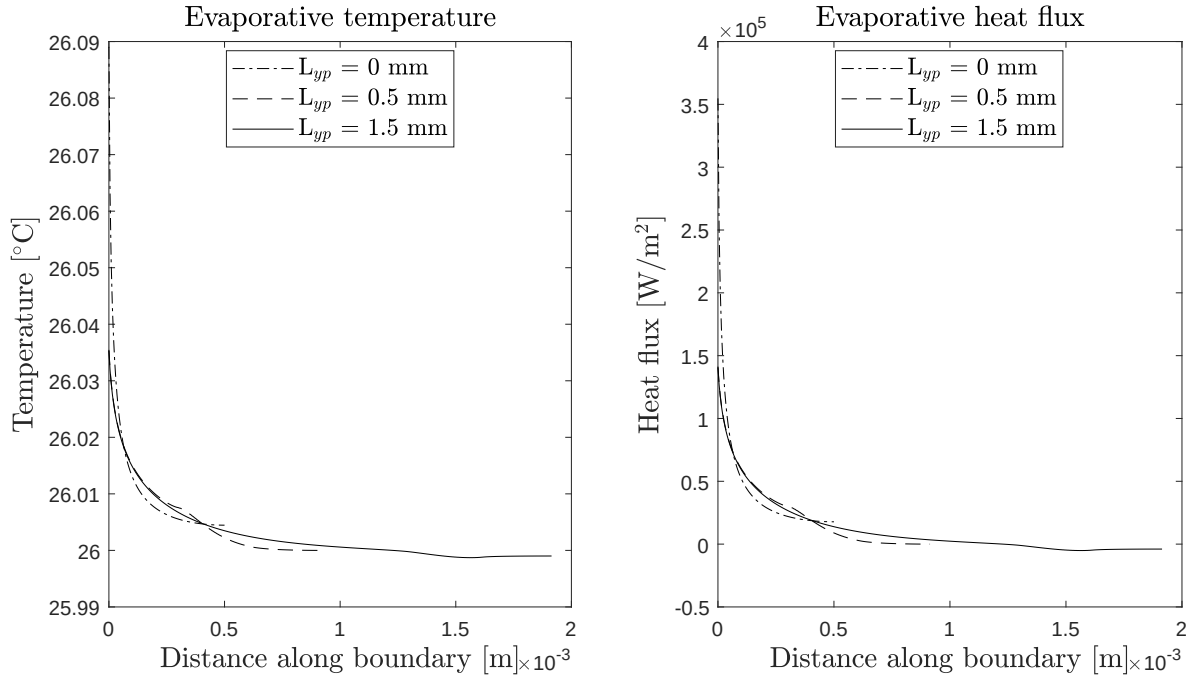

Figure 3.33: Temperature and heat flux profiles along $\partial\Omega_{ev}$ for different L_{yp}.

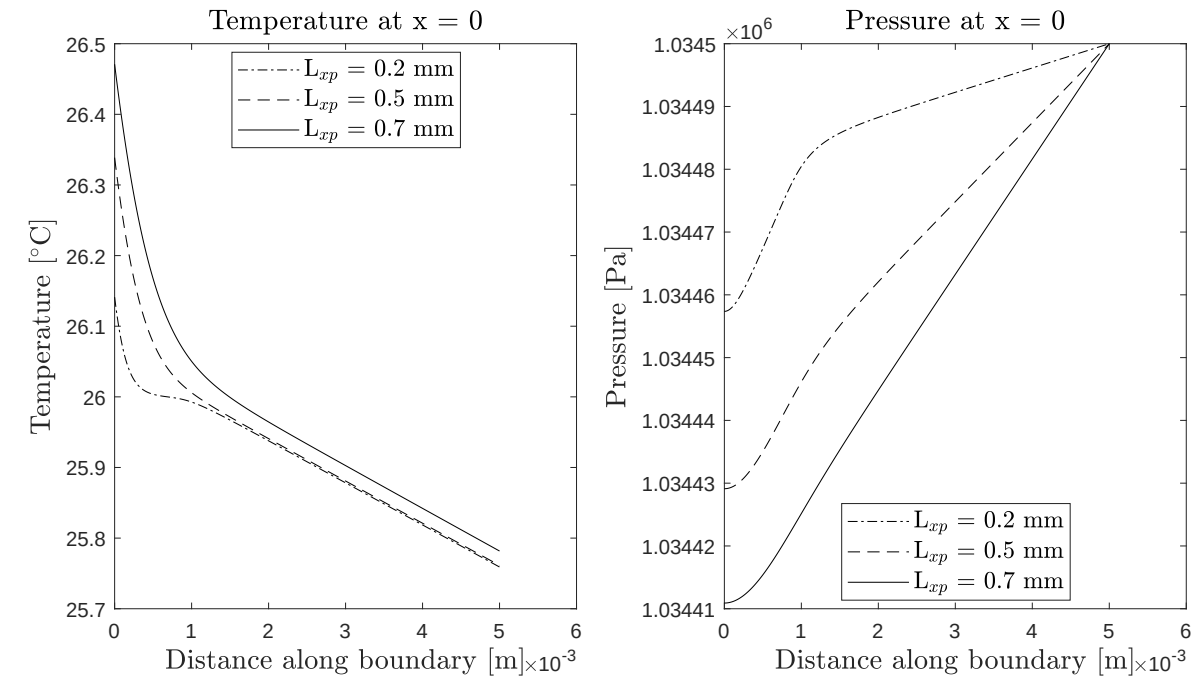

Figure 3.34: Temperature and pressure profiles along the y-axis for different L_{xp}.

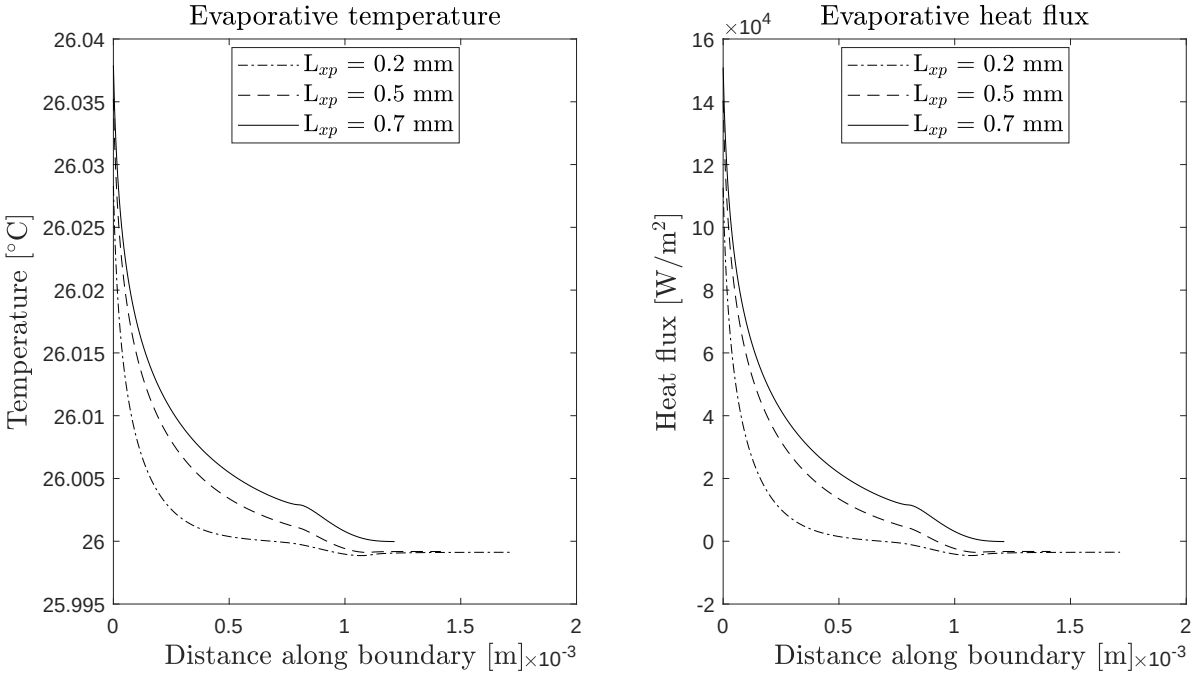

Figure 3.35: Temperature and heat flux profiles along $\partial\Omega_{ev}$ for different L_{xp}.

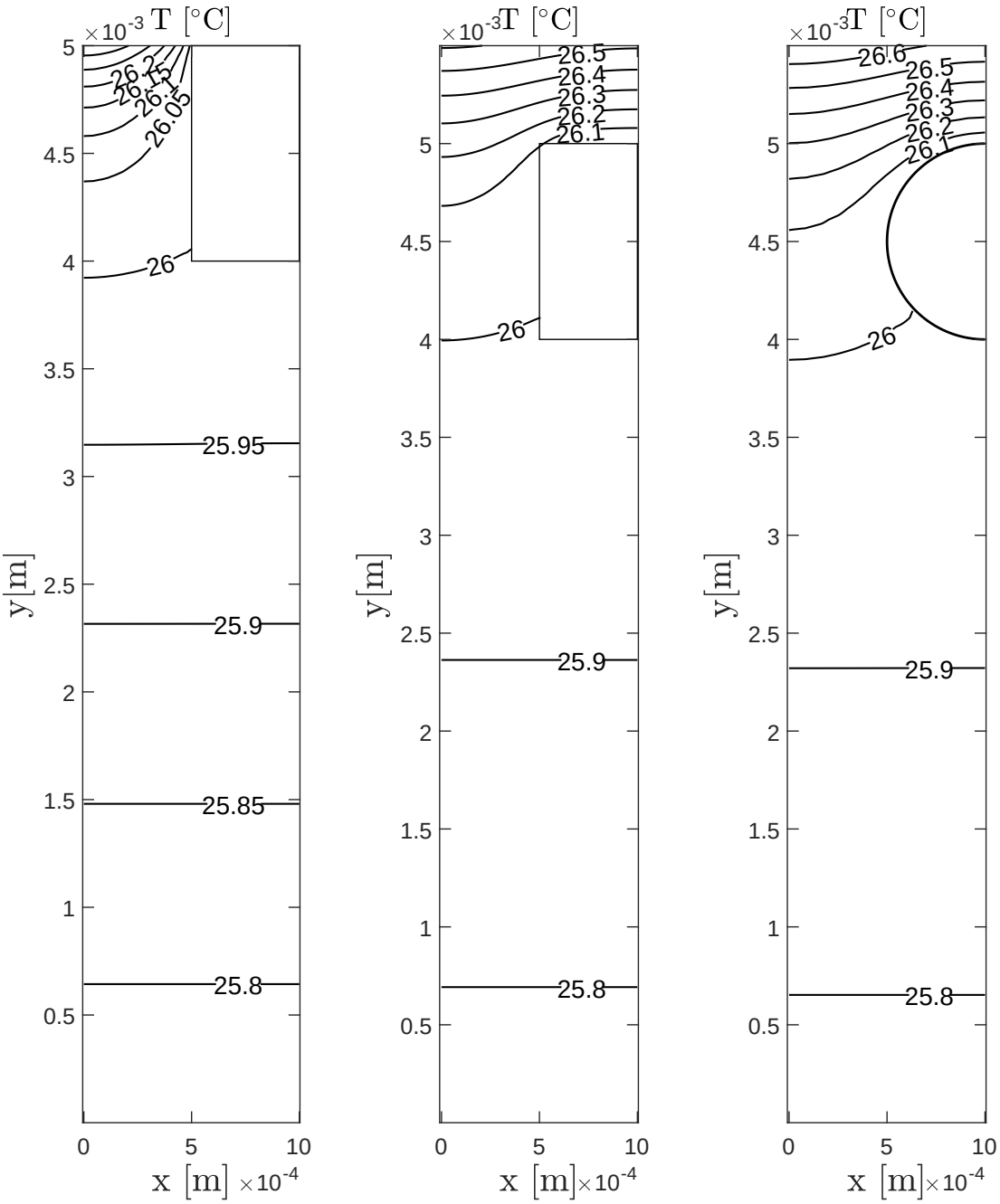

Figure 3.36: Comparison of the temperature mapping within the wick for different vapor groove shapes.

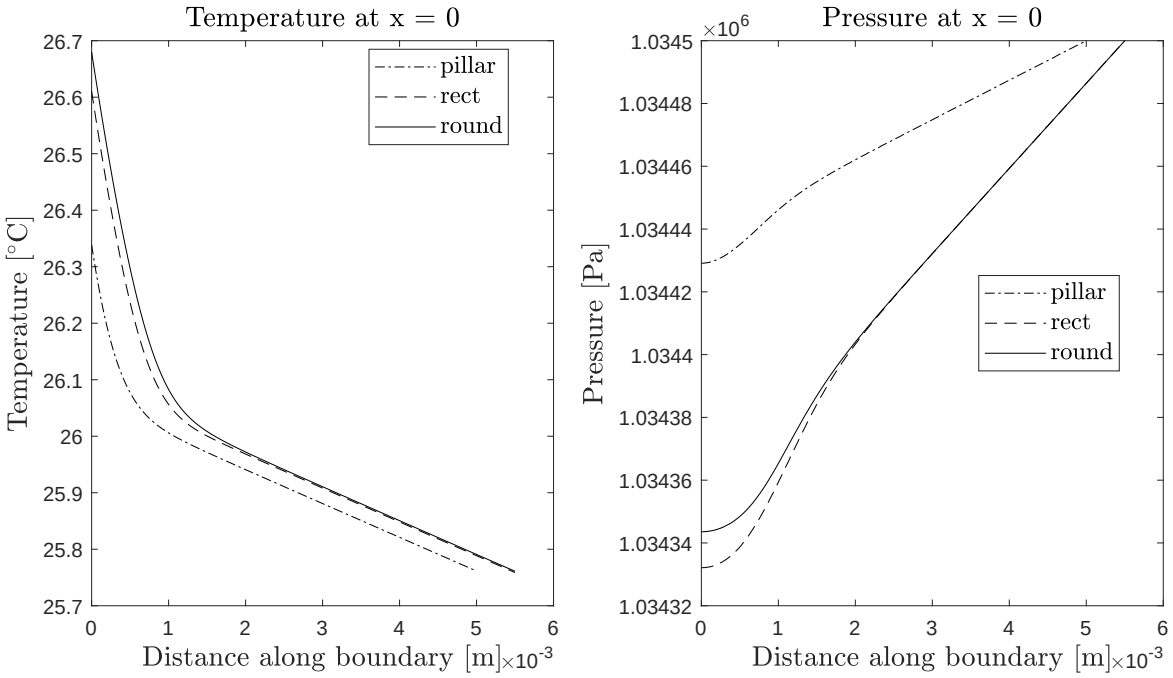

Figure 3.37: Temperature and pressure profiles along the y-axis for different shapes.

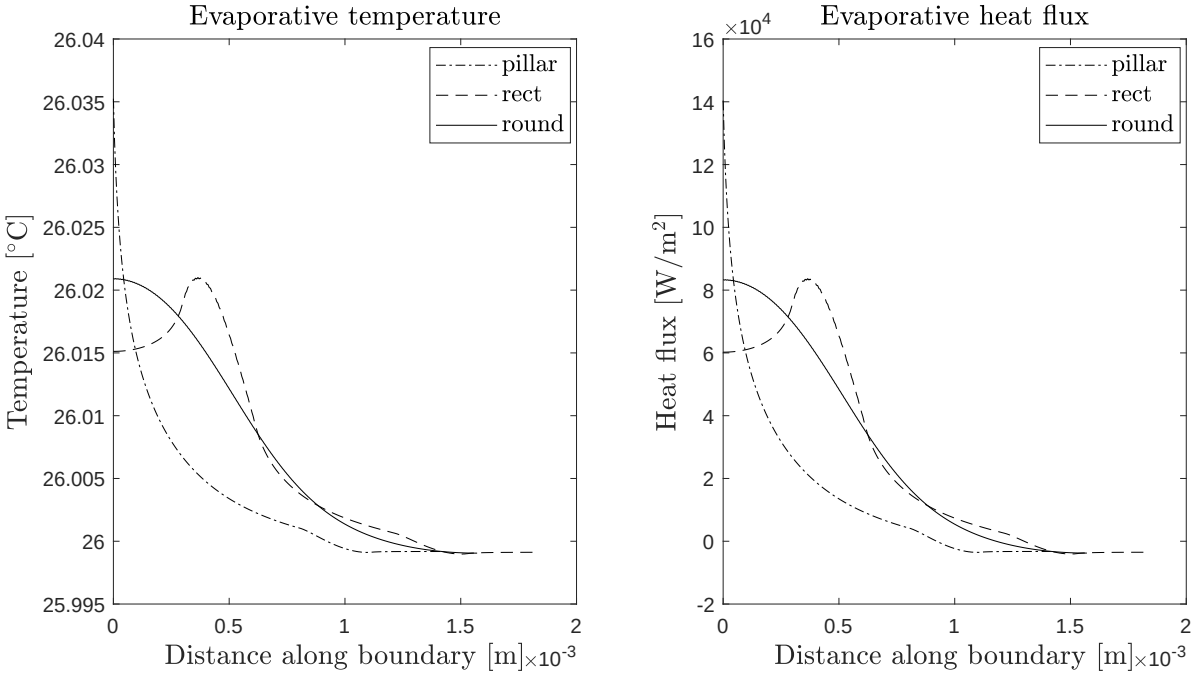

Figure 3.38: Temperature and heat flux profiles along $\partial\Omega_{ev}$ for different shapes.

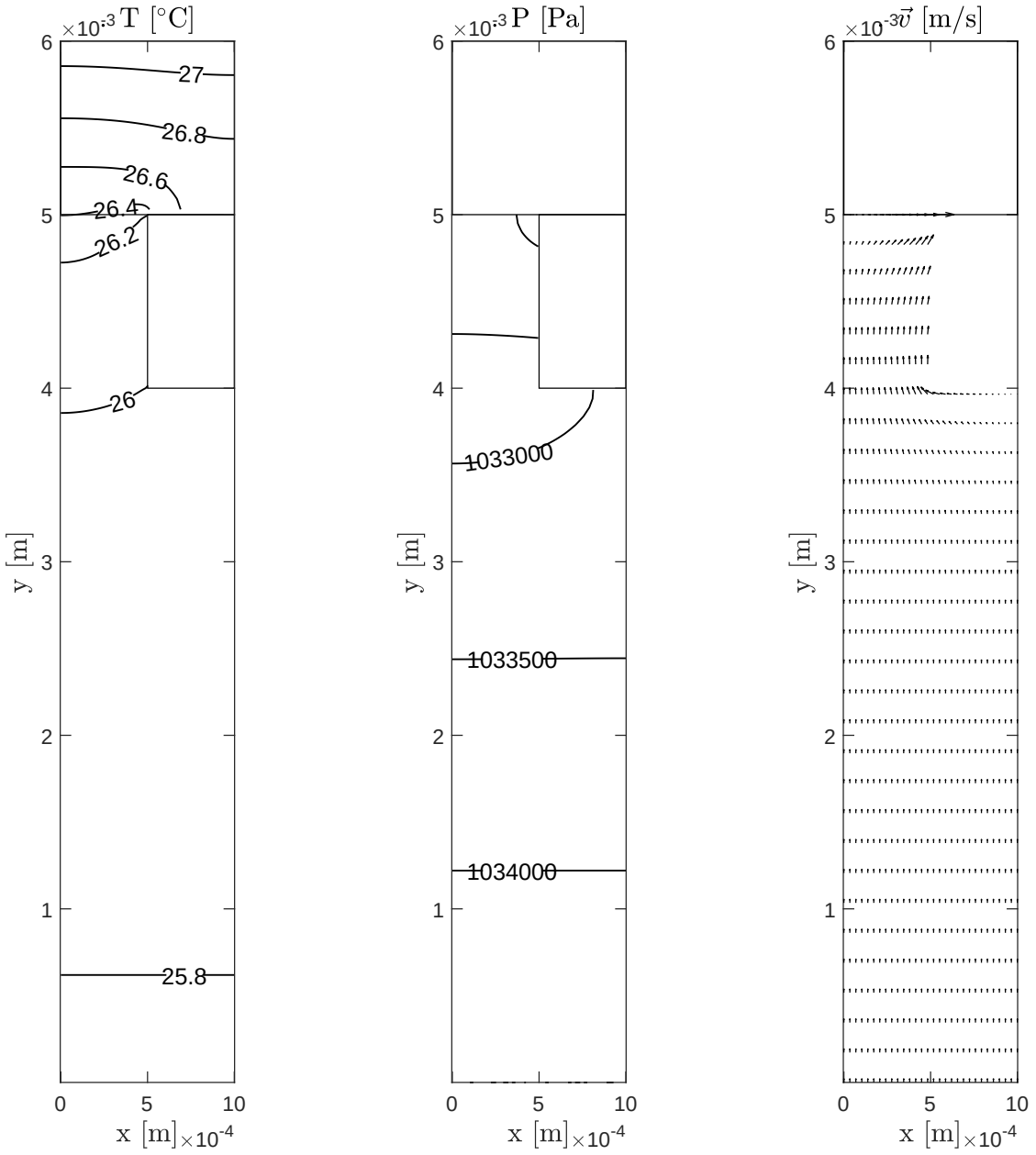

Figure 3.39: Temperature, pressure and velocity fields within the porous and solid domains of the evaporator.

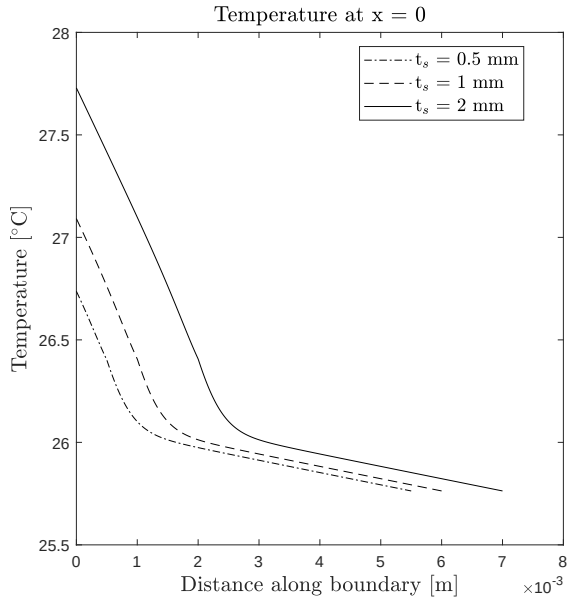

Figure 3.40: Temperature profiles along the y-axis for different case thicknesses.

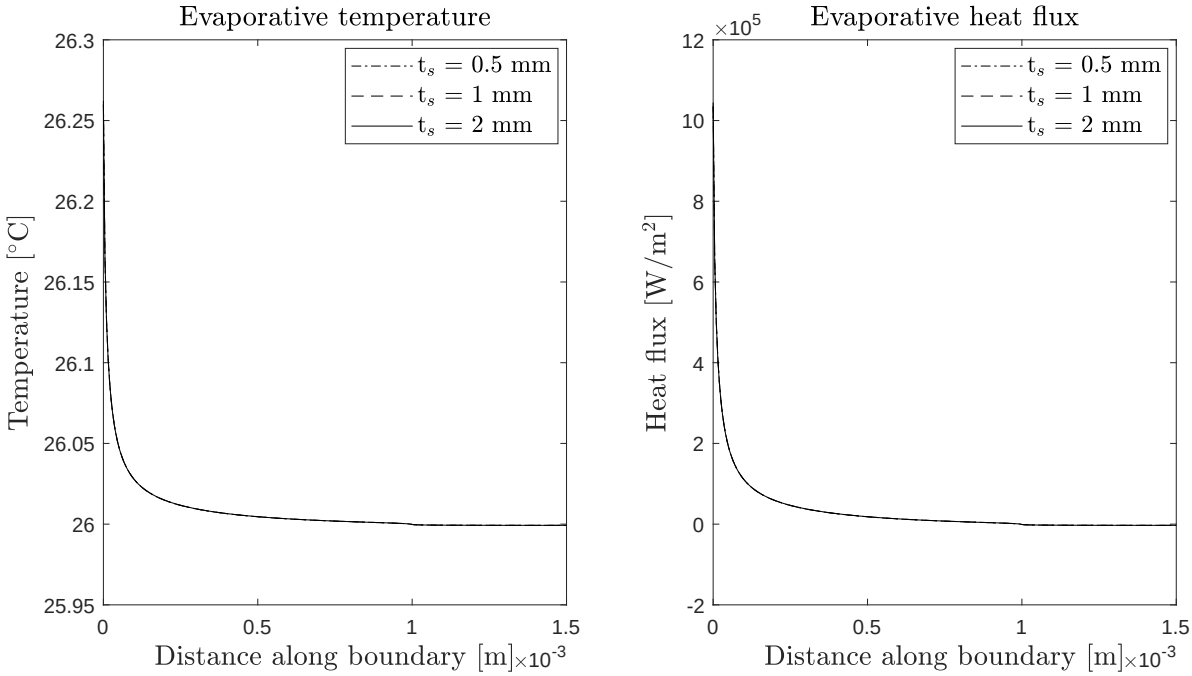

Figure 3.41: Temperature and heat flux profiles along $\partial\Omega_{ev}$ for different t_s.

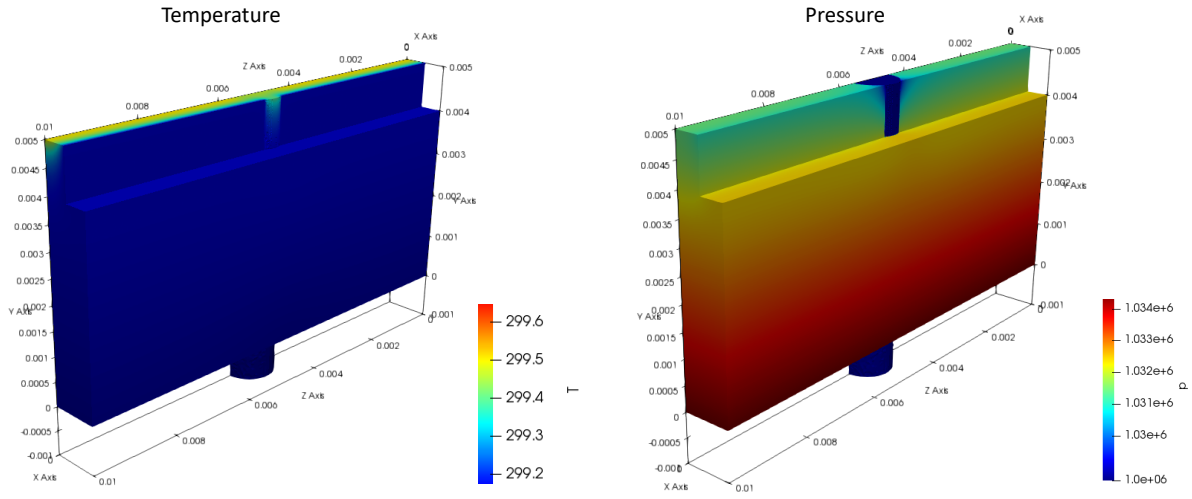

Figure 3.42: Temperature and Pressure mapping within the porous structure crossed by a 1 mm diameter strut.

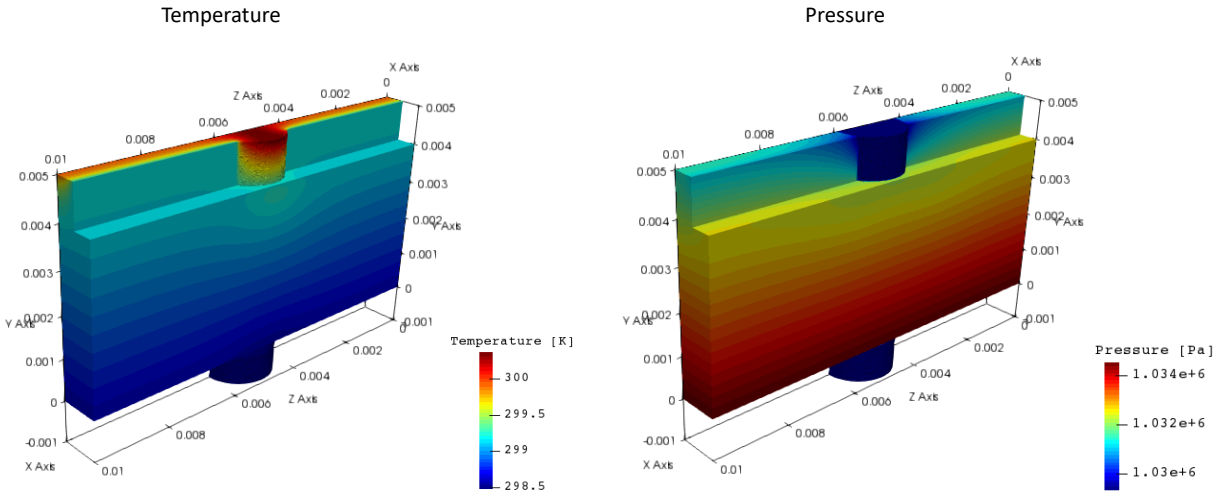

Figure 3.43: Temperature and Pressure mapping within the porous structure crossed by a 2 mm diameter strut.

Chapter 4

Experimental Setup

4.1 Introduction

An experimental setup has been built in order to investigate the heat transfer behaviour of the porous structure thermally driven by phase change phenomena and capillary forces. The literature review shows that today there are no means to reliably predict the behaviour of an evaporator during dry-out. Numerous scientific problems are still to overcome: evaporation at liquid-vapor interface in the porous medium, vapor penetration within the wick structure and heat transfer behaviour, etc. For this purpose the experimental setup here presented focuses, with minimal system complexity, on the understanding of the evaporator's elementary mechanisms. The findings are helpful to validate and improve the numerical code that has the capability to be used for the development of future two-phase evaporators for mechanically pumped fluid loops.

4.2 Objectives

The main goal of this experiment is to advance towards the understanding of the functioning of evaporator, including the effect of porous properties (permeability, porosity, thermal con-

ductivity), by means of experimental investigation and comparison with theoretical models and numerical simulation results. The objectives of the experimental campaign are:

- Experimental quantification of the evaporative heat load generated at the liquid-vapor interface
- Validation of the numerical model under steady-state conditions
- Investigation of the dry-out condition (transient) on the heat transfer and performance of the evaporator.

4.3 Experimental setup

Figure 4.1 presents the fluid loop of the experimental setup of a titanium AM evaporator. The evaporator is connected to a liquid reservoir to supply sub-cooled liquid to the wick under the same pressure conditions. The hydrostatic pressure drop is controlled by the elevation distance Δh between the upper surface of the porous structure and liquid level in the reservoir. A temperature controller regulates the temperature in the liquid chamber of the test cell through a heating film located along the tube connecting the reservoir and the evaporator. The upper surface of the porous sample is heated through a film heater. The sample is surrounded by transparent acrylic walls with a 20 mm thickness. The vapor exiting the test cell passes through a condenser and the liquid is collected in a flask. The mass of liquid condensed is measured over time. In order to reduce heat losses to the ambient environment, the test cell is surrounded by a 10 mm air gap followed by a 10 mm thermal insulation. Calibrated t-type thermocouples measure the temperatures in the porous and solid titanium sample, but also temperatures of the fluid in the vapor and liquid chambers. Other thermocouples are located on the external walls of the test cell, in the liquid reservoir and at the outlet of the condenser. The system is composed of one power supply (PS) and a data acquisition system (DAQ). Figure 4.2 shows the actual setup with the test cell inside its thermal insulation.

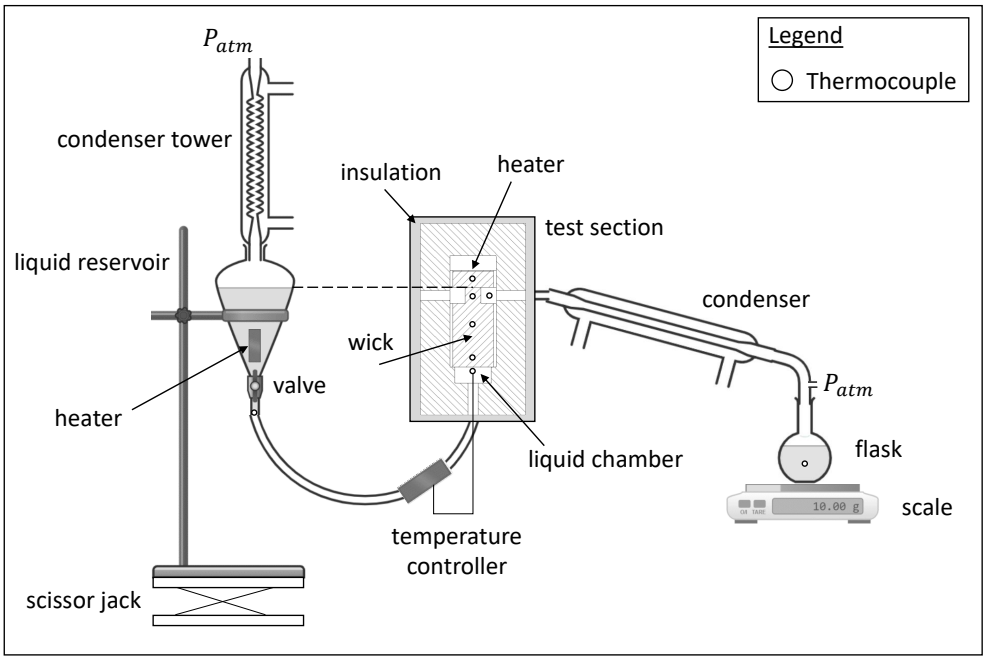

Figure 4.1: Experimental layout of the titanium AM evaporator.

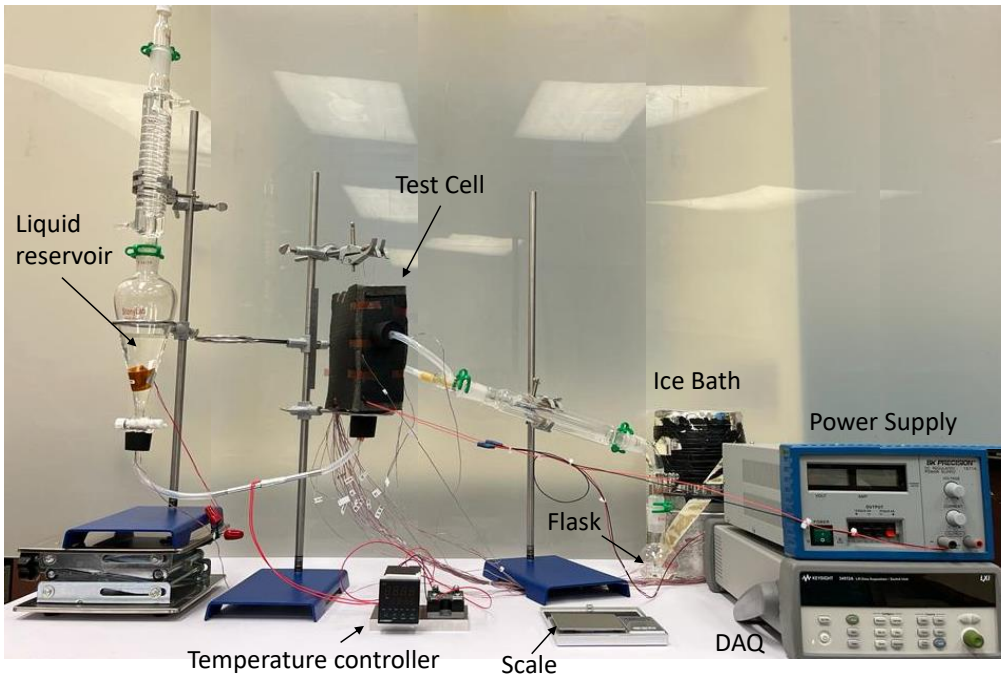

Figure 4.2: Photo of the experimental setup of the titanium AM evaporator.

4.4 Test cell

A schematic of the test section is illustrated in Figure 4.3. The Titanium AM sample, made of a solid top layer of 10 mm and a porous structure of 50 mm height, is contained within a casing made of acrylic. The AM part is surrounded by a 1 mm silicone pad that avoids any parasitic liquid flow from the bottom liquid chamber to the top.

During nominal operation, heat is applied at the top of the test cell and transferred through the wick medium filled with the working fluid, Galden PFPE-70 (see Table 4.2 for properties). The heater can provide a heat load within the range 0 - 10 W. The liquid chamber at the bottom of the wick is at a known pressure and subcooled liquid is continuously provided by a liquid reservoir. In order to sustain continuous capillary flow, the capillary pumping pressure must meet or exceed the sum of pressure drop. The maximum capillary pumping pressure can be expressed as $2\ \sigma/r_e$, where r_e is the effective pore radius.

An air gap of 10 mm is present between the acrylic walls of the case and a 10 mm K-flex thermal insulation. This allows to reduce heat losses to the ambient. The evaporator temperature is not expected to exceed 100 °C in order to reduce any chances of delamination of the foil heater.

T-type thermocouples have been installed inside 12.5 mm holes in the AM part. A mixture of epoxy and silver paste has been inserted inside the holes with two different syringes, then the hot junction of the thermocouples has been inserted and let it harden for 48 hours. Before installation, all the components of the test cell have been cleaned with acetone to remove any residual of dust.

4.4.1 Porous structure

The test sample has been fabricated at JPL using the Powder Bed Fusion Additive Manufacturing technique. Gotoh et al. [5] present a detailed experimental study on the porous properties of samples produced at JPL in AlSi10Mg, Stainless steel 316L, Inconel 625 and Ti-6Al-4V. They measure the effective pore radius, permeability and porosity. The authors

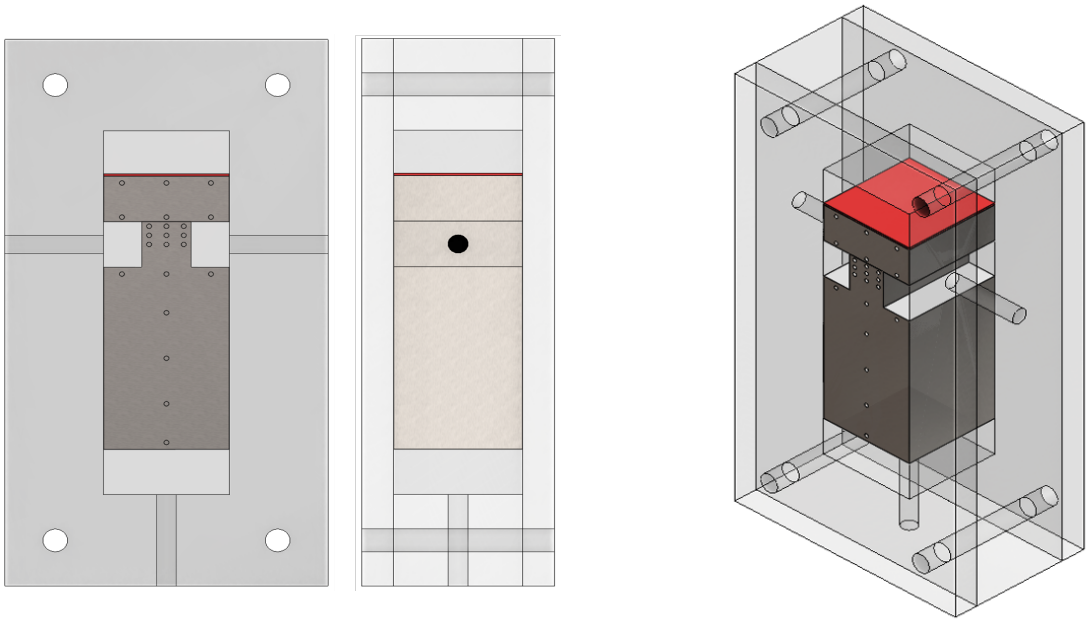

Figure 4.3: Test cell: front view (left), side view (center), 3D (right).

show that with this processes by varying the laser parameters they can obtain porous materials with pore radii from 1.1 to 28.1 μm, porosity ranging from 10.4 to 42.4 % and permeability ranging from 5.9 x 10^{-16} to 4.4 x 10^{-12} m^2. With appropriate energy density given to the laser, porosity and other parameters can be controlled. Figure 4.4 summarizes the results of the testing conduced at JPL on the porous properties and Table 4.1 shows the selected properties of the Titanium AM Evaporator. This particular combination of properties is very similar to the properties of the actual evaporator of the 2PMPL and at the same time it is free of manufacturing defects, such as cracks, thanks to high energy level of the laser.

The titanium sample has been printed horizontally on a steel substrate and then removed through the wire electron discharge machining (wire EDM). This technique, also called spark machining, is a precision manufacturing process through which a desired shape is cut within $\pm$ 0.001 mm using discharges across a fine wire minimizing the alteration of the back surface of the porous sample.

After the machining, the sample has been cleaned in an ultrasonic resonator in an acetone bath to remove any residual of dust.

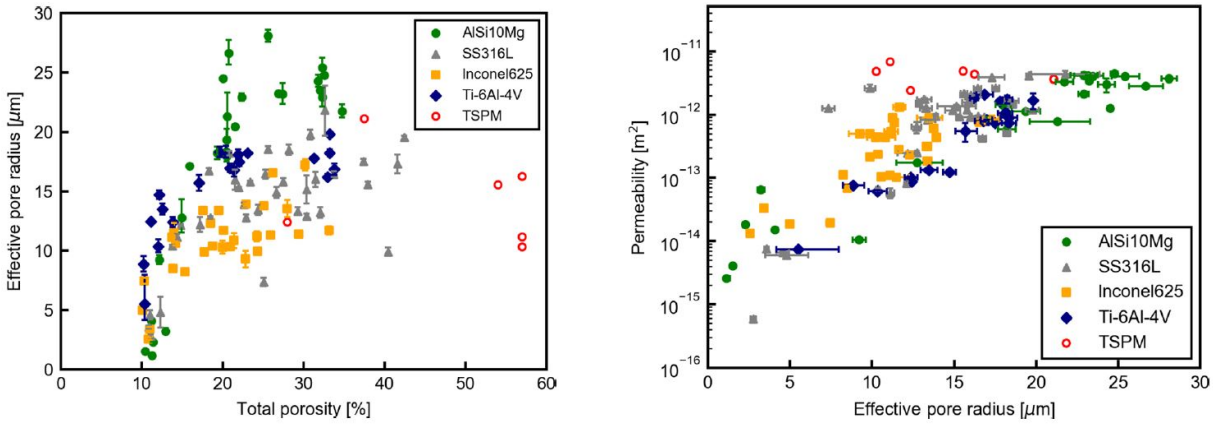

Figure 4.4: Properties of AM wick samples fabricated at JPL [5].

Table 4.1: Porous properties of the selected titanium sample.

Alloy	**Pore Radius** [μm]	**Porosity** [%]	**Permeability** [m^2]
Titanium	15.7	18.5	5.6 x 10^{-13}

Table 4.2: Thermal properties of Galden PFPE HT-70 at 1 atm.

Properties	**Units**	**PFPE HT-70**
Boiling point	^{o}C	70
Density	kg/m^3	1680
Kinematic viscosity	m^2/s	5.00E-07
Specific heat	J/kg-K	963
Heat of vaporization at boiling point	kJ/kg	71.2
Surface tension	N/m	0.014
Thermal conductivity	W/m-K	0.065
Average molecular weight	amu	410

4.5 Measurement techniques

4.5.1 Temperature measurements

T-type thermocouples have been placed inside the wick and solid structure of the AM Titanium Evaporator, and also on the external walls of the acrylic case, at the liquid reservoir, in the liquid and vapor chambers and in the flask where the condensed liquid is collected. The cold junction of the thermocouples has been placed in an ice bath to minimize the effects of the ambient temperature on the DAQ.

The thermocouples have been carefully calibrated with the complete measurement chain prior to the measurement against a Pt100 temperature probe as reference temperature. From the recorded temperatures a calibration polynomial has been calculated. All the thermocouples have found to be within ± 0.1 °C from the reference temperature.

Table 4.3: T-type thermocouples.

Parameter	**Units**	**Value**
Number	–	30
Outer diameter	mm	0.8
Range	°C	0 - 100
Accuracy	°C	0.1
Response time	s	0.02
Acquisition rate	Hz	20

4.5.2 Liquid condensate measurement

A transparent glass Graham condenser type with an internal length of the cooling tube of 10 cm condenses the vapor coming from the test cell into liquid. The liquid is collected in a flask and weighted at the end of each run to measure the condensed mass with a high precision scale with ±0.01 g resolution. A thermocouple is also located inside the flask and measures the temperature of the liquid during the test.

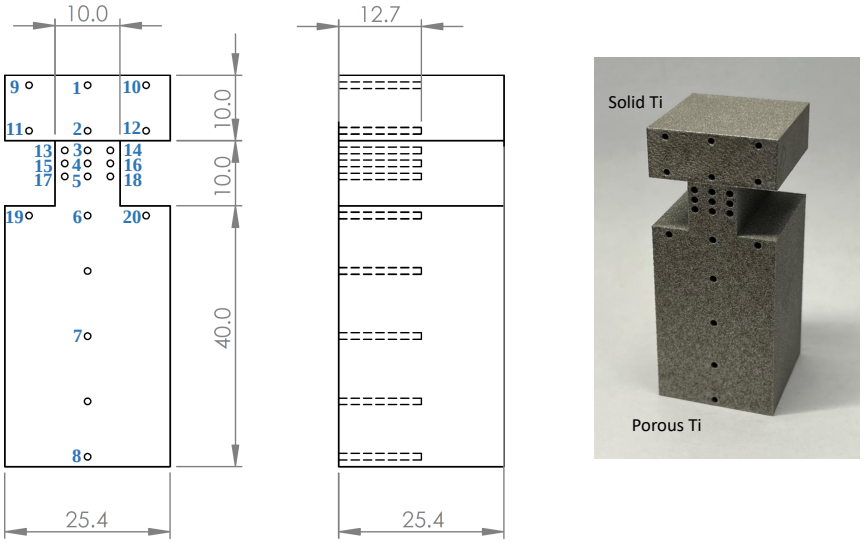

Figure 4.5: Geometry of the Titanium evaporator. Thermocouples IDs and locations (left). Additive Manufactured Titanium evaporator (right). Dimensions in [mm].

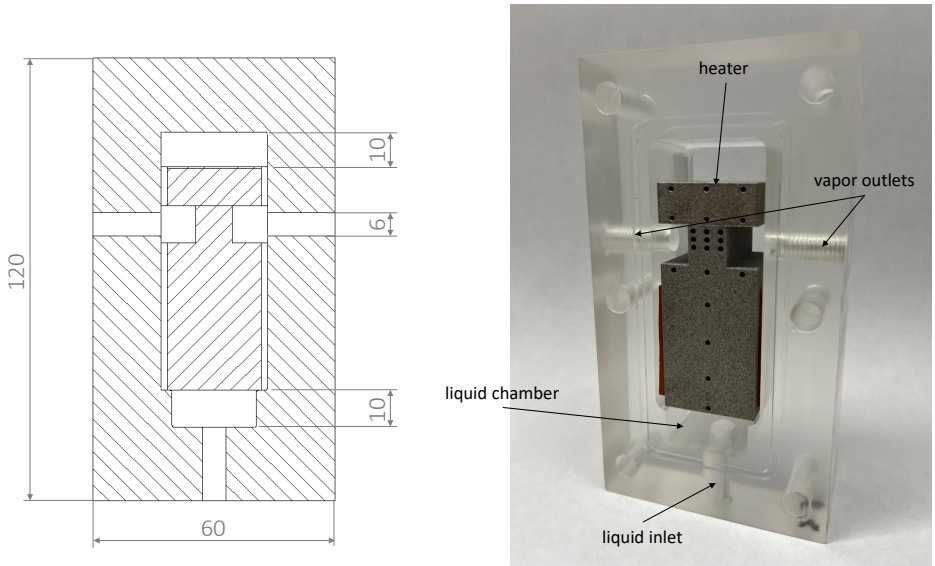

Figure 4.6: Test cell of the Titanium evaporator. Dimensions in [mm].

4.6 Experimental procedure

During the experiments the following parameters have been measured, time stamped and stored:

- Imposed heat load [W]
- Wall temperature distribution in the porous and solid structures [°C]
- Liquid channel and vapor chamber temperatures [°C]
- Mass of the liquid collected at the condenser [g]

The experiment sequence has been the following:

1. Submerge the reference thermocouple in the ice bath
2. Fill the liquid reservoir with PFPE-70 working fluid up to the desired level Δh [cm], defined as the elevation between the free liquid level in the reservoir and the solid-to-wick boundary
3. Start the DAQ recording
4. Heat the liquid in the reservoir up to the desired temperature T_{res} [°C]
5. Open the liquid inlet valve to allow flow towards the test cell
6. Once the test cell has reached steady state, switch on the evaporator heater at the desired power Q_{in} [W]
7. Record the time at which vapor starts to condense and accumulate in the flask
8. Record the time at which temperatures at the wick pillar reach saturation T_{sat} [°C]
9. Let the evaporator reach the thermal steady-state (0.1 °C/hour slope)
10. Measure the mass of the liquid condensed in the flask at the end of the test run.

To remove the air from the wick structure, prior to each test run, the liquid level in the reservoir has been adjusted slightly to the top of the porous structure and heat load has been applied to keep at saturation conditions the top part of the wick pillar. Then, the liquid level at the reservoir has been adjusted to the required elevation Δh.

One experimental run is defined as the acquisition of the measured parameters (temperatures of the solid and porous titanium structures, loop temperatures and mass of the condensed liquid) associated to a set of the input parameters (such as heat input power). The total number of runs for the porous sample are therefore 30. The time required for each run is 6 hours to reach desired conditions: [4 hours (reaching steady state condition) + 2 hours (time to acquire diagnostics)] x 3 series of acquisitions. Consequently, the total experiment time is 540 hours: 30 runs x time required for each run (6 hours) + instruments calibration. Appendix A summarizes the main data collected during the test runs.

4.7 Uncertainty analysis

The uncertainty analysis has been performed following the uncertainty estimation method of Kline and McClintock [38]. The uncertainty related to the tools (multimeter, DAQ, heater and thermocouples) used in this experiment is tabulated in Table 4.4.

A Root Sum of Squares (RSS) analysis has been carried out in order to determine the typical uncertainty in the heat loads measurement. The heat input can be expressed as function of the applied voltage and heater resistance

$$Q_{in} = \frac{V^2}{R} \tag{4.1}$$

and the relative uncertainty of Q $_{in}$ is

$$w_Q = \sqrt{\left(\frac{dQ}{dV} w_V\right)^2 + \left(\frac{dQ}{dR} w_R\right)^2} \tag{4.2}$$

The evaporative heat load is measured as

$$Q_{ev} = \dot{m}_l h_{fg} \tag{4.3}$$

Table 4.4: Uncertainty of measurements.

	Error Source	**Uncertainty**
Keithley 2400 multimeter	Voltage	0.02 % + 600 μV
Agilent 39470 A DAQ	T-type	0.2 °C
Minco heater	Resistance	0.1 Ω

where $\dot{m}_l$ is the liquid collected at the flask after the condenser over the time of the test run. At least 100 g are collected per run and it is conservatively assumed that around 5 g are trapped along the path from the vapor chamber to the flask.

The resulting uncertainty in the heat input measurement is 1.5% of the total power applied. This means that for a 4 W applied, the relative uncertainty is 0.06 W. While for the evaporative heat load it is 5% that corresponds to 0.1 W of the evaporative heat load.

4.8 Experimental validation

Preliminary tests have been conducted in order to validate the assumptions made in the numerical model on thermal properties such as thermal conductivity and on the contact resistance between the solid and the porous media.

Several tests have been performed with different powers and they have been repeated for 5 times for repeatability. Figure 4.7 shows a pure conduction test with an heat input of 1.5 W. A thermal contact resistance between the solid and porous parts is the reason of the temperature gap present in the plot. For this reason the numerical model has been corrected with a thermal conductance value of 0.1 W/cm^{2}K. Table 4.5 summarizes the thermal conductivities of the different materials of the test cell, included the solid and porous AM parts.

Figure 4.8 illustrates the temperature profile along the y-axis (symmetry axis). It is possible to notice a good agreement between the numerical and experimental results. Table 4.6 summarizes the calculated heat balance in the test cell. Out of 1 W that goes to the porous structure, 0.4 W are the heat losses towards the case and the thermocouples.

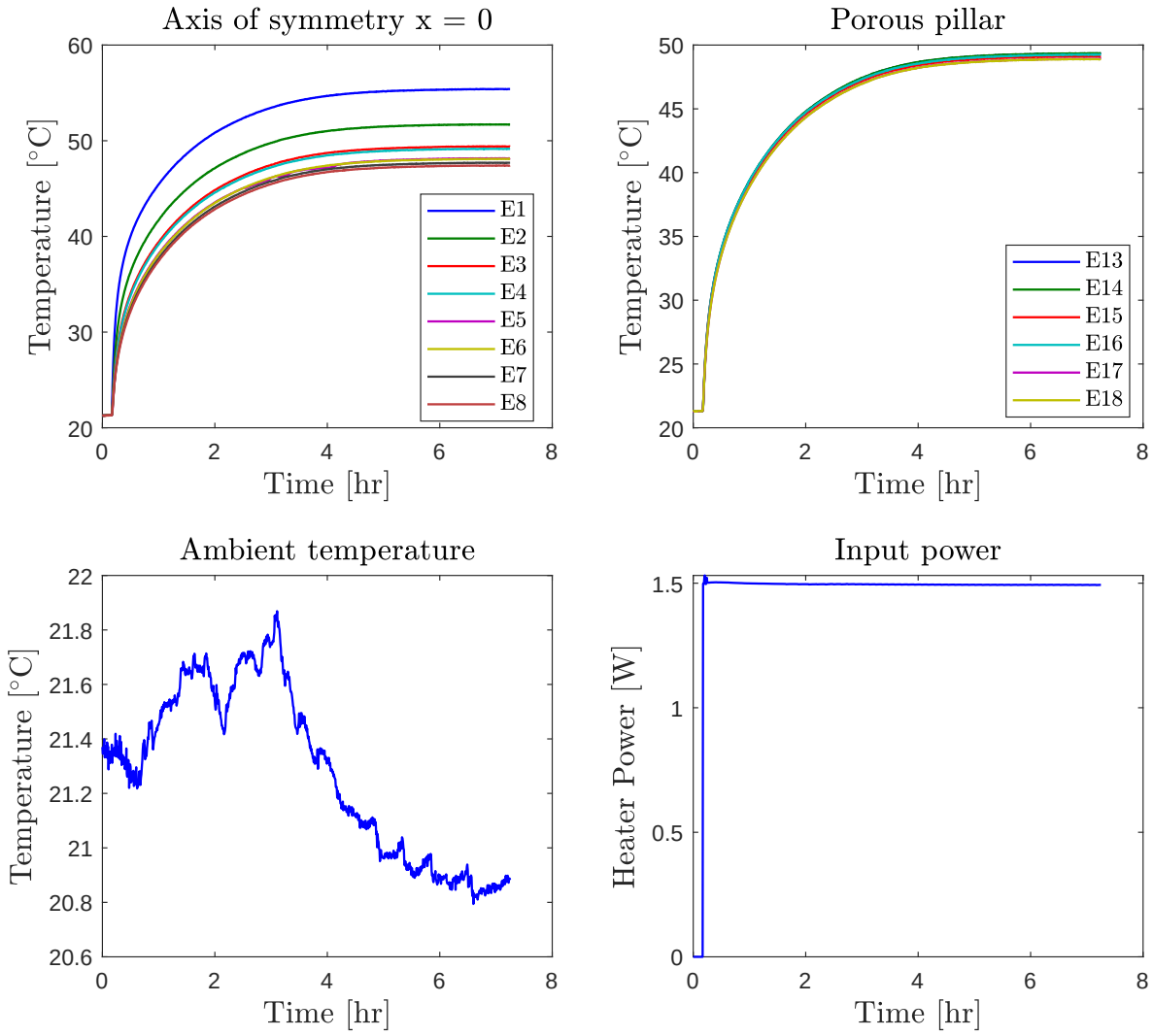

Figure 4.7: Test case 11 with inlet power of 1.5 W (pure conduction).

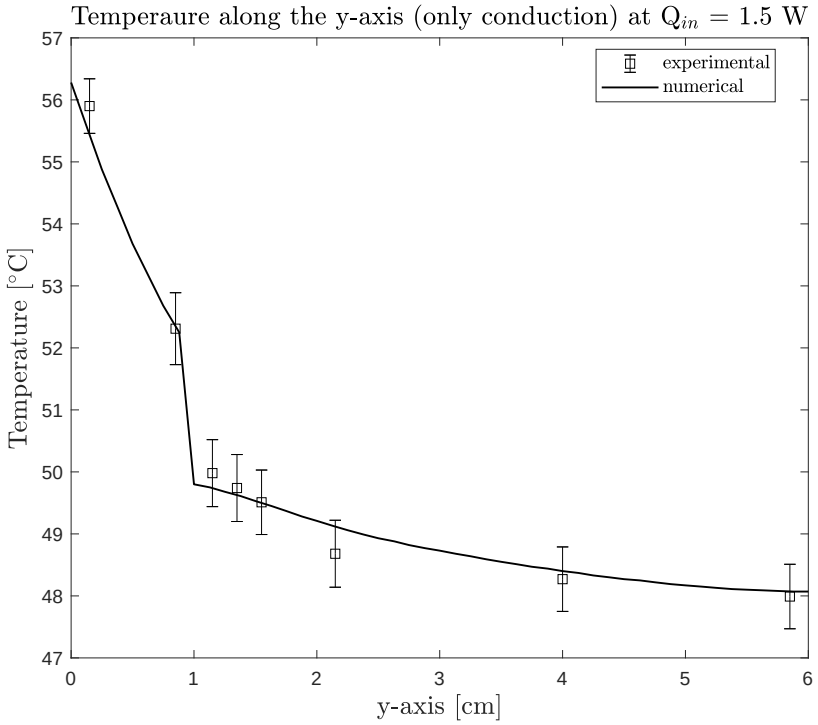

Figure 4.8: Temperature along the y-axis with an inlet power of 1.5 W (pure conduction).

Table 4.5: Estimated thermal conductivities.

Material	**Thermal conductivity [W/m-K]**
Acrylic	0.2
Silicone	0.3
Solid Titanium	6
Porous Titanium	5.5
Air	0.025

Table 4.6: Calculated energy balance (pure conduction).

Heat load	**Q [W]**
Heat input	1.5
Heat to the wick	1
Heat loss to the case	0.35
Heat loss through TCs	0.05
Total heat losses	0.4

4.9 Experimental results: steady-state

The first objective of the experimental campaign is to find the operational conditions at which the capillary flow is taking place under certain input heat loads. Figure 4.9 illustrates a typical test run. IDs and locations of the thermocouples are provided in Figure 4.5. An heat input of 4 W is applied at the heater when the liquid level is located at the top interface of the wick Δh = 0 cm as illustrated in Figure 4.1.

The test takes place over 4 hours and evaporation starts to occur after two hours when the vapor is at saturation temperature T_{sat} = 70 °C. Thermocouples E1 - E8 are located along the axis of symmetry (y-axis) with E1 located 1.5 mm below the surface where the heater is applied. Both E1 and E2 are placed in the solid structure, while E3 - E8 are located within the wick. Due to the thermal contact resistance between the solid and porous structures it is possible to observe a temperature gap between E2 and E3. Thermocouples E13 - E18 are located 1.5 mm below the evaporative boundary. At steady-state they all reach a value above the saturation condition.

The liquid temperature in the liquid chamber (TC located at its center) increases monotonically during the test up to 46 °C. This configuration respects the working conditions of the JPL evaporator. The main difference is that since the height of the liquid chamber is larger, a temperature stratification is present. Ambient conditions during the test are stable within 1 °C.

The vapor coming out the vapor chamber goes through a condenser and is accumulated inside a flask. The liquid collected during the steady-state phase (last hour) has been measured at the end of the test run and it corresponded to 104 g. Since $Q_{ev} = \dot{m}_l \ h_{fg}$, this is equivalent to an evaporative heat load of 2.2 $\pm$ 0.1 W.

The test has been repeated 3 times for reproducibility proposes.

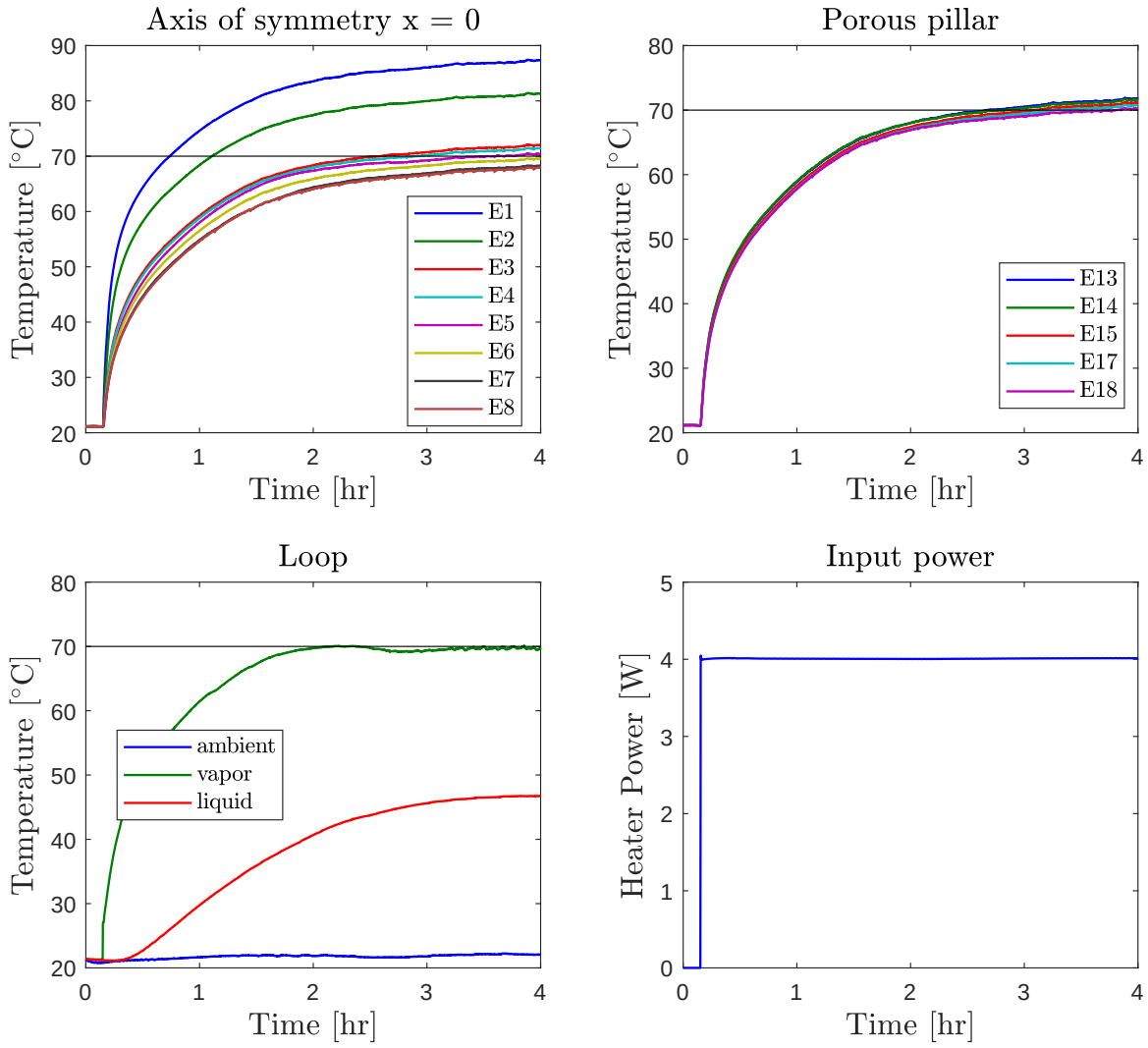

Figure 4.9: Test case 23 with inlet power of 4 W and $\Delta h = 0$ cm.

4.10 Numerical results in the experimental conditions

The second objective of the experimental campaign is the validation of the numerical model. The numerical model has been modified to match the experimental conditions including the effect of gravity.

Table 4.7 summarizes the main boundary conditions, wick properties and geometrical inputs to the model. When $\Delta h = 0$, the inlet pressure is 1.008 atm, while the outlet pressure is at 1 atm. The evaporative heat transfer coefficient is calculated in agreement with equation 3.14 with constant thermal properties at 1 atm and its value corresponds to 9.6 x 10^4 W/m^2 K.

Figure 4.10 shows the temperature, pressure and velocity fields along the porous structure for the experimental test run presented in the previous paragraph with an input heat load of 3 W. It is possible to observe that only a 4 °C temperature gradient is present between the top and bottom boundary of the wick structure. As expected, the liquid flow along the domain is mostly one dimensional in the base of the wick and becomes 2D in proximity of the liquid-vapor interface.

Figure 4.11 and Figure 4.12 illustrate the temperature and pressure profiles along the axis of symmetry x = 0 and the evaporative boundary and they compare it to the experimental values. Both plots present a good agreement between the experimental and numerical values of the temperature profile and heat fluxes. However only the numerical model is able to give the accurate temperature profile, characterized by a smaller gradient, and heat flux along the evaporative boundary.

Table 4.8 summarizes the heat balance calculated by the numerical model. Out of 4 W applied at the input heater, 3 W go to the top boundary of the porous media. This value corresponds to 0.47 W/cm^2. Heat losses towards the case are 0.6 W and towards the liquid are 0.15 W, for a total of 0.8 W. The numerical model confirms that the heat load to evaporation is 2.2 ± 0.1 W.

Table 4.7: Boundary conditions, wick properties and geometrical inputs to the numerical model.

Parameter	**Units**	**Value**
Heat input	W	4
Liquid temperature	°C	46
Liquid pressure	atm	1.008
Convective heat transfer coefficient	W/m^2-K	100
Vapor pressure	atm	1
Saturation temperature	°C	70
Evaporative heat transfer coefficient	W/m^2-K	9.6 x 10^4
Effective thermal conductivity	W/m-K	5.5
Porosity	%	18.5
Permeability	m^2	5.6 x 10^{-13}
Effective pore radius	μm	11.7
L_x	cm	1.27
L_y	cm	4
L_{xp}	cm	0.5
L_{yp}	cm	1

Table 4.8: Calculated energy balance.

Heat load	**Q [W]**
Heat input	4
Heat to the wick	3
Heat loss to the case	0.6
Heat loss to the liquid	0.15
Heat loss through TCs	0.05
Total heat losses	0.8
Heat to evaporation	2.2

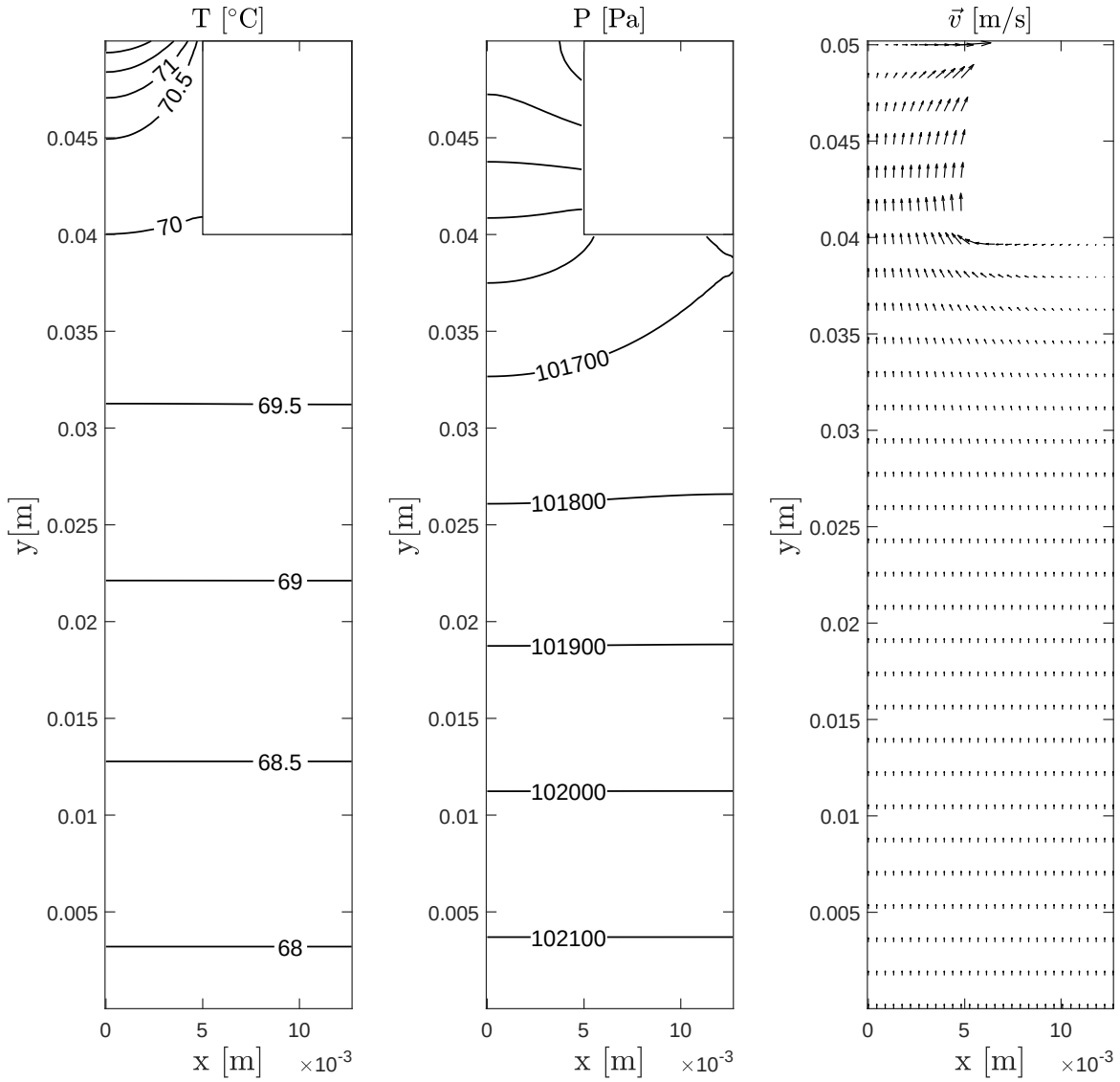

Figure 4.10: Numerical temperature, pressure and velocity fields in the experimental conditions at $Q_{in} = 4$ W.

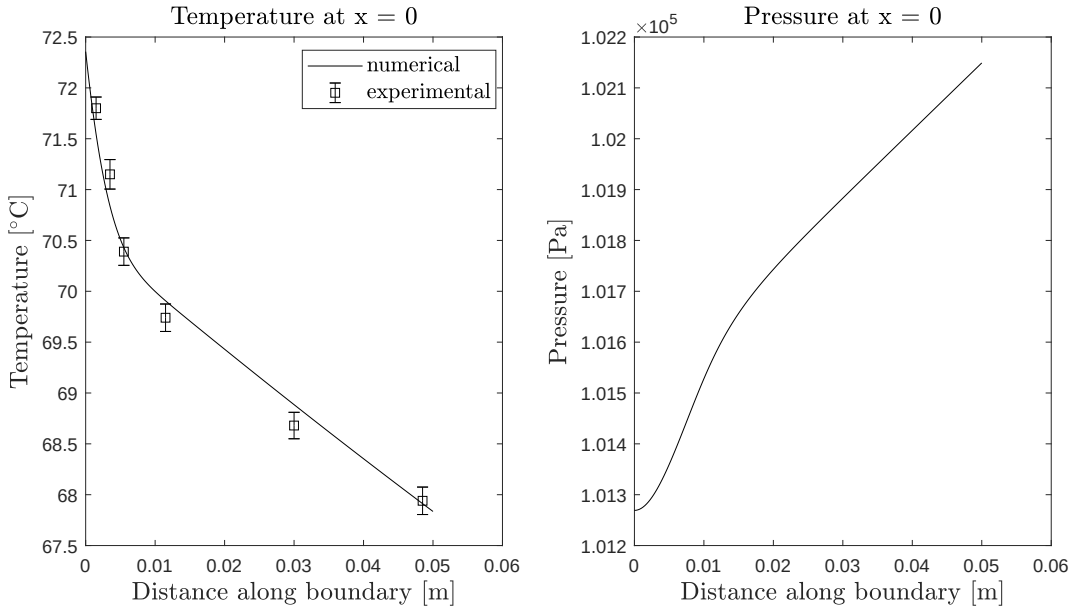

Figure 4.11: Temperature and pressure profiles along the y-axis for $Q_{in} = 4$ W.

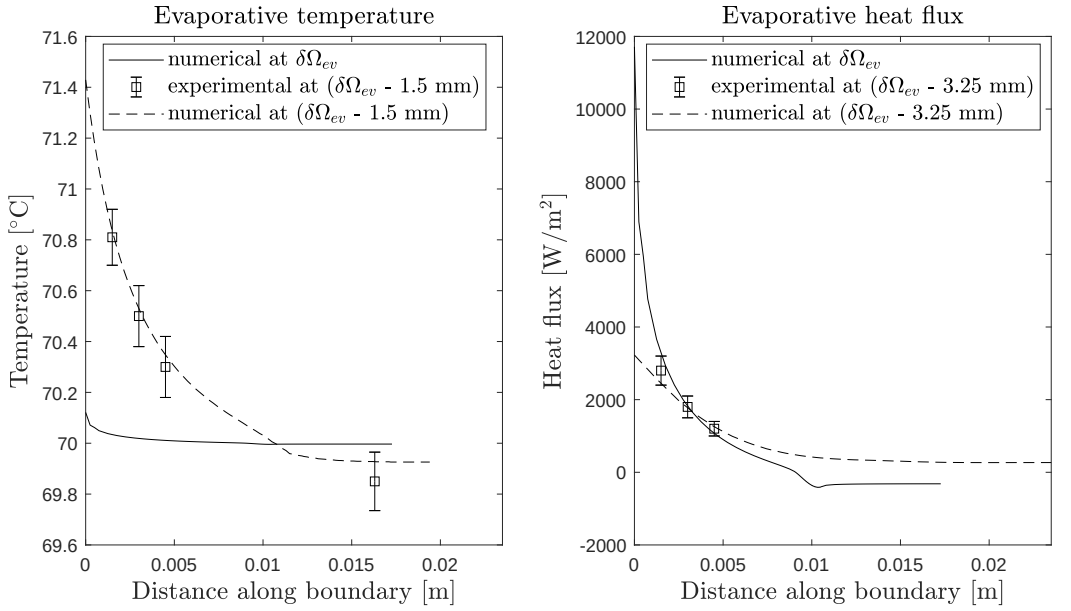

Figure 4.12: Temperature and heat flux profiles along $\partial\Omega_{ev}$ for $Q_{in} = 4$ W.

4.11 Experimental results: thermal transients

The third objective of the experimental campaign is the study of the transient conditions such as dry-out. The literature review shows that today there are no means to reliably predict the behaviour of a evaporator during dry-out. The experimental campaign remains the only way to characterize this condition for porous media.

Figure 4.13 shows a test run with an inlet heat load of 4 W at an elevation of $\Delta h = 0$ cm. The first part of the test shows the repeatability of the test previously described, while in the second part the elevation Δh is increased to 1 cm (located at the base of the wick pillar). It is possible to observe that all temperatures increase. In particular thermocouple E8 (located at 1.5 mm inside the bottom surface of the wick) measures a temperature of 76 °C above the saturation temperature of 70 °C. Oscillations are observed at the thermocouple located inside the liquid chamber and the vapor temperature increases also above saturation. The experimental results suggest that not only dry-out takes place at the top of wick pillar due to temperature values way above the boiling limit, but also bubbles at the bottom interface of the wick are formed and merged in a single slug, forcing the oscillation of temperature recorded by the thermocouple located at the center of the liquid chamber. During this phase no liquid condensation has been observed at the collecting flask.

Such increase of the temperatures of the solid and wick parts can be explained due to the penetration of the vapor within the porous structure caused by the adverse hydrostatic pressure. In particular, an increase of the hydrostatic pressure drop reduces the supply of the liquid at the liquid-vapor interface. The vapor expands in the wick invading more pores, the temperature of the casing increases and the heat transfer performances are degraded. An increase of Δh leads to a decrease of the liquid mass flow rate that supplies the top boundary of the wick and causes an overheating of the casing. Moreover, it is interesting to notice that failure does not come only from the dry-out at the top region, but also from the fact that the bottom base of the wick reaches saturation conditions with consequent formation of nucleation and bubble expansion closing the liquid supply to the porous structure.

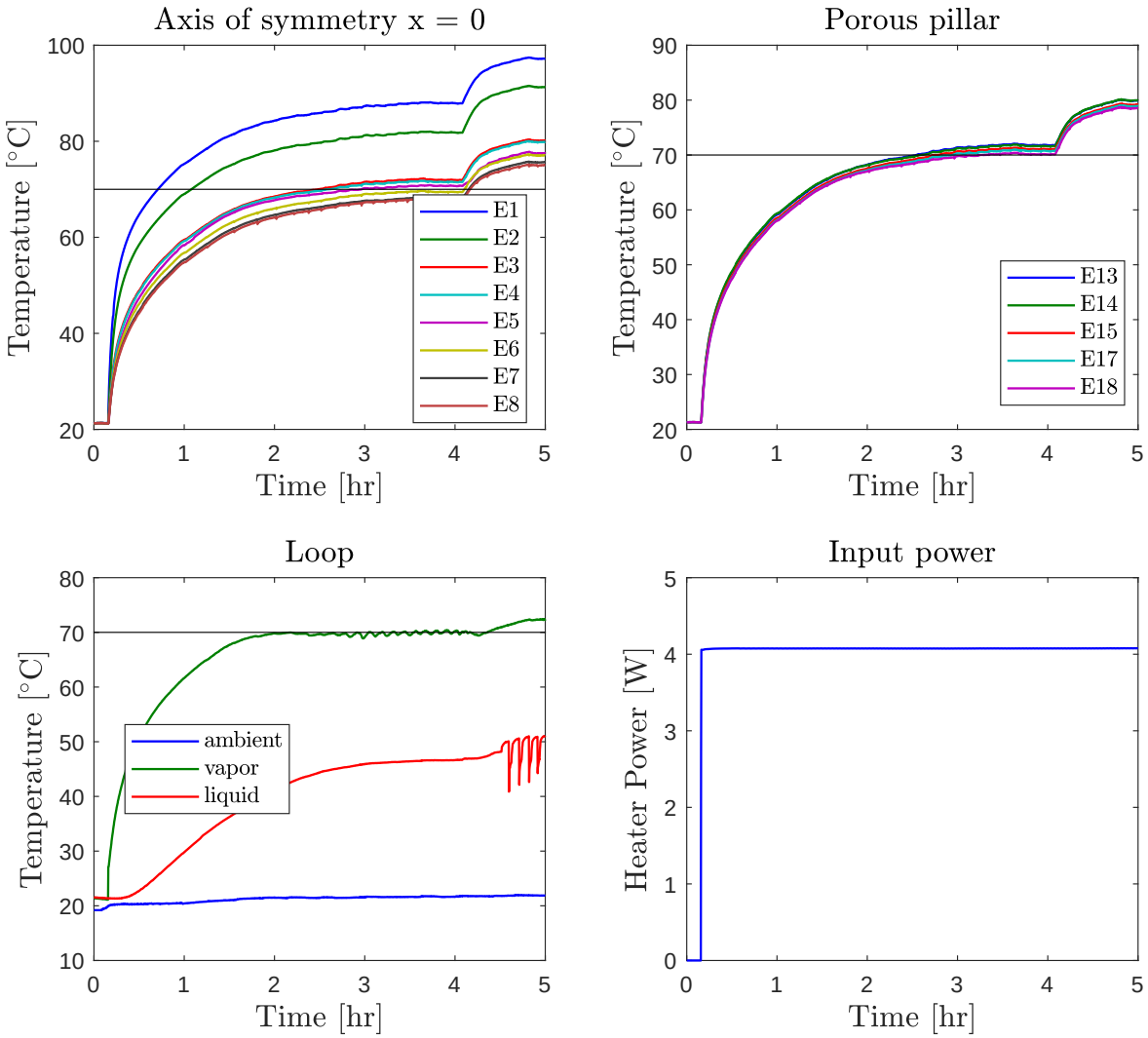

Figure 4.13: Test case 24 with inlet power of 4 W and $\Delta h = [0, 1]$ cm.

Chapter 5

Conclusions

A novel additively manufactured evaporator has been developed at NASA Jet Propulsion Laboratory as part of a Two-Phase Mechanically Pumped Loop for spacecraft thermal management. Understanding the heat and mass transfer within the porous structure of the evaporator and how it is connected to the dynamics of the liquid-vapor interface is fundamental to characterize the performance of the evaporator and also to design the next generation of 2PMPL.

This research work, conducted at the Boiling and Phase Change Laboratory at UCLA, has produced a numerical tool that facilitates the understanding of the physical aspects at the base of the heat and mass transfer within the porous structure of an evaporator. A wick model based on continuity, momentum and energy equations together with a particle model valid at the liquid-vapor interface along the wick-to-vapor groove boundary have been developed. An experimental setup has been also built in order to validate the numerical calculations and to investigate the transient behaviours of a capillary driven titanium evaporator. A good agreement has been obtained between the experimental and numerical results. The main conclusions of this research work can be summarized as follows:

1. During nominal conditions, evaporation occurs along the wick-to-vapor groove interface with variable intensity, increasing in proximity of the heat source. Heat transfer is a

result of the combination of evaporation, heat conduction within the porous media and convection of the cooling working liquid.

2. The material properties of the wick and of the fluid significantly influence the heat transfer performances of the evaporator. For instance, the effective thermal conductivity affects the temperature gradient within the wick and the heat losses to the liquid chamber. Permeability mainly affects the pressure drop across the porous structure. Porosity does not have great effect on the evaporative heat load, but it influences the pressure drop along the wick. Ammonia is a better candidate as working fluid compared to acetone for an aluminum wick.

3. The geometrical features of the wick have a strong effect on the heat transfer within the evaporator. For instance, the thickness of the porous base affects both the temperature gradient and the pressure drop in the wick. Thinner pillars with a higher density per area would greatly improve the heat transfer. Technological limitations, however, might come from manufacturing capabilities. The wick pillar configuration is the best option between solid pillar, rectangular and round vapor groove chambers. The thickness of the case does not affect the performance of the wick, but it influences the maximum temperature externally reached. The struts slightly reduce the performances of the wick since they introduce a heat path towards the liquid chamber.

4. Dry-out at the wick-to-vapor groove boundary due to recession of the meniscus within the solid particles takes place at high superheat values. This means that dry-out is likely to occur before in the wick at the boundary where the heat input is applied than the evaporative boundary.

5. The operational conditions of the porous structure subject to a heat input are limited by three main conditions: (1) capillary limit, caused by the insufficient capillary pressure at the liquid-vapor interface able to bring enough liquid flow to the evaporating surface; (2) nucleation limit, due to vapor bubble generation within the wick originated by a

high input heat flux; (3) bubble nucleation and vapor expansion at the liquid inlet surface causing a dry-out of the entire wick and stop of condensation.

6. The adverse hydrostatic pressure acting on the porous structure inhibits the liquid mass flow rate from the liquid chamber to the evaporating boundary. This causes bubble nucleation and vapor expansion towards adjacent pores with effects on the temperature increase of the casing and the wick and degradation of the overall heat transfer performances.

Appendix A

Titanium Evaporator - Experimental Journal

Legend:

- Cond./amb. - pure conduction test without insulation
- Cond. - pure conduction test with insulation
- Evap. - evaporation test
- P/ NP - Passed / Not Passed
- Q - input power [W]
- Δh - elevation between liquid level at reservoir and top porous boundary [cm]
- T_l - liquid temperature [°C]
- T_{wick}^{min}, T_{wick}^{max} - minimum and maximum temperature in the wick [°C]
- T_{solid}^{max} - maximum temperature in the solid [°C]
- m_l - mass of the liquid collected after condensation [g]

Table A.1: Experimental journal of the tests on the Titanium AM Evaporator.

Test	**Event**	**P/NP**	**Q [W]**	**Δh [cm]**	**T_l [°C]**	**T^{max}_{solid} [°C]**	**T^{max}_{wick} [°C]**	**T^{min}_{wick} [°C]**	**m_l [g]**
1	Cond./amb.	P	0.5, 1, 1.5	-	-	30.5, 38.2, 46.2	29.2, 36.0, 42.8	28.5, 34.7, 40.8	-
2	Cond./amb.	P	0.5, 1, 1.5	-	-	30.8, 38.9, 46.2	29.3, 36.1, 42.2	28.6, 34.8, 40.3	-
3	Cond./amb.	P	0.5, 1, 1.5	-	-	30.5, 38.3, 46.4	29.3, 36.3, 43.3	28.7, 35.1, 41.4	-
4	Cond./amb.	P	0.5, 1, 1.5	-	-	30.7, 38.6, 46.0	29.7, 36.5, 43.2	29.1, 35.3, 41.4	-
5	Cond./amb.	P	0.5, 1, 1.5	-	-	30.9, 39.4, 46.1	29.8, 37.4, 43.3	29.2, 36.1, 41.4	-
6	Cond.	P	0.5	-	-	34.4	32.4	31.7	-
7	Cond.	P	1	-	-	45.7	41.8	40.5	-
8	Cond.	P	1.5	-	-	56.1	50.4	48.5	-
9	Cond.	P	0.5	-	-	34.8	32.6	31.9	-
10	Cond.	P	1	-	-	46.1	41.9	40.5	-
11	Cond.	P	1.5	-	-	56.4	50.4	48.4	-
12	Cond.	P	0.5	-	-	34.5	32.3	31.6	-
13	Cond.	P	1.5	-	-	56.2	50.1	48.1	-
14	Cond.	P	1	-	-	45.8	41.6	40.2	-
15	Evap.	NP	2	5	-	-	-	-	-
16	Evap.	NP	2	0	-	-	-	-	-
17	Evap.	P	2, 2.5, 3	3.2	37	63.3, 70.4, 76.5	54.7, 60.0, 64.2	52.0, 56.7, 60.4	-
18	Evap.	P	3.2	3	37	77.8	65.5	62.2	-
19	Evap.	P	2.5	1	35	68.1	68	54.3	10
20	Evap.	P	4	0	48	89.8	73.9	69.4	104
21	Evap.	P	5	0	44.1	96.8	76.6	71.1	71
22	Evap.	P	3.5	0	48	79	68	64	20
23	Evap.	P	4	0	47	89.5	73.5	69.2	100
24	Evap.	P	4	0, 1	46	89.7	74	69.1	101
25	Evap.	P	3	0, 1	37	77, 87	65, 73	61, 70	51
26	Evap.	P	4	0	48	90	73.8	69.7	98
27	Evap.	P	5	0	44	96.8	76.6	71.1	75
28	Evap.	P	5, 3	0	47	97, 76	78, 65	72, 61	105
29	Evap.	P	3	0, 5	37	76, 90	64, 78	60, 73	51
30	Evap.	P	4	0, 1	48	89.3	73.4	69.6	97

Appendix B

Drawings

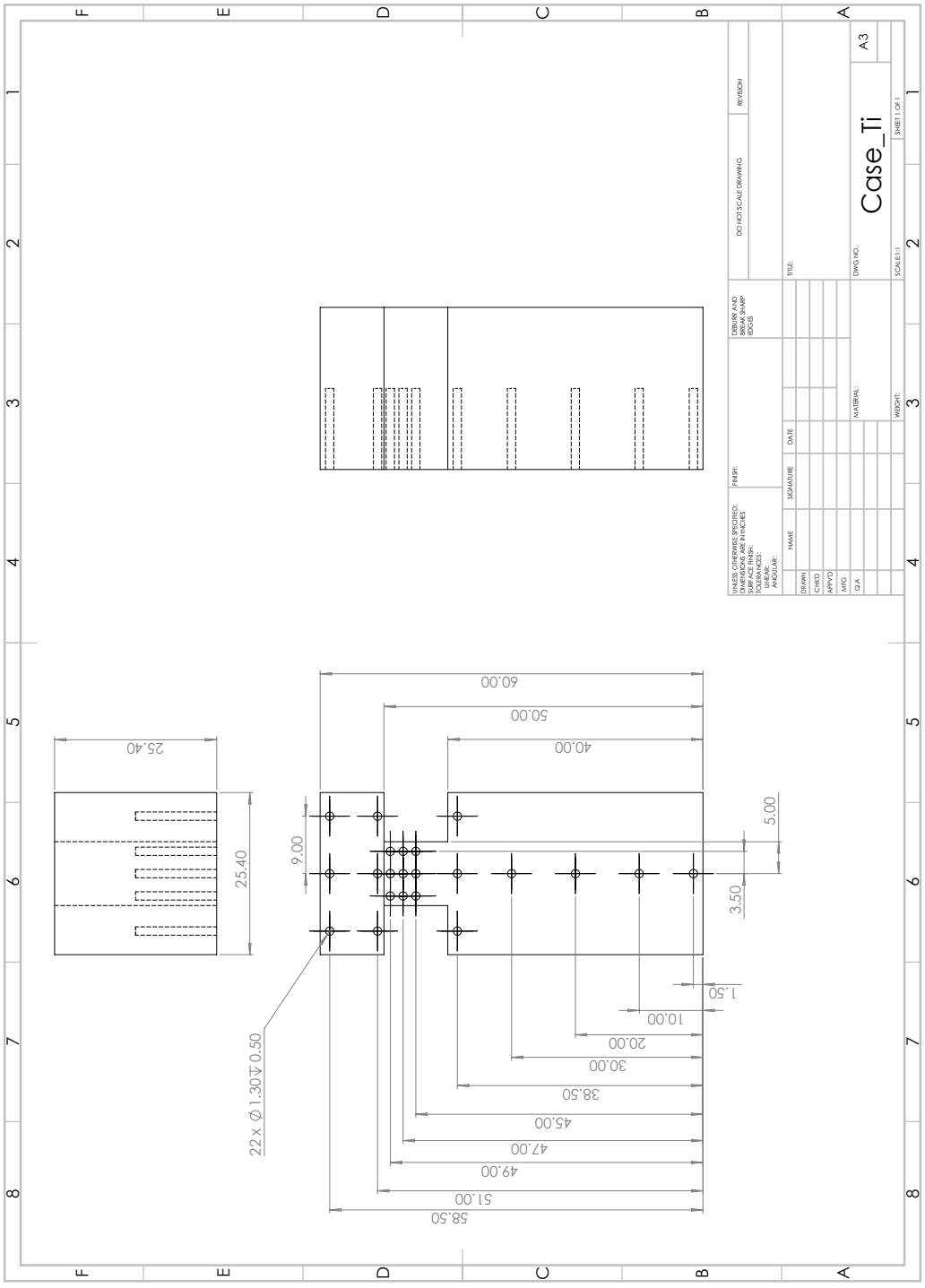

Figure B.1: Drawing of the Titanium AM Evaporator.

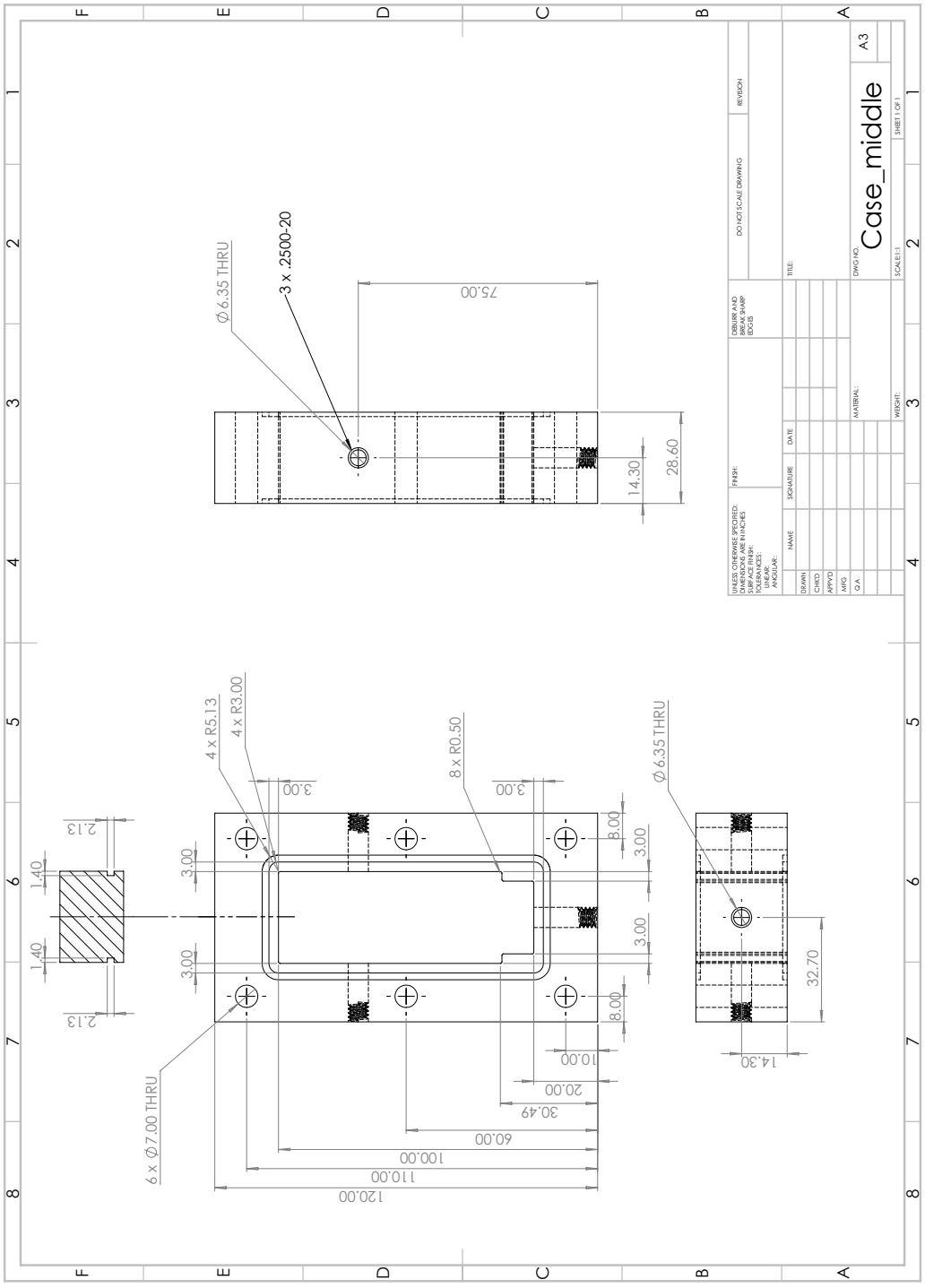

Figure B.2: Drawing of the casing around the Titanium AM Evaporator.

Bibliography

[1] Miriam Sargusingh et al. "NASA Environmental Control and Life Support Technology Development and Maturation for Exploration: 2017 to 2018 Overview". In: 48th International Conference on Environmental Systems. 2018.

[2] M. Aguilar et al. "The Alpha Magnetic Spectrometer (AMS) on the international space station: Part II — Results from the first seven years". In: *Physics Reports* 894 (2021), pp. 1–116.

[3] Eric Sunada et al. "A two-phase mechanically pumped fluid loop for thermal control of deep space science missions". In: 46th International Conference on Environmental Systems. 2016.

[4] Benjamin Furst et al. "An Additively Manufactured Evaporator with Integrated Porous Structures for Two-Phase Thermal Control". In: 48th International Conference on Environmental Systems. 2018.

[5] Ryohei Gotoh et al. "Experimental and analytical investigations of AlSi10Mg, stainless steel, Inconel 625 and Ti-6Al-4V porous materials printed via powder bed fusion". In: *Progress in Additive Manufacturing* (2022), pp. 1–13.

[6] Amir Faghri. *Heat pipe science and technology*. Global Digital Press, 1995.

[7] Hosei Nagano and Jentung Ku. "Gravity Effect on Capillary Limit in a Miniature Loop Heat Pipe with Multiple Evaporators and Multiple Condensers". In: 2007.

[8] M. A. Hanlon and H. B. Ma. “Evaporation Heat Transfer in Sintered Porous Media ”. In: *Journal of Heat Transfer* 125.4 (2003), pp. 644–652.

[9] Yu.F. Maydanik, M.A. Chernysheva, and V.G. Pastukhov. “Review: Loop heat pipes with flat evaporators”. In: *Applied Thermal Engineering* 67.1 (2014), pp. 294–307.

[10] Valery M. Kiseev, Valeri V. Vlassov, and Issamu Muraoka. “Experimental optimization of capillary structures for loop heat pipes and heat switches”. In: *Applied Thermal Engineering* 30.11 (2010), pp. 1312–1319.

[11] Jeehoon Choi et al. “Interface engineering to enhance thermal contact conductance of evaporators in miniature loop heat pipe systems”. In: *Applied Thermal Engineering* 60.1 (2013), pp. 371–378.

[12] Yong Tang et al. “Experimental investigation on capillary force of composite wick structure by IR thermal imaging camera”. In: *Experimental Thermal and Fluid Science* 34.2 (2010), pp. 190–196.

[13] Joseph P Mooney et al. “A capillary flow model for discretely graded porous media in two phase heat transfer applications”. In: *International Journal of Thermofluids* 15 (2022), p. 100183.

[14] HJ Van Gerner, RC Van Benthem, and J van Es. “Fluid selection for space thermal control systems”. In: (2014).

[15] Benjamin Siedel, Valérie Sartre, and Frédéric Lefèvre. “Complete analytical model of a loop heat pipe with a flat evaporator”. In: *International Journal of Thermal Sciences* 89 (2015), pp. 372–386.

[16] William G. Anderson. “Intermediate Temperature Fluids for Heat Pipes and Loop Heat Pipes”. In: 2007.

[17] Yiding Cao and Amir Faghri. “Analytical solutions of flow and heat transfer in a porous structure with partial heating and evaporation on the upper surface”. In: *International Journal of Heat and Mass Transfer* 37.10 (1994), pp. 1525–1533.

[18] V. X. Tung and Vijay K. Dhir. “A hydrodynamic model for two-phase flow through porous media”. In: *International Journal of Multiphase Flow* 14 (1988), pp. 47–65.

[19] Chuan Ren, Qing-Song Wu, and Mao-Bin Hu. “Heat transfer with flow and evaporation in loop heat pipe’s wick at low or moderate heat fluxes”. In: *International Journal of Heat and Mass Transfer* 50.11-12 (2007), pp. 2296–2308.

[20] Xianfeng Zhang, Xuanyou Li, and Shuangfeng Wang. “Three-dimensional simulation on heat transfer in the flat evaporator of miniature loop heat pipe”. In: *International Journal of Thermal Sciences* 54 (2012), pp. 188–198.

[21] C. Figus et al. “Heat and mass transfer with phase change in a porous structure partially heated: continuum model and pore network simulations”. In: *International Journal of Heat and Mass Transfer* 42.14 (1999), pp. 2557–2569.

[22] Tarik Kaya and John Goldak. “Numerical analysis of heat and mass transfer in the capillary structure of a loop heat pipe”. In: *International Journal of Heat and Mass Transfer* 49.17 (2006), pp. 3211–3220.

[23] Riadh Boubaker et al. “Dynamic model of heat and mass transfer in an unsaturated porous wick of capillary pumped loop”. In: *Applied Thermal Engineering* 76 (2015), pp. 1–8.

[24] Masahito Nishikawara et al. “Numerical Study of Thermal Performance of a Capillary Evaporator in a Loop Heat Pipe with Liquid-Saturated Wick”. In: *Journal of Electronics Cooling and Thermal Control* vol. 4.n° 4 (Dec. 2014), pp. 118–127.

[25] Kent S Udell. “Heat transfer in porous media heated from above with evaporation, condensation, and capillary effects”. In: *Journal of Heat Transfer* 105.3 (1983), pp. 485–492.

[26] P. S. Ramesh and K. E. Torrance. “Boiling in a porous layer heated from below: effects of natural convection and a moving liquid/two-phase interface”. In: *Journal of Fluid Mechanics* 257 (1993), 289–309.

[27] Q. Liao and T. S. Zhao. "Evaporative Heat Transfer in a Capillary Structure Heated by a Grooved Block". In: *Journal of Thermophysics and Heat Transfer* 13.1 (1999), pp. 126–133.

[28] Kimihide Odagiri and Hosei Nagano. "Characteristics of phase-change heat transfer in a capillary evaporator based on microscale infrared/visible observation". In: *International Journal of Heat and Mass Transfer* 130 (2019), pp. 938–945.

[29] Chen Li and G. P. Peterson. "Evaporation/Boiling in Thin Capillary Wicks (II)—Effects of Volumetric Porosity and Mesh Size". In: *Journal of Heat Transfer* 128.12 (Jan. 2006), pp. 1320–1328.

[30] Riadh Boubaker, Souad Harmand, and Vincent Platel. "Experimental study of the liquid/vapor phase change in a porous media of two-phase heat transfer devices". In: *Applied Thermal Engineering* 143 (2018), pp. 275–282.

[31] L. Mottet, T. Coquard, and M. Prat. "Three dimensional liquid and vapour distribution in the wick of capillary evaporators". In: *International Journal of Heat and Mass Transfer* 83 (2015), pp. 636–651.

[32] Prem Kumar et al. "Thermal-fluidic transport characteristics of bi-porous wicks for potential loop heat pipe systems". In: *Experimental Thermal and Fluid Science* 94 (2018), pp. 355–367.

[33] R. Giraudon et al. "Effect of the wick characteristics on the thermal behaviour of a LHP capillary evaporator". In: *International Journal of Thermal Sciences* 133 (2018), pp. 22–31.

[34] B. Paul. "Compilation of Evaporation Coefficients". In: *ARS Journal* 32.9 (1962), pp. 1321–1328.

[35] A.F. Mills and R.A. Seban. "The condensation coefficient of water". In: *International Journal of Heat and Mass Transfer* 10.12 (1967), pp. 1815–1827.

[36] Quickersim CFD Toolbox. In: *MATLAB Central File Exchange* (2020). URL: (https://www.mathworks.com/matlabcentral/fileexchange/71604-quickersim-cfd-toolbox.

[37] E. W. Lemmon et al. *NIST Standard Reference Database 23: Reference Fluid Thermodynamic and Transport Properties-REFPROP, Version 10.0, National Institute of Standards and Technology*. 2018. DOI: https://doi.org/10.18434/T4/1502528. URL: https://www.nist.gov/srd/refprop.

[38] S.J. Kline and F.A. McClintock. "Describing Uncertainty in Single Sample Experiments". In: *Mech. Engineering* 75 (1953), pp. 3–8.